# COMBINED SUPER-RESOLUTION FLUORESCENCE AND SCANNING ELECTRON MICROSCOPY FOR CATALYSIS RESEARCH

Jordi VAN LOON

Supervisor:
Prof. M. Roeffaers, KU Leuven

Members of the Examination Committee:
Prof. T. Niewold, KU Leuven, Chair
Prof. J. Hofkens, KU Leuven
Prof. D. De Vos, KU Leuven
Prof. J. W. Seo, KU Leuven
Prof. S. Munck, KU Leuven
Dr. A.-J. Bons, ExxonMobil Chemical Europe Inc.

Dissertation presented
in partial fulfilment of
the requirements for
the degree of Doctor of
Bioscience Engineering
(PhD)

October 2017

Doctoraatsproefschrift nr. 1456 aan de faculteit Bio-ingenieurswetenschappen van de KU Leuven

Uitgegeven in eigen beheer, Van Loon Jordi, Leuven

# Preface

I first started working in the molecular imaging and photonics lab as a master thesis student who still had everything to learn. Little did I know that five years on I would be writing up my PhD dissertation at the centre for surface chemistry and catalysis. During this period, I crossed paths with a lot of people and all of them had a part in both my professional and personal development. Simply put, without them, I wouldn't have gotten to where I am today. The proper acknowledgements are therefore in order.

I would like to start by especially thanking my supervisor, Prof. Maarten Roeffaers, for the great amount of effort and energy he has spent over the last five years, both during my master thesis and my PhD, to help me succeed. As is the case for every new endeavor, executing a PhD is associated with a learning curve. This curve would have been much steeper if it weren't for the extensive supervision I received and I am tremendously grateful for this.

The assessors of my PhD, Prof. Johan Hofkens and Prof. Dirk De Vos, also deserve a special mentioning for following up on my research during the past four years. Their critical viewpoints have improved the level of the research included in this dissertation. In the final stages of my PhD, their reflections were further complemented by those of the members of my examination committee: Prof. Jin Won Seo, Prof. Sebastian Munck, Prof. Theo Niewold and Dr. Anton-Jan Bons. I am very grateful for their critical but constructive feedback. This has helped me to improve my dissertation in all the important facets.

Apart from the supervision I received, several cooperations have also proven indispensable to successfully conclude my PhD. Special mentioning goes to Filippo, who introduced me to the world of single molecule fluorescence microscopy, Alexey, for his help during my initial steps as a researcher and Kris, for his support in developing and applying the FluoSEM which has been at the epicenter of the presented research. Also the administrative and technical support of Carine and later on Annelies and Paul have been of vital importance.

Of course, performing a PhD is much more than simply absorbing knowledge and developing your soft skills. Gaining life wisdom during the lab activities, parties and numerous coffee breaks is at least as important. This role was more than successfully fulfilled by: Liu, Christian, Niels, Dennis, Doortje, Julian, Eduardo, Jeroen, Eva, Charlotte, Wouter V, Wouter S, Wouter B, Collin, Guillaume, Thomas, Haowei, Tom, Arnica, Arun, Koen, Lexie, Dries, Jasper, Vincent, Elke,…

Er zijn uiteraard ook personen buiten het labo die een bedankje verdienen voor hun rol doorheen mijn loopbaan. Zo zijn er mijn meest doorwinterde vrienden; Kurt, Bart, Dennis, Niels, Lennert, Ive, Dieter, Jens, … Bedankt voor de (enkele) pogingen om naar mijn wetenschappelijke verhalen te luisteren, maar vooral om te pas en te onpas voor de nodige afleiding te zorgen.

Een woord van dank is ook op zijn plaats voor mijn vriendin die ik sinds enkele maanden ook met trots mijn verloofde mag noemen. Yka, bedankt voor je onvoorwaardelijke steun. Tijdens de moeilijkste momenten was jij er steeds om me bij te staan, waardoor ik het optimale uit de voorbije 4 jaar heb kunnen halen. Ook Alex en Jacqueline hebben hier een aanzienlijke rol in vervuld.

Mijn broer en zus mogen in deze lijst ook niet ontbreken. De laatste jaren zijn we sterk naar elkaar toe gegroeid en dit heeft zonder twijfel een positieve rol gespeeld in het behalen van mijn doctoraat. Thuiskomen was steeds een leuke afwisseling van het leven in Leuven. En zeker sinds de geboorte van Nandje kon ik tijdens de laatste hectische maanden mijn gedachten geregeld verzetten.

Het laatste woord richt ik graag tot mijn ouders. Make en pake, alles wat ik tot nu toe heb verwezenlijkt zou nooit mogelijk geweest zijn zonder de kansen die ik van jullie gekregen heb. Ik ben jullie hier dan ook onnoemelijk dankbaar voor en hoop dat het succesvol afsluiten van mijn periode in Leuven ook voor jullie een mooie mijlpaal is.

# Summary

Heterogeneous catalysts are commonly used to speed up chemical reactions. The performance of these materials is largely determined by their (surface) structure and chemical composition. Rationally improving solid catalysts therefore requires a thorough understanding of the structure-activity relationship down to the smallest possible length scales. Recently developed approaches that correlate fluorescence microscopy (FM) and scanning electron microscopy (SEM) allow such insights by linking nanoscale catalytic activity maps to the local structural context. All samples subjected to such investigations revealed a pronounced inter- and intraparticle activity distribution, that could in most cases be related to minute sub-particle structural features and defects. Until now, these correlative studies have exclusively been performed by using dedicated microscopes, which requires a delicate and time consuming sample transfer. Furthermore, despite the successful application of FM to investigate zeolite catalysis, even at the level of individual catalytic reactions, correlative studies have not yet been explored for this class of catalysts. The aim of this PhD was to investigate the nanoscale zeolite catalyst structure-activity relationship, by developing an integrated light and electron microscope (ILEM) that combines single molecule sensitive FM and SEM. While developing this device and accompanying assays, validation experiments were performed on ZnO photocatalysts.

The initial application of the ILEM led to a real-time visualization of silver nanoparticle photodeposition on individual ZnO crystals. This was enabled by the ability to simultaneously perform local UV irradiation, through the optical microscope, and SEM imaging, at the same region of interest (ROI). This required the use of a liquid cell, sealed by an electron and optically transparent window on each side, to perform such measurements inside the vacuum chamber of the SEM. As such, the ZnO photocatalyst could be submersed in a liquid silver (I) ion containing reaction mixture during SEM imaging. The UV irradiation needed for photodeposition was attained through the glass slide opposing the electron transparent window supporting the sample. This research is reported in **Chapter 2** and revealed that silver nanoparticle formation mostly occurs at crystal edges. At the same time, the contribution of the electron beam during silver deposition was found to be non-negligible. A quantitative structure-activity investigation was therefore performed by using the ILEM correlatively in **Chapter 3**. By performing nanoscale structural imaging on commonly encountered ZnO photocatalysts, before and after UV induced silver photodeposition, the facet dependent photocatalytic reactivity was explored at the single particle level. Furthermore, heterogeneities could be related to structural features and defects at the sub-particle level.

The first correlative fluorescence and electron microscopy investigation of zeolite catalysts was made possible after resolving several technical

challenges that were encountered during the photocatalyst structure-activity determination. Furthermore, by optimizing the fluorescence microscope to enable the detection of individual catalytic turnovers, super-resolved activity maps could be recorded with nanometer-scale precision. In **Chapter 4** it is described how this correlative approach directly revealed the effect of intercrystalline intergrowths, which are omnipresent in powdered zeolite batches, on the overall catalytic performance of acid mordenite zeolites. By resolving the orientation of the individual reaction products using linear polarized excitation light, the molecular alignment with respect to the underlying zeolitic framework could be visualized. This revealed that the catalytic activity at the defect-rich intergrowth boundary mainly originated from within the original microporous structure and that the intergrowth itself merely serves as a void space that facilitates mass transport into these pores. Acid leaching did not dramatically change this, as activity simply increased on previously active regions while the molecular orientation was maintained. This contrasted the results of static pyridine adsorption experiments, which indicated that the removal of 30% of framework aluminium should be sufficient for a transition of small-port to large-port H-MOR.

A correlative structure-activity investigation of individual ZSM-22 catalyst particles has also been achieved in **Chapter 5**. The typical needle-shaped morphology of these particles results from a lateral fusion of elementary nanorods. Indirect experimentation already suggested that during this lateral fusion, external, catalytically inactive, aluminium is converted into catalytically active internal aluminium. This is important with respect to the shape selective properties of the catalyst material, as this would denote that active sites are only located within the microporous structure. The availability of the ILEM allowed a direct visualization of catalyst activity and shape-selectivity at the sub-particle level which confirmed earlier assumptions about nanorod fusion. The prominently present catalytic hotspots were tentatively assigned to crystallographic mismatching during this fusion process. Hence, catalyst performance is locally increased by increasing accessibility into the shape selective micropores.

Over the course of this PhD, a performant ILEM was developed with accompanying tools to explore the structure-activity relationship of heterogeneous catalysts at the nanoscale. This enabled both consecutive and real-time investigations of ZnO photocatalysts, as well as the first correlative structure-activity studies on zeolite catalysts. This powerful research tool allows a direct correlation of catalyst structure and activity beyond the single particle level. As such, inter- and intraparticle activity variations are rationalized at the nanoscale and the investigation of industrially relevant catalyst samples is enabled, as the latter are commonly nanometer sized. It is anticipated that the further application and development of this ILEM will ultimately lead to a more rationalized catalyst optimization.

# Samenvatting

Chemische reacties worden vaak versneld door middel van heterogene katalysatoren. De prestatie van deze materialen hangt in grote mate af van hun (oppervlakte) structuur en chemische samenstelling. Een rationele katalysator optimalisatie vereist dus een grondig inzicht in de structuur-activiteit verhouding. Dergelijke inzichten kunnen bekomen worden aan de hand van recent ontwikkelde technieken die fluorescentie en scanning elektronen microscopie (FM en SEM) met elkaar correleren. Zo is het mogelijk om de katalytische activiteit te mappen met nanometer precisie en deze te linken aan de lokale structurele context. Dergelijke studies toonden reeds een uitgesproken verdeling van de activiteit aan, zelfs tussen individuele kristallen. In de meeste gevallen, konden deze heterogeniteiten gekoppeld worden aan kleine structurele kenmerken of defecten. Tot dusver zijn deze onderzoeken enkel uitgevoerd door middel van toegewijde microscopen. Dit vereist een delicate transfer van het staal tussen de modaliteiten. Daarenboven, zijn dergelijke correlatieve onderzoeken nog niet toegepast op zeoliet katalysatoren, ondanks de mogelijkheid om met FM enkelvoudige katalytische omzettingen te detecteren. Het doel van dit doctoraat was om een geïntegreerde licht en elektronen microscoop (ILEM) te ontwikkelen die super-geresolveerde FM combineert met SEM om zo de structuur-activiteit verhouding van zeoliet katalysatoren te bestuderen. Tijdens de ontwikkeling van dit toestel en de bijhorende procedures zijn validatie experimenten uitgevoerd op ZnO fotokatalysatoren.

De eerste toepassing van de ILEM resulteerde in een real time visualisatie van zilver nanopartikel fotodepositie op individuele ZnO kristallen. Dit was mogelijk doordat UV irradiatie simultaan kon gebeuren met SEM en dit op dezelfde positie. Om dergelijke metingen in de vacuüm kamer van de SEM uit te kunnen voeren, was de ontwikkeling van een *liquid cell* noodzakelijk, die zowel een elektronen als optisch transparant raam bevatte. Hierdoor kon SEM plaatsvinden terwijl het staal zich in een vloeibare zilver(I) ionen oplossing bevond. De benodigde UV fotonen voor fotodepositie bereikten het staal via het optische raam onderaan de cel. Dit onderzoek staat beschreven in **Hoofdstuk 2** en toont aan dat zilver depositie voornamelijk plaatsvindt op de randen van de ZnO kristallen. Tegelijkertijd werd ondervonden dat de invloed van de elektronen straal tijdens dit onderzoek niet te verwaarlozen was. Een kwantitatieve bepaling van de structuur-activiteit verhouding werd daarop bekomen door de ILEM correlatief toe te passen in **Hoofdstuk 3**. Door de ZnO partikels voor en na fotodepositie structureel te bestuderen, kon de kristalvlak afhankelijkheid van de fotokatalyse onderzocht worden voor individuele partikels. De waargenomen heterogeniteiten konden verder ook gerelateerd worden aan kleine defecten en structurele kenmerken.

Het eerste correlatieve fluorescentie en elektronen microscopische onderzoek

van zeoliet katalysatoren werd mogelijk na enkele technische aanpassingen van de ILEM. Door daarenboven de FM verder te optimaliseren teneinde de detectie van enkelvoudige katalytische omzettingen mogelijk te maken, konden nanometer geresolveerde activiteit mappen opgemeten worden. In **Hoofdstuk 4** staat beschreven hoe deze correlatieve benadering het effect van veel voorkomende interkristallijne vergroeiingen op de katalytische performantie van zure mordeniet zeolieten kon blootleggen. Door de oriëntatie van individuele reactieproducten te bepalen middels lineair gepolariseerd excitatie licht, kon ook de moleculaire uitlijning ten opzichte van het onderliggende microporie netwerk gevisualiseerd worden. Dit toonde aan dat de katalytische activiteit ter hoogte van defect rijke vergroeiingen voornamelijk plaatsvindt in het originele microporie netwerk. De vergroeiing zelf treedt enkel op als een ruimte waardoor massa transport naar deze poriën vereenvoudigd wordt. Zuur gemedieerd etsen zorgt niet voor een dramatische verandering van deze situatie, aangezien de activiteit enkel toeneemt op reeds actieve plaatsen en de moleculaire oriëntatie behouden blijft. Dit contrasteert met de resultaten van statische pyridine adsorptie experimenten die aantoonden dat de verwijdering van 30% van het aluminium uit het zeoliet rooster voldoende zou moeten zijn voor een transitie van *small-port* naar *large-port* mordeniet.

In **Hoofdstuk 5** werden ook individuele ZSM-22 katalysatoren bestudeerd met behulp van de correlatieve techniek. De typische naald vorm van deze partikels komt voort uit de laterale fusie van de elementaire *nanorods*. Indirecte experimenten suggereerden reeds dat extern, inactief, aluminium omgezet wordt naar katalytisch actief intern aluminium tijdens deze laterale fusie. Dit is van belang voor de vorm selectiviteit van de katalysator, aangezien dit wil zeggen dat activiteit voornamelijk binnenin de microporie structuur gelokaliseerd is. De beschikbaarheid van de ILEM maakte het mogelijk om de katalytische activiteit en vorm selectiviteit rechtstreeks waar te nemen voor enkelvoudige kristallen. Dit bevestigde eerdere aannames en toonde verder prominente katalytische hotspots aan. Deze laatste werden toegewezen aan een onvolledige laterale fusie, waardoor de toegankelijkheid naar de actieve sites in de microporiën toeneemt.

Tijdens dit doctoraat werd een performante ILEM ontwikkeld met bijhorende tools om de structuur-activiteit verhouding van heterogene katalysatoren te bestuderen op de nanoschaal. Dit maakte het mogelijk om zowel consecutieve als simultane experimenten uit te voeren op ZnO fotokatalysatoren, alsook werden hierdoor de eerste correlatieve studies van zeoliet katalysatoren mogelijk. Deze krachtige tool laat een directe correlatie toe van de structuur en activiteit, voorbij het niveau van individuele partikels. Hierdoor wordt het mogelijk om inter- en intrakristallijne heterogeniteiten tot op de nanoschaal te rationaliseren en kunnen industrieel relevante katalysatoren onderzocht worden. Door de verdere ontwikkeling en toepassing van de ILEM wordt verwacht dat een gerationaliseerde optimalisatie van vaste katalysatoren uiteindelijk mogelijk wordt.

# List of Abbreviations

| | |
|---|---|
| BET | Brunauer–Emmett–Teller |
| BSE | Back Scattered Electron |
| BSED | Back Scattered Electron Detector |
| CA-BODIPY | Catechol-Modified 3,4-Dinitrophenyl-substituted Borone Dipyrromethene |
| CL | Cathodoluminescence |
| CLEM | Correlative Light and Electron Microscopy |
| CLSM | Confocal Laser Scanning Microscopy |
| DL | Diffusion Length |
| DN-BODIPY | 3,4-Dinitrophenyl-substituted Borone Dipyrromethene |
| EDS | Energy Dispersive Spectroscopy |
| EM | Electron Microscopy |
| EMCCD | Electron Multiplying Charged Couple Device |
| EMIM | Ethyl Methyl Imidazolium |
| ETD | Everhart-Thornley Detector |
| FCC | Fluid Catalytic Cracking |
| FEG | Field Emission Gun |
| FFA | Furfuryl Alcohol |
| FID | Free Induction Decay<br>Flame Ionization Detector |
| FM | Fluorescence Microscopy |
| FOV | Field of View |
| GSED | Gaseous Secondary Electron Detector |
| HAADF | High-Angle Annular Dark-Field |
| HFW | Horizontal Field Width |
| HR | High Resolution |
| ICP-OES | Inductively Coupled Plasma Optical Emission Spectroscopy |
| iFlEM | Integrated Fluorescence and Electron Microscopy |
| ILEM | Integrated Light and Electron Microscopy |
| ITO | Indium Tin Oxide |
| LED | Light Emitting Diode |
| LL | Lower Limit |
| LP | Long Pass |
| LP-MOR | Large Port Mordenite |
| MOR | Mordenite |
| MQ | Milli Q |

| | |
|---|---|
| MR | Membered Ring |
| NA | Numerical Aperture |
| NASCA | Nanometer Accuracy by Stochastic Chemical Reactions |
| NMR | Nuclear Magnetic Resonance |
| NP | Nanoparticle |
| NR | Nanorod |
| OEC | Oxygen Evolution Catalyst |
| PALM | Photoactivated Localization Microscopy |
| PDMS | Polydimethylsiloxane |
| PL | Photoluminescence |
| pyr | Pyridine |
| ROI | Region of Interest |
| SE | Secondary Electron |
| SEM | Scanning Electron Microscopy |
| SPM | Scanning Probe Microscopy |
| SP-MOR | Small-Port Mordenite |
| SRFM | Super-Resolution Fluorescence Microscopy |
| STEM | Scanning Transmission Electron Microscopy |
| STORM | Stochastic Optical Reconstruction Microscopy |
| TEM | Transmission Electron Microscopy |
| UV | Ultraviolet |
| VC | Vacuum Compatible |
| ZSM | Zeolite Socony Mobil |

# Table of Contents

# Chapter 1

## Introduction - Correlating Catalyst Structure and Activity at the Nanoscale

.

# Chapter 1 - Correlating Catalyst Structure and Activity at the Nanoscale

## 1.1. Introduction

Over 80% of industrial scale chemical processes make use of heterogeneous catalysts.[1,2] Typically, this involves the use of solid catalyst materials, like supported metal nanoparticles (NP), metal oxides or zeolites, to speed up liquid or gas phase reactions.[2–9] The performance of these materials is largely determined by their (surface) structure and chemical composition.[10,11] The intrinsic structural complexity therefore often leads to significant variability in physicochemical properties and thus catalytic activity on both the inter- and intraparticle level.[12–14] Consequently, the rational improvement of heterogeneous catalysts requires a thorough understanding of the structure-activity relationship down to the smallest possible length scales. This information is not available using traditional bulk scale characterization tools, as they yield ensemble averaged information. Highly resolved microscopy techniques, such as electron microscopy (EM) and scanning probe microscopy (SPM), allow nano and even atomic scale investigations of the catalyst structure. However, the structural heterogeneity renders it impossible to directly link these results to the corresponding catalytic performance since the latter information is only available from bulk scale activity testing.[15–17]

The development of super-resolution fluorescence microscopy (SRFM) has recently enabled the investigation of catalyst activity down to the nanoscale with the possibility of resolving individual catalytic turnovers.[18–20] In such studies a fluorogenic reagent is used, i.e., a non-fluorescent reagent that is catalytically converted into fluorescent product molecules. Some of these reaction products can even be detected with single molecule sensitivity and subsequently localized with nanometer-scale accuracy; note that the accuracy depends on several factors such as number of collected photons, signal-to-noise ratio, pixel size, etc.[21–23] This approach enabled, for the first time, the reconstruction of nanometer scale catalytic activity maps based on individual catalytic turnovers and revealed large inter- and intraparticle variations in activity distribution for various solid catalytic materials.[13,14,17,22,24,25] Nonetheless, insights into the structure-activity relationship remain limited, as nanoscale activity maps could not straightforwardly be related to the corresponding structural or compositional information. Commonly, this was attempted by linking activity maps to diffraction limited optical transmission images of the same particle or highly-resolved electron micrographs obtained from similar crystals of the same synthesis batch. Increased efforts have therefore been undertaken to combine SRFM and EM, and correlate information from both methods. This introduction provides a summary of the benchmark efforts undertaken to investigate the structure-activity relationship in heterogeneous catalysts at the (sub)single-particle level.

## 1.2. Correlating catalyst structure and activity

The SRFM assays used in catalysis research have been largely borrowed from biological research. The same applies to correlative fluorescence microscopy (FM) and EM studies that are used to determine the catalyst structure-activity relationship. Information from both microscopy modalities can be acquired by a correlative approach or using an integrated device, and EM is either achieved by scanning electron microscopy (SEM) or (scanning) transmission electron microscopy ((S)TEM). Clearly, choosing between these combinations has implications on the sort of experiments that can be performed. The catalyst under investigation and the catalytic process of interest thus dictate which approach is preferred.

### 1.2.1.Combining fluorescence and electron microscopy

In correlative light and electron microscopy (CLEM) (**Figure 1.1a**), FM and EM are performed consecutively by employing dedicated microscopes. This allows full flexibility over the FM configuration, even enabling SRFM, but requires sample transfer which could lead to contamination and complicates image registration.[26,27] Fiducial markers, visible in both FM and EM, are commonly mixed into the sample to facilitate the image registration process. However, these markers might compromise sample integrity and it remains time consuming to accurately retrieve the region of interest (ROI) and perform image overlay. Alternatively, commercial systems have been developed that make use of a shuttle and find approach to enable an automated ROI retrieval. This procedure facilitates FM and EM correlation by means of a dedicated sample holder and a semi-automated calibration procedure. When TEM is used in a correlative approach, exhaustive sample preparation is typically needed, requiring sample slicing. This potentially deteriorates nanoscale structural features.

Integrated light and electron microscopy (ILEM) can be based on both SEM and (S)TEM (**Figure 1.1b** and **Figure 1.1c**), and, as two imaging modalities are combined into one, it has the potential to largely reduce sampling time and minimize the chances of sample contamination.[28,29] However, (S)TEM image formation is done via a detector placed coaxially to the electron gun. The objective lens of an epifluorescence microscope therefore needs to be positioned at a 90-degree angle. This necessitates sample rotation when switching between modalities and implies that only consecutive experiments can be performed. Additionally, due to these geometrical constraints, a long working distance objective lens is required, which only allows diffraction limited confocal laser scanning microscopy (CLSM). In an SEM based ILEM, the objective lens and electron gun can be placed at opposite sides of the sample. This allows simultaneous SRFM and SEM. To study the catalyst under realistic conditions, and similarly, for many biological experiments, the sample needs to be submerged inside a liquid environment. Such liquid contained samples are not compatible with the high vacuum conditions of the EM and complicate the application of ILEM to correlate catalyst structure to activity at the nanoscale.

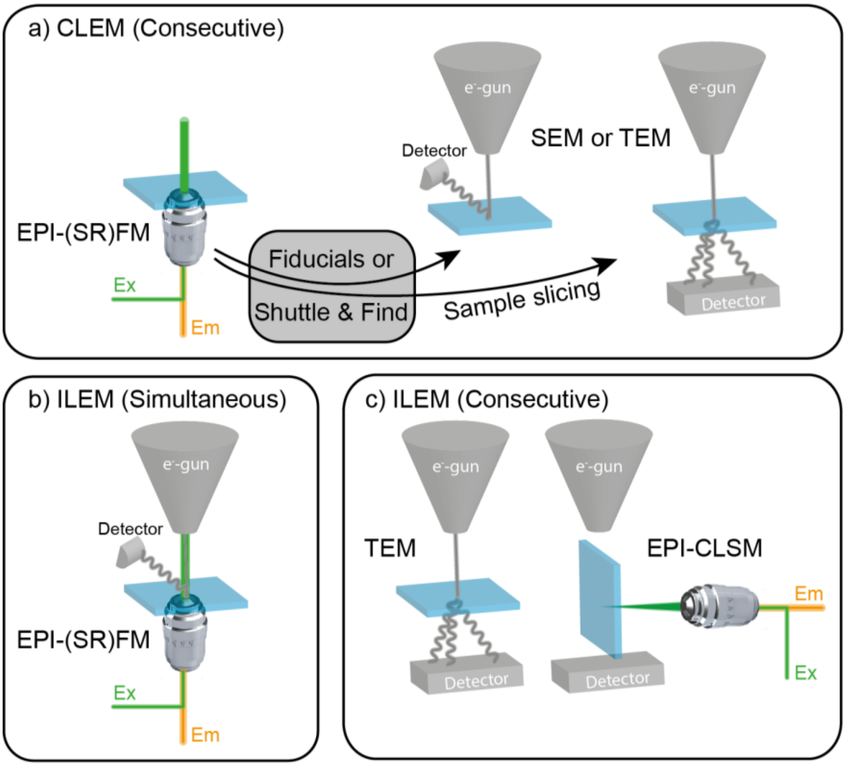

***Figure 1.1.*** *Schematic representation of the different approaches to correlate catalyst structure and activity on the nanoscale by means of FM and EM. a) Correlative light and electron microscopy (CLEM), enables consecutive (SR)FM and SEM or TEM, but requires fiducial markers or a shuttle and find approach to facilitate ROI retrieval and in case of TEM, additional sample slicing is required. b) Integrated light and electron microscopy (ILEM) that combines wide-field FM with SEM or c) confocal laser scanning microscopy (CLSM) with TEM. Whereas the former allows a simultaneous use of both modalities, the latter only allows consecutive imaging due to its intrinsic configuration.*

### 1.2.2. Towards *in situ* SRFM and SEM

In this PhD project, one specific aim was to develop an SEM based ILEM that enables SRFM based on the localization of individual fluorophores. Besides the stringent requirements set by the specific nature of the sample, i.e., catalysts in liquid environment, the aim of observing single molecule fluorescence puts severe constraints on the design of the optical microscope integrated in the SEM. Specifically, the use of high numerical aperture (NA) objective lenses to maximize the photon collection, the limited focal depth and working distance in combination with good mechanical stability and ease and precision of image correlation had to be taken into consideration. A brief summary of the developments that were already available to perform *in situ* SEM in combination with light microscopy before the start of the PhD project follows in this section. The obvious strengths and weaknesses of these approaches were taken into consideration before developing the SEM based iLEM with SRFM in Leuven.

Several approaches have been developed to perform EM on liquid contained samples using either open or closed cells. In combination with the development of a SEM based ILEM that is capable of performing SRFM, this could ultimately lead to the *in situ* investigation of the structure-activity relationship of heterogeneous catalysts at the nanoscale.

Since the development of environmental SEM (ESEM) in the 1980s,[30] the investigation of samples that are covered in a thin layer of liquid has become possible by allowing the introduction of water vapor into the sample chamber and cooling the sample to subzero temperatures.[31] Because of the implementation of differential pumping and pressure limiting apertures, proper functioning of this device is ensured with up to 4000 Pa of chamber pressure.[32,33] BSE's can be used for imaging purposes, regardless of the chamber pressure, however, SE detection requires the application of a dedicated gaseous secondary electron detector (GSED) that measures the amount of gas ionization in the sample chamber.[34] Such a device is extremely useful to investigate fluorescently stained, fully wetted biological samples using an ILEM. However, the lack of truly atmospheric conditions and the incompatibility with liquids other than water make it unsuitable to perform fluorogenic reagent based SRFM.

An alternative to ESEM that enables samples to be maintained at even higher pressures and in a wider variety of liquids is by enclosing the sample in a closed cell with an electron transparent window. This window acts as a barrier between the vacuum of the SEM chamber and the elevated pressure conditions inside the sample compartment. Such a device was reported by Thiberge et al. and was later on commercialized as the WetSEM QX-series of Quantomix which is readily available from electron microscopy consumables suppliers (**Figure 1.2**).[35,36] In summary, a traditional SEM stub is transformed into a liquid containing capsule by mounting a 145 nm thick polyimide window, reinforced by a TEM Ni grid, at the top, and a pressure relief membrane at the bottom; the role of the latter membrane is to prevent rupturing of the electron transparent window in case a pressure buildup occurs in the liquid cell. The sample under investigation is deposited just below the polyimide window. With such a capsule experiments can be performed at increased temperatures if a heating element is coupled to the stub pin and also a flow can be provided through the cell.[31] There is even a possibility to introduce a light guide that is coupled to a spectrometer through the stub pin for cathodoluminescence (CL) applications (**Figure 1.2b**).[35] As such, by correlating the position of the electron beam to the corresponding CL intensity, a correlation of sample functions to its structure is already possible. The wetSEM liquid cell design is, however, not compatible with FM as this would require the application of an objective lens that is in focus on the sample.

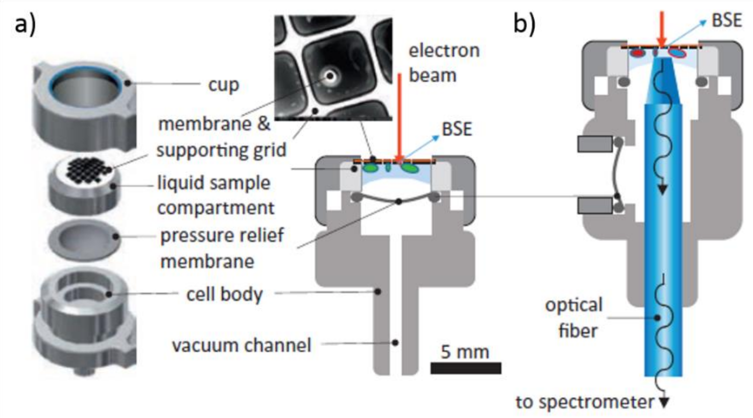

***Figure 1.2.*** *a) Different components of the wetSEM capsule. b) Configuration of the wetSEM capsule in combination with an optical fiber that is coupled through the stub pin, enabling CL detection. Reproduced with permission from Ref.* [31]

Alternatively, the atmospheric SEM (ASEM), commercially available as the Jeol Clairscope, (**Figure 1.3**) allows *in situ* optical microscopy and SEM.[32,33,37] This device consists of an inverted SEM. The sample can be deposited on an electron transparent $Si_3N_4$ window which is part of a larger petridish that is mounted on top of this device. Like the previous wetSEM capsule, the electron transparent window serves as the barrier between the high vacuum inside the SEM column and the sample at elevated pressures or even in liquid. An important difference, however, is the fact that the sample is now freely accessible from the top, simplifying experimental procedures. Furthermore, as the sample is located on top of the $Si_3N_4$ window, its mounting is also more stable due to the gravitational force and incomplete wetting of the sample does not pose a problem. On the other hand, it is important to consider the stability of the inverted SEM as it is only separated from the liquid and atmospheric environment by the thin $Si_3N_4$ window. A three-component protection system was therefore instated, comprising a specialized shutter which is placed between the dish and column, an air leak valve that introduces air into the chamber to bring the ASEM chamber to atmospheric pressure immediately after the electron transparent window breaks, and an inner pipe which is provided inside the SEM with an orifice to protect the electron gun.[38]

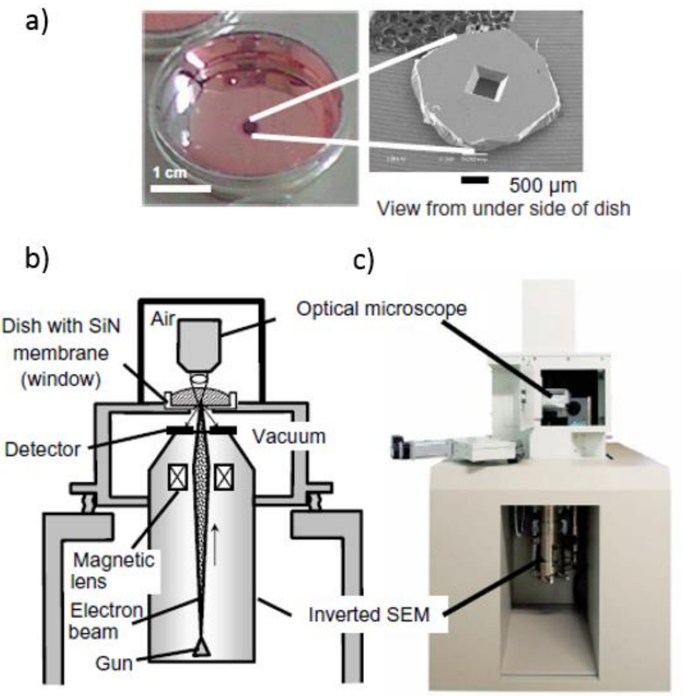

***Figure 1.3.*** *a) Sample dish with integrated* $Si_3N_4$ *window, which serves as the barrier between the atmospheric conditions where the sample is contained, and the high vacuum conditions of the electron gun. b) and c) Schematic representation and picture of the atmospheric SEM combined with an optical microscope. Adapted with permission from ref.* [32]

The space that is available on top of the sample can be used to mount an upright optical microscope (**Figure 1.3 b and Figure 1.3 c**). For example, Nishiyama et al. used a CLSM.[38] Besides air objectives, FM can be performed using a water dipping objective lens. Nonetheless, the configuration of the ASEM does not allow the application of a high NA immersion oil objective lens that is typically used to perform SRFM.

Based on the specific goals of this PhD work, i.e., linking nanoscale catalyst structure to performance by combining SRFM and SEM, it was considered that the approach reported by Liv et al., and commercialized by Delmic BV, is the most promising.[29,39] In this device the optical microscope is partially integrated inside the SEM vacuum chamber. Specifically, a high NA objective lens is mounted underneath the sample, coaxially to the electron gun, as illustrated in **Figure 1.1b**. The position of this objective can be adjusted in three dimensions with respect to the sample. Besides an accurate alignment with respect to the fixed center of the electron gun, this also allows accurate optical focusing on the sample. Additionally, it is also possible to move the sample stage in three dimensions, enabling imaging of different regions of interest while also the working distance of the EM can be reduced.

Apart from the typical samples inside the SEM chamber vacuum, liquid contained samples can be studied in so-called nanoreactors which have an electron transparent window at the top and an optically transparent window at the bottom.[40,41] As was the case for the wetSEM capsule, the sample is mounted at the bottom of the electron transparent window, which is in this case manufactured from $Si_3N_4$. In an initial application, a high NA (0.95) 40X air objective was used, allowing both CLSM and wide field FM with high resolution on biological samples while performing SEM. Even though, this approach did not yet enable SRFM, an important advantage is the offered flexibility towards the choice of SEM. More precisely, it is not limited to one specific model such as the JEOL Clairscope in the ASEM. The latter has a limited spatial resolution due to the use of a tungsten filament cathode. Therefore, the commercial approach offered by Delmic BV is used in this work as this allowed the integration of an optical microscope with a FEI Quanta 250. In order to maximize the performance of the optical microscope, a high NA oil-immersion objective lens needed to be integrated inside the SEM vacuum chamber. Where most immersion oils are not compatible with these conditions, the ionic liquid, 1,3 EMIM acetate, was chosen as it is characterized by a low vapor pressure, low viscosity and suitable refractive index ($n = 1.5$).

The integration of a vacuum compatible 1.4 NA 100X objective into the system makes the alignment procedure of the optical pathway more challenging since small misalignments of the optical components will lead to relatively large deflections of the excitation and fluorescence beams. Hence, the optical path needs to be carefully redesigned to allow minute adjustments. This also means that the procedure for aligning the FOV’s of the objective lens and electron gun becomes more challenging because of the relatively small horizontal field width of the optical microscope. A proper alignment protocol can be established based on the detection of the CL signal of the SEM using the integrated optical microscope.

An *in situ* application of the proposed ILEM with SRFM capabilities would require a redesigned version of the nanoreactor that is described by Liv et al.[40,41] For example, the distance between the $Si_3N_4$ window and the cover slide is 200 µm in the original design. This distance is larger than typical working distances of high NA objective lenses and renders it impossible to bring the sample in focus. Furthermore, single catalytic turnover mapping requires the use of a fluorogenic reagent. Once this reagent is added to the sample the reaction is initiated. Thus, the time required to assemble the cell and mount it into the SEM chamber leads to a fluorescence build-up that compromises the possibility to perform super-resolved catalytic activity mapping. A suitable liquid cell should therefore be equipped with flow capabilities that allow addition of the reagent upon request. In **Appendix 2** of this dissertation, an extended discussion of different approaches is provided and a liquid flow cell design is proposed that will ultimately allow *in situ* SRFM and SEM for catalysis research.

### 1.2.3. Nanoscale structure-activity investigation of metal nanoparticles

The catalytic activity of metal NP's originates from active surface sites and can be related to the expression of specific crystallographic facets, defects or influences from the support.[10] Due to their intrinsically small dimensions, EM has already been used from the initial SRFM investigations to provide structural information that complements the catalytic performance.[20] However, in these studies, pioneered by Chen and co-workers, metal NP catalysts are commonly coated with a mesoporous silica shell to stabilize their morphology and prevent aggregation. This shell additionally facilitates SRFM as the diffusion of fluorescent product molecules is slowed-down. The particle size and shell thickness of such silica coated particles are commonly determined by complementing SEM based CLEM with TEM.

The first application of SEM based CLEM to investigate metal NP catalysts was achieved by Zhou et al.[42] Catalytic activity mapping of Au nanorods (NR) incorporated into a mesoporous $SiO_2$ shell was performed by using the oxidative deacetylation of amplex red. Registration of the nanoscale activity maps with the SEM images was ingeniously enabled by using the NR's as fiducial markers. This revealed a heterogeneous activity distribution at the sub-particle level, characterized by an increased activity on the tips compared to the center of the particles (**Figure 1.4**). This behavior was less pronounced for larger NR's and, interestingly, a small fraction of NR's showed an opposite behavior. This information would have been lost in ensemble catalytic activity testing.

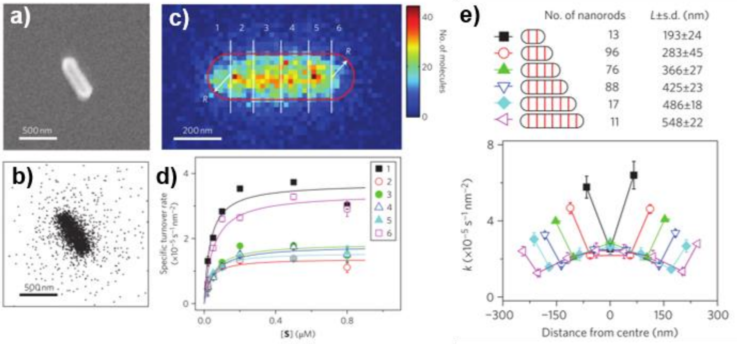

***Figure 1.4.*** *a) SEM image of the Au nanorod particle under investigation. b) Scatter plot of the first portion of the detected fluorescent product molecules resulting from the catalytic conversion on the Au nanorod represented in a). c) Nanoscale catalytic activity map obtained by rotating the image to orient it horizontally and by binning the detected catalytic turnovers in 20 x 20 nm$^2$ areas. The color scale represents the*

*number of turnovers detected in the respective areas, the red line shows the outline of the $SiO_2$ shell of the nanorod and the white lines subdivide the nanoparticle into six different segments. d) The specific reaction rates of the different segments assigned in c), depending on the fluorogenic reagent concentration. e) The specific catalytic reaction rates within the different sub segments are represented with respect to their distance from the center of the NR's. Averaged data, obtained over 301 nanorods, subdivided into six length groups. The subdivision is shown in the scheme at the top. Adapted with permission from ref.* [42]

The heterogeneous activity distribution was attributed to a varying density of crystallographic defects within individual NR's. Such defects, typically low-coordination metal sites, lead to an increased catalytic activity and are more commonly encountered on NR tips compared to sides.[3,4] This clearly corroborates with the notion of locally increased activity. On the other hand, a decreasing activity is observed when probing from the center of the particles towards the tips and this is even more pronounced for larger particles (**Figure 1.4e).** This trend is attributed to the presence of growth induced defects on the NP's sides. An increased growth rate induces more surface defects and as the growth rate decreases in time, less defects will be incorporated towards the tips of the particle. Additionally, the synthesis of larger particles is characterized by a relatively large initial growth rate, aggravating the effect.

The same fluorogenic reaction has been applied by Shen et al. to investigate the presence of surface reaction intermediates on mesoporous $SiO_2$ coated and bare pseudospherical Au NR's.[43] By correlatively applying SEM and SRFM, a surface adsorbed one-electron-oxidized amplex red radical intermediate was identified. Based on the reaction kinetics, a heterogeneous activity distribution was observed within the individual NR's which was attributed to the large structural complexity. The presence of this reaction intermediate would thus have remained hidden in ensemble averaged experiments.

Such correlative research has also been performed on Au nanoplates with a mesoporous $SiO_2$ shell using the fluorogenic resazurin to resorufin reduction.[44] A clear heterogeneous activity distribution was observed on the sub-particle level, showing differences between facets, morphological features and even between the center of a NP and its periphery (**Figure 1.5**). More precisely, NP corners proved to be more catalytically active than edges and even more so than the flat facets, and the activity decreases between the particle's center and edge. The extent of this radially decreasing reactivity was shown to be size dependent, as the effect was less pronounced for larger particles. This is ascribed to the slower growth rate reduction that enables the formation of larger NP's. However, the average specific activity is smaller for larger NP's. These results were interpreted as originating from growth induced surface defects, as was previously the case for Au NR structures.[42,43]

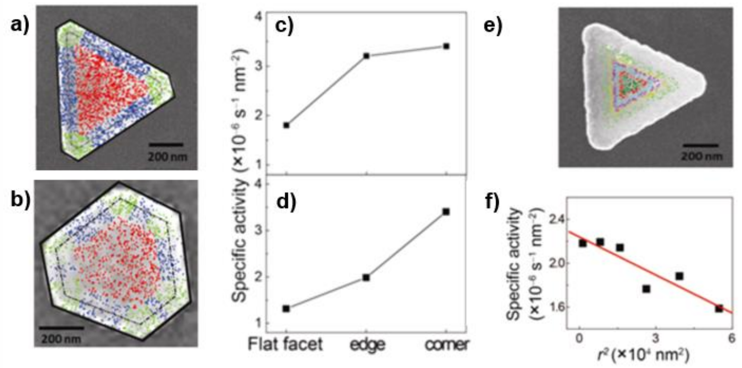

***Figure 1.5.*** *Catalytic activity distribution on the different facets of a) triangular and b) hexagonal Au nanoplates in a $SiO_2$ shell. Color coding represents the respective regions in which the turnover occurred; flat facet (red), edge (blue) and corner (green). The dashed line highlights the transition between the Au nanoplate and the surrounding $SiO_2$ shell. c) The specific activity on the different regions of the triangular nanoplate and d) on the hexagonal nanoplate. e) The radial activity gradient on the flat facet. This facet is subdivided into different radial segments towards the outside and color coded. f) Specific activity measured within the different radial segments, where r is the distance between the center of the flat surface and the middle of the corresponding radial segment. Adapted with permission from ref.* [44]

Metal NP catalyst samples are clearly characterized by an inter- and intraparticle heterogeneity. Regardless of this complexity, correlative SRFM and SEM has the power to look beyond the ensemble level and reveal sub-particle activity distributions. This enables parallel catalyst screening as a means of high-throughput characterization.[45] As such, highly active catalyst particles can be identified and subpopulations can be easily resolved (**Figure 1.6**). It has furthermore been proven that the relevance of these fluorescence based investigations can be extended towards more generally applied, non-fluorescent, catalytic reactions by establishing a correlation between them.

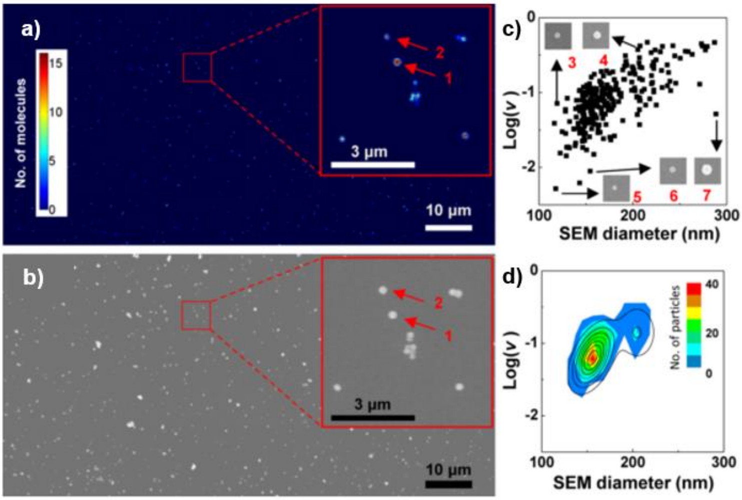

***Figure 1.6.*** *a) Super-resolved catalytic activity map showing the resazurin to resorufin reduction of approximately 1000 pseudospherical gold nanoparticles in a SiO$_2$ shell. The inset represents a zoomed in area. b) The corresponding SEM image of the activity map shown in a). c) Scatter plot that shows the turnover rate ([v] = $s^{-1}$.particle$^{-1}$) of individual catalyst particles in function of their diameter and d) contour plot of the histogram in c). The solid black lines represent fits with 2D Gaussian functions. Adapted with permission from ref.* [45]

### 1.2.4.Nanoscale structure-activity investigation of photocatalysts

Similar to metal NP catalysis, most photocatalytic materials consist of non-porous semiconductor particles in which the activity is limited to the outer crystal surface and crystallographic features play an important role in the photocatalytic performance.[46,47] For example, structural defects can act as electron or hole traps and locally enhance photoreductive or -oxidative activity. Correlative SRFM and SEM is therefore ideally suited to reveal the structure-activity relationship of individual photocatalyst particles. The function of the optical microscope in such investigations is twofold. Besides enabling catalytic activity mapping by visualizing single conversions of fluorogenic substrates, the optical microscope can also be used to introduce the light that stimulates the photocatalytic process and enables the generation of charge carriers.

Tachikawa et al. have developed a redox-responsive fluorogenic probe reaction based on the photoreductive conversion of 3,4-dinitrophenyl-substituted boron dipyrromethene (DN-BODIPY).[48] Using this fluorogenic reaction an increased photoreductive activity on the {101} facets of anatase TiO$_2$ crystals compared to the {001} facets was revealed.[49] By immobilizing the sample on a cover slide equipped with a numbered grid, SRFM investigations, performed in a specialized inverted sample cell, could be correlated with SEM. As such, an increased catalytic activity could be attributed to micron scale structural defects. In another experiment, the visible-light photocatalytic activity of Au-NP functionalized $TiO_2$ was observed to preferentially occur in zones of tens of nanometer surrounding the Au-NP deposits.[50] This was assumed to be the result of the local effect of the plasmon-induced electron and/or energy transfer processes.

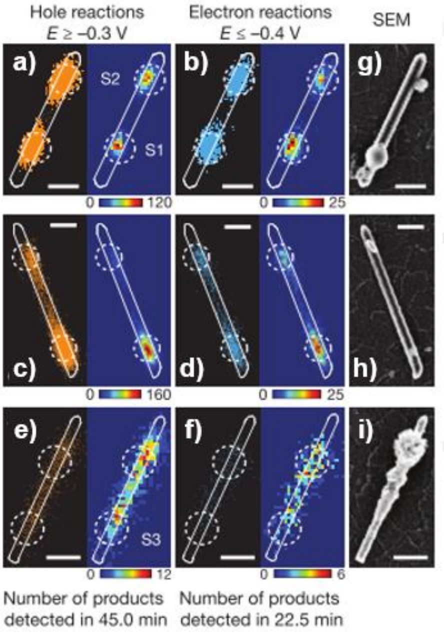

***Figure 1.7.*** *a) Scatter plot (left) and two-dimensional histogram (40 × 40 nm$^2$ pixels; right) of all individual resorufin product molecules (orange dots) generated from hole-induced amplex red oxidation reactions at $E \geq -0.3$ V on a single $TiO_2$ nanorod with two localized hotspots. The solid white line is the outline of the nanorod, determined using SEM. Dashed white circles denote focused 375-nm laser spots for photocurrent measurements and OEC deposition. The color scales indicate number of products formed. b) Same as a), but at $E \leq -0.4$ V, and the blue dots are resorufin product molecules generated from electron-induced resazurin reduction reactions. c)–f), Same as a) and b), but for a nanorod with a single dominant hole reaction hotspot (c, d) or delocalized hole reactions (e, f). g)–i), SEM images of the three nanorods in a)–f) after OEC deposition. All scale bars are 400 nm. Adapted with permission from ref.* [51]

The previously applied amplex red based fluorogenic reaction has also been used to study the photoelectrocatalytic oxidation reaction on rutile $TiO_2$ particles.[52] In these experiments, an ITO functionalized cover slide was used as cathode to selectively drain the photogenerated electrons. This ensured that electron-induced oxidation pathways were suppressed. Hence, only direct and indirect photooxidation processes, induced by photogenerated holes, were probed. This research proposed a mechanism in which reagent molecules are oxidized by surface adsorbed hydroxyl radical species and correlative imaging showed a significant inter- and intraparticle heterogeneity. These rutile $TiO_2$ particles are commonly modified with an oxygen evolution catalyst (OEC) to improve water oxidation efficiency (**Figure 1.7**).[51] Correlative SRFM and SEM indicated that careful control over the OEC deposition is important to attain optimal performance. Based on these results, the authors suggested a block-deposit-remove strategy that allows OEC deposition at the preferred positions. Hence, a rational design of catalytic photoelectrodes is within reach.

Reagent adsorption is an important step during photocatalysis and needs to be well understood. The adsorption ability of anatase $TiO_2$ particles has been investigated using the fluorogenic catechol-modified BODIPY (CA-BODIPY) molecules.[53] As such, a clear facet and solvent dependent adsorption was observed, which was indicative for the adsorption of water and organic compounds. The latter were additionally found to be mutually competitive. Additionally, $TiO_2$ nanocrystals showed an improved adsorption over micrometer sized particles due to the presence of crystallographic defects. Similarly, an increased exposure of Fe sites near branch tips of $Fe_2O_3$ pine tree shaped structures also led to a preferred adsorption (**Figure 1.8**).

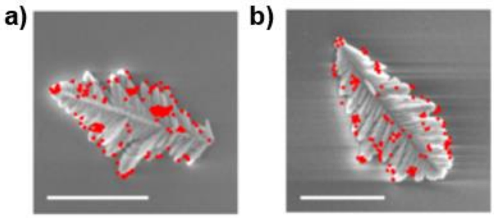

***Figure 1.8.*** *Scatter plots representing the locations of the reactive sites (red dots) on $Fe_2O_3$ branches determined by means of the fluorogenic CA-BODIPY reaction. A preferential adsorption near branch tips is observed. Scale bars are 2 µm. Adapted with permission from ref.* [53]

### 1.2.5. Nanoscale structure-activity investigation of solid acid catalysts

The catalytic activity of various zeolite based acid catalysts has been studied using SRFM. In contrast to metal NP- and photocatalysts, the performance of zeolites originates from the presence of highly active (acid) sites contained inside the characteristic microporous structure. Since these pores typically have similar dimensions as reagent and product molecules, such materials are in high demand for shape selective catalysis. However, these micropores also induce mass-transport limitations.[54] This is commonly resolved by introducing meso- and macroporous defects to enhance catalytic performance. Such modifications clearly bring variability inside the crystalline zeolite framework. For industrial scale applications, these zeolite catalysts are often embedded in large catalyst bodies, such as extrudates. During the shaping of these catalysts, various chemicals are added into the system that can alter the catalytic performance via pore blocking and de- and realumination.[55,56] Clearly, also the field of zeolite catalysis would benefit from a well-defined structure-activity relationship at the nanoscale.

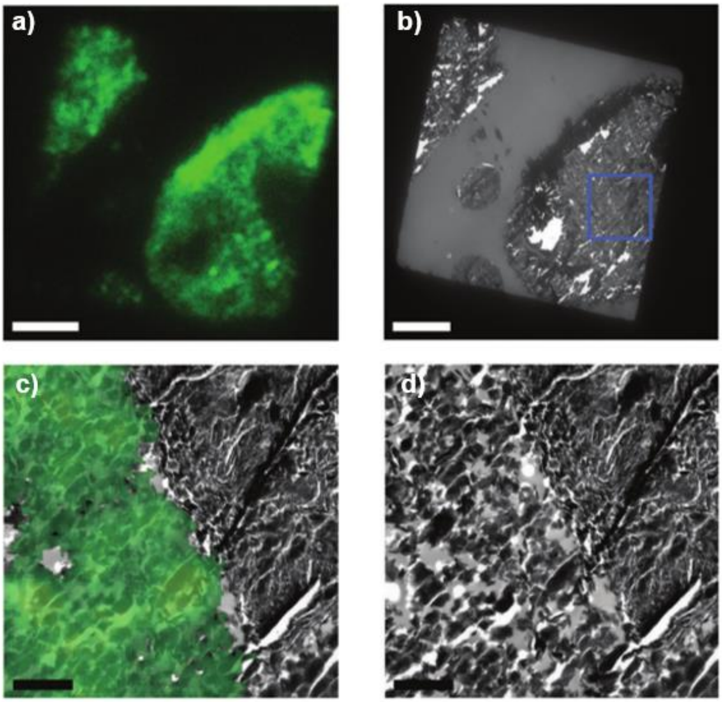

***Figure 1.9.*** *a) Confocal FM image of a sliced FCC catalyst sample, and b) the corresponding TEM image. Scale bars: 10 mm. c) The overlay image of the FM and TEM image in the area highlighted by the blue square in b) and d) the corresponding TEM image. Scale bars: 2 mm. Adapted with permission from ref.* [57]

Even though SRFM has been proven to be a powerful characterization technique for zeolite catalysts, the application of correlative SRFM and EM is less explored. Until 2017 there was only one correlative structure-activity investigation, performed by Karreman et al. to elucidate the catalytic activity distribution in fluid catalytic cracking (FCC) particles (**Figure 1.9**). The system of choice was an ILEM that combined TEM and CLSM (**Figure 1.1c**).[57,58] The configuration of this system and the required sample slicing do not allow nanoscale catalytic activity mapping. The authors therefore prestained the catalytic domains using the fluorogenic 4-fluorostyrene oligomerization reaction. Fluorescence intensity obtained from diffraction limited CLSM revealed the Brønsted acidity, which could be directly related to the structural organization of the FCC particles as observed by TEM. This revealed a heterogeneous distribution of the zeolite and matrix material in FCC particles and both structural and activity changes could be observed after hydrothermal deactivation that mimicked different life stages of the FCC catalyst.

## 1.3. Scope and outline

Correlative SRFM and SEM has been applied in catalysis research to unravel the effects of the intrinsically complex catalyst structure on its performance. This is achieved by linking nanoscale catalytic activity maps to the local structural context. So far, in every reported catalyst sample, such investigations have revealed the presence of pronounced inter- and intraparticle activity distributions that went unnoticed in traditional catalyst characterization. These heterogeneities are often the result of minute sub-particle structural features and defects. The structure-activity investigation in zeolite catalysis has until now been limited to the study of FCC catalyst particles using an ILEM that combines diffraction limited CLSM and TEM. The development of an integrated device that combines an SEM with a (SR)FM has the potential to accelerate research into the structure-activity relationship of zeolite catalysts. However, this field has so far been unexplored. In this PhD, such a device is developed and applied to investigate gradually more complex systems, ultimately allowing combined nanoscale activity mapping and structural imaging of zeolite catalysts.

In **Chapter 2**, this instrument has been applied to quantitatively investigate *in situ* UV induced silver co-catalyst photodeposition on ZnO dumbbell particles. This could only be achieved by developing a liquid cell that withstands the reduced pressure in the SEM chamber, and contains both an electron and optically transparent window. As such, the dynamic processes occurring at the photocatalyst surface sample could be studied with nanometer-scale resolution under realistic conditions.

By correlatively applying the developed ILEM, the facet dependent photocatalytic reactivity of two commonly encountered ZnO structures was explored at the single-particle level in **Chapter 3**. Silver (I) photoreduction to silver nanoparticles was used as a probe to link the photoreductive activity of ZnO to the local catalyst structural features. This required a nanoscale observation of the ZnO crystals before and after UV-induced silver deposition. Such studies would also be possible by using dedicated microscopes, but the related sample handling makes it time consuming and susceptible to sample contamination. The availability of an ILEM is therefore invaluable for this line of research.

Additional in-house adjustments to the ILEM enabled SRFM. For the first time, this allowed small-port mordenite catalyst structure to be linked to its performance at the nanoscale. This research is described in **Chapter 4** and was performed on an industrially applied zeolite batch composed of complex intergrown particles, as opposed to idealized micrometer-sized crystals. The significance of crystal intergrowths for catalyst performance was demonstrated both before and after acid leaching. Additionally, the effect of extensive acid leaching on the small-port behavior of mordenite zeolites was also studied.

**Chapter 5** is dedicated to the investigation of individual ZSM-22 catalyst particles. Their typical needle-shaped morphology originates from the lateral fusion of multiple nanorods. Based on indirect bulk scale experimenting, this lateral fusion has been shown to convert inactive Al-enriched external nanorod surfaces into catalytically active internal acid sites. The availability of the ILEM allowed a direct visualization of the effect of nanorod fusion on catalyst activity and shape-selectivity at the sub-particle level.

A conclusion to this PhD work and perspectives for future developments towards the determination of the structure-activity relationship in heterogeneous catalysts are provided in **Chapter 6**.

## 1.4. References

(1) Olaf, D.; Helmut, K.; Karl, K.; Thomas, T. In Ullmann's Encyclopedia of Industrial Chemistry; Bohnet, M., Ed.; John Wiley and Sons, 2014; pp 457–481.
(2) *Handbook of Heterogeneous Catalysis*; G., E., H., K., J., W., Eds.; Wiley-VCH, 1997.
(3) Somorjai, G. A.; Yimin, L. *Introduction to Surface Chemistry and Catalysis*, 2nd ed.; Wiley, 2010.
(4) Ertl, G. *Reactions at Solid Surfaces*, 1st ed.; Wiley, 2009.
(5) *Nanoparticles and Catalysis*, 1st ed.; Astruc, D., Ed.; Wiley-VCH, 2008.
(6) Hoffmann, M. R.; Martin, S. T.; Choi, W.; Bahnemannt, D. W. **1995**, 69–96.
(7) Chen, X.; Mao, S. S. **2007**.
(8) *Zeolites and Catalysis: Synthesis, Reactions and Applications*, 2nd ed.; Cejka, J., Corma, A., Jones, S., Eds.; Wiley-VCH, 2010.
(9) Industrial Catalysis: A Practical Approach; Hagen, J., Ed.; Wiley-VCH, 2006.
(10) *Metal Nanoparticles for Catalysis: Advances and Applications*; Franklin, T., Ed.; The Royal Society of Chemistry, 2014.
(11) The Chemical Physics of Solid Surfaces and Heterogeneous Catalysis, Vol. 4, 1st ed.; King, D. A., Woodruff, P. D., Eds.; 1982.
(12) Cordes, T.; Blum, S. A. *Nat. Publ. Gr.* **2013**, *5* (12), 993–999.
(13) Chen, P.; Zhou, X.; Andoy, N. M.; Han, K.-S.; Choudhary, E.; Zou, N.; Chen, G.; Shen, H. *Chem. Soc. Rev.* **2014**, *43* (4), 1107–1117.
(14) Janssen, K. P. F.; De Cremer, G.; Neely, R. K.; Kubarev, A. V.; Van Loon, J.; Martens, J. A.; De Vos, D. E.; Roeffaers, M. B. J.; Hofkens, J. *Chem. Soc. Rev.* **2014**, *43* (4), 990–1006.
(15) Buurmans, I. L. C.; Weckhuysen, B. M. *Nat. Chem.* **2012**, *4* (11), 873–886.
(16) Weckhuysen, B. M. *Chem. Soc. Rev.* **2010**, *39*, 4557–4559.
(17) Wang, W.; Gu, J.; He, T.; Shen, Y.; Xi, S.; Tian, L.; Li, F.; Li, H.; Yan, L.; Zhou, X. *Nano Res.* **2015**, *8* (2), 441–455.
(18) Roeffaers, M. B. J.; Sels, B. F.; Uji-I, H.; De Schryver, F. C.; Jacobs, P. a; De Vos, D. E.; Hofkens, J. *Nature* **2006**, *439* (7076), 572–575.
(19) Naito, K.; Tachikawa, T.; Fujitsuka, M.; Majima, T. *J. Phys. Chem. C* **2008**, *112*, 1048–1059.
(20) Xu, W.; Kong, J. S.; Yeh, Y.-T. E.; Chen, P. *Nat. Mater.* **2008**, *7* (12), 992–996.
(21) Roeffaers, M. B. J.; De Cremer, G.; Libeert, J.; Ameloot, R.; Dedecker, P.; Bons, A. J.; Bückins, M.; Martens, J. A.; Sels, B. F.; De Vos, D. E.; Hofkens,

J. *Angew. Chemie - Int. Ed.* **2009**, *48* (49), 9285–9289.

(22) De Cremer, G.; Sels, B. F.; De Vos, D. E.; Hofkens, J.; Roeffaers, M. B. J. *Chem. Soc. Rev.* **2010**, *39* (12), 4703–4717.

(23) Tachikawa, T.; Yamashita, S.; Majima, T. **2011**, 7197–7204.

(24) Weckhuysen, B. M. *Angew. Chemie - Int. Ed.* **2009**, *48* (27), 4910–4943.

(25) Sambur, J. B.; Chen, P. *Annu. Rev. Phys. Chem.* **2014**, *65* (1), 395–422.

(26) Kopek, B. G.; Paez-segala, M. G.; Shtengel, G.; Sochacki, K. A.; Sun, M. G.; Wang, Y.; Xu, C. S.; Engelenburg, S. B. Van; Taraska, J. W.; Looger, L. L.; Hess, H. F. *Nat. Publ. Gr.* **2017**, *12* (5), 916–946.

(27) de Boer, P.; Hoogenboom, J. P.; Giepmans, B. N. G. *Nat. Methods* **2015**, *12* (6), 503–513.

(28) Agronskaia, A. V.; Valentijn, J. A.; van Driel, L. F.; Schneijdenberg, C. T. W. M.; Humbel, B. M.; van Bergen en Henegouwen, P. M. P.; Verkleij, A. J.; Koster, A. J.; Gerritsen, H. C. *J. Struct. Biol.* **2008**, *164* (2), 183–189.

(29) Zonnevylle, A. C.; Van Tol, R. F. C.; Liv, N.; Narvaez, A. C.; Effting, A. P. J.; Kruit, P.; Hoogenboom, J. P. *J. Microsc.* **2013**, *252* (1), 58–70.

(30) Danilatos, G. D. In *Advcances in Electronics and Electron Physics*; Elsevier, 1988; Vol. 71, pp 109–250.

(31) Kolmakov, A. In *Liquid Cell Electron Microscopy*; Ross, F. M., Ed.; Cambridge University Press: Cambridge, 2017; pp 78–105.

(32) Nishiyama, H.; Suga, M.; Ogura, T.; Maruyama, Y.; Koizumi, M.; Mio, K.; Kitamura, S.; Sato, C. *J. Struct. Biol.* **2010**, *169*, 438–449.

(33) Hirano, K.; Kinoshita, T.; Uemura, T.; Motohashi, H.; Watanabe, Y.; Ebihara, T.; Nishiyama, H.; Sato, M.; Suga, M.; Maruyama, Y.; Tsuji, N. M.; Yamamoto, M.; Nishihara, S.; Sato, C. *Ultramicroscopy* **2014**, *143*, 52–66.

(34) Goldstein, J.; Newbury, D.; Joy, D.; Lyman, C.; Echlin, P.; Lifshin, E.; Sawyer, L.; Michael, J. *Scanning Electron Microscopy and X-Ray Microanalysis*, 3rd ed.; Springer, 2007.

(35) Thiberge, S.; Nechushtan, A.; Sprinzak, D.; Gileadi, O.; Behar, V.; Zik, O.; Chowers, Y.; Michaeli, S.; Schlessinger, J.; Moses, E. *PNAS* **2004**, *101*, 3346–3351.

(36) Thiberge, S.; Zik, O.; Moses, E. *Rev. Sci. Instrum.* **2004**, *75* (7), 2280–2289.

(37) Sato, C. In *Correlative Light and Electron Microscopy III*; Müller-Reichert, T., Verkade, P., Eds.; Elsevier, 2017; pp 187–211.

(38) Nishiyama, H.; Koizumi, M.; Ogawa, K.; Kitamura, S.; Konyuba, Y.; Watanabe, Y.; Ohbayashi, N.; Fukuda, M.; Suga, M.; Sato, C. *Ultramicroscopy* **2014**, *147*, 86–97.

(39) Liv, N.; Zonnevylle, A. C.; Narvaez, A. C.; Effting, A. P. J.; Voorneveld, P. W.; Lucas, M. S.; Hardwick, J. C.; Wepf, R. A.; Kruit, P.; Hoogenboom, J. P. *PLoS One* **2013**, *8* (2), 1–9.

(40) Liv, N.; Lazic, I.; Kruit, P.; Hoogenboom, J. P. *Ultramicroscopy* **2014**, *143*, 93–99.

(41) Liv, N.; Slingeland, D. S. B. V. O.; Baudoin, J.; Kruit, P.; Piston, D. W.; Hoogenboom, J. P. *ACS Nano* **2016**, *10*, 265–273.

(42) Zhou, X.; Andoy, N. M.; Liu, G.; Choudhary, E.; Han, K.-S.; Shen, H.; Chen, P. *Nat. Nanotechnol.* **2012**, *7* (4), 237–241.

(43) Shen, H.; Zhou, X.; Zou, N.; Chen, P. *J. Phys. Chem. C* **2014**, *118* (46), 26902–26911.

(44) Andoy, N. M.; Zhou, X.; Choudhary, E.; Shen, H.; Liu, G.; Chen, P. *J. Am. Chem. Soc.* **2013**, *135* (5), 1845–1852.

(45) Zhou, X.; Choudhary, E.; Andoy, N. M.; Zou, N.; Chen, P. *ACS Catal.* **2013**, *3*, 1448–1453.

(46) Li, R.; Zhang, F.; Wang, D.; Yang, J.; Li, M.; Zhu, J.; Zhou, X.; Han, H.; Li, C. *Nat. Commun.* **2013**, *4*, 1432.

(47) Debroye, E.; Van Loon, J.; Yuan, H.; Janssen, K. P. F.; Lou, Z.; Kim, S.; Majima, T.; Roeffaers, M. B. J. *J. Phys. Chem. Lett.* **2017**, *8*, 340–346.

(48) Tachikawa, T.; Wang , N.; Yamashita, S.; Cui, S.-C.; Majima, T. *Angew. Chemie Int. Ed.* **2010**, *49* (46), 8593–8597.

(49) Tachikawa, T.; Yamashita, S.; Majima, T. *J. Am. Chem. Soc.* **2011**, *133* (18), 7197–7204.

(50) Tachikawa, T.; Yonezawa, T.; Majima, T. *ACS Nano* **2013**, *7* (1), 263–275.

(51) Sambur, J. B.; Chen, T.-Y.; Choudhary, E.; Chen, G.; Nissen, E. J.; Thomas, E. M.; Zou, N.; Chen, P. *Nature* **2016**, *530* (7588), 77–80.

(52) Sambur, J. B.; Chen, P. *J. Phys. Chem. C* **2016**, *120* (37), 20668–20675.

(53) Tachikawa, T.; Ohsaka, T.; Bian, Z.; Majima, T. *J. Phys. Chem. C* **2013**.

(54) Cremer, G. De; Bartholomeeusen, E.; Pescarmona, P. P.; Lin, K.; Vos, D. E. De; Hofkens, J.; Roeffaers, M. B. J.; Sels, B. F. *Catal. Today* **2010**, *157* (1–4), 236–242.

(55) Michels, N.; Mitchell, S.; Pérez-Ramirez, J. *ACS Catal.* **2014**, *4*, 2409–2417.

(56) Whiting, G. T.; Chowdhury, A. D.; Oord, R.; Paalanen, P.; Weckhuysen, B. M. *Faraday Discuss.* **2016**, *188*, 369–386.

(57) Karreman, M. A.; Buurmans, I. L. C.; Geus, J. W.; Agronskaia, A. V.; Ruiz-Martínez, J.; Gerritsen, H. C.; Weckhuysen, B. M. *Angew. Chemie - Int. Ed.* **2012**, *51* (6), 1428–1431.

(58) Karreman, M. A.; Buurmans, I. L. C.; Agronskaia, A. V.; Geus, J. W.; Gerritsen, H. C.; Weckhuysen, B. M. *Chem. - A Eur. J.* **2013**, *19* (12), 3846–3859.

# Chapter 2

## Assessing Photocatalytic Activity at the Nanoscale Using Integrated Optical and Electron Microscopy

Elke Debroye,* **Jordi Van Loon**,* Xian Gu, Thomas Franklin, Johan Hofkens, Kris P.F. Janssen, Maarten B.J. Roeffaers

Adapted with permission from: *Part. Part. Syst. Charact.* **2016**, 33, 412–418

* Joint first authors

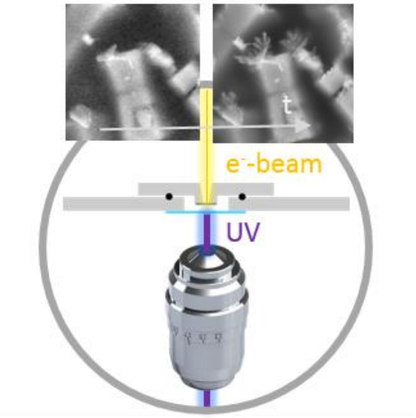

An integrated optical-electron microscope is presented that enables the *in situ* study of dynamic processes on photo-active materials. Here, the deposition of metallic silver nanostructures at ZnO photocatalyst particles is monitored in real time under ambient conditions by means of scanning electron microscopy. Zinc oxide crystals are immobilized on an electron transparent silicon nitride window. By passing UV light through an opposing optically transparent window, the zinc oxide is illuminated resulting in the photocatalytic formation of silver nanostructures. Both windows are part of a specially designed liquid cell filled with a dilute aqueous silver nitrate solution. Using the presented system, different electron detectors are evaluated for their ability to provide detailed images despite the interference caused by the liquid surrounding the sample. Special care has to be taken since direct silver reduction from solution induced by the electron beam interferes with the photocatalytic process. Oxygen gas, produced during to the photocatalytic reaction, is shown to also complicate the imaging of the dynamic nanoscale processes in the SEM. Nevertheless, the integrated approach allows to directly establish structure-activity relationships and to unravel optically induced processes at nanostructured materials.

## Contributions

E.D. and J.V.L. contributed equally to this work. Most of the experiments were performed and analyzed by E.D., J.V.L. and X.G. J.V.L., T.F. and K.P.F.J. were responsible for the development of the ILEM. Most of the article writing was done by E.D., J.V.L. and M.B.J.R. with contributions from all authors. All authors were involved in data interpretation.

# Chapter 2 - Assessing Photocatalytic Activity at the Nanoscale using Integrated Optical and Electron Microscopy

## 2.1. Introduction

Research into nanomaterials is strongly driven by their unique functional properties which strongly depend on size, morphology, organization and composition. As such, electron microscopy has become an indispensable research tool for studying nanoparticles, as it allows detailed structural characterization at relevant length scales. At this moment, however, it is not yet possible to directly link this detailed structural information to the functioning of the nanomaterials at the same length scale.

Heterogeneous nano-photocatalysts show promising results at the laboratory scale for applications in environmental remediation, as well as in the generation of fuels and organics.[1] There is evidence that the performance of photocatalytic nanomaterials is correlated to the structural and morphological features of individual catalyst particles.[2–4] Recently, we have reported on a simple method to generate dendritic silver nanostructures at the surface of ZnO crystals *via* the UV induced photocatalytic reduction of silver ions from an aqueous $AgNO_3$ solution (**Figure S2.1**).[5] These nanometer sized silver structures act as an efficient electron sink, rendering the dendrites into potential co-catalysts.[6–8] It is believed that the nucleation and growth of these silver dendrites is subject to intra- and inter-particle heterogeneities.[6,8–10] To investigate the photodeposition dynamically at the single photocatalyst particle level, an optical microscope is integrated into a scanning electron microscope (SEM) by means of a custom-made SEM chamber door (Secom, Delmic BV). This integrated instrument allows the *in situ* SEM observation and quantitative analysis of the deposition of silver co-catalysts under UV illumination. A crucial step towards this *in situ* observation is the development of a liquid cell that is equipped with both an electron and optically transparent window, while it is compatible with the reduced pressure in the sample chamber of the electron microscope. The general advantage of the developed wet sample holder for electron microscopy is the ability to image structural changes of materials under optical stimulation while keeping the samples under realistic conditions, i.e., atmospheric pressure and even wet conditions. As such, dynamic processes, in this study occurring at the photocatalyst surface under UV illumination, can be investigated with nanometer-scale detail provided by SEM. A similar sample holder was also used recently to image biological specimen simultaneously in fluorescence and electron microscopy.[11]

## 2.2. Experimental section

### 2.2.1. Materials and reagents

Zinc acetate dihydrate ($ZnO(CH_3COO)_2{\cdot}2H_2O$, ≥98.0%, Sigma-Aldrich), sodium hydroxide (NaOH, >99%, VWR Chemicals) and silver nitrate ($AgNO_3$, ≥99.0%, Sigma-Aldrich) were used as received without further purification. In the experimental processes, ultrapure water has been employed. Hydrothermal reactions were conducted in stainless steel Teflon-lined autoclaves in a Thermo Scientific Heratherm oven (OGS60). Solutions were dispersed in a 60 W Branson 2200 Ultrasonic bath equipped with thermostatic heating.

### 2.2.2. Synthesis ZnO dumbbells[12]

4.4 g of $ZnO(CH_3COO)_2{\cdot}2H_2O$ is dissolved in 20 mL of milli Q water under vigorous stirring. The pH of the clear zinc acetate solution was adjusted to pH 8 with a 4 M aqueous NaOH solution. The resulting reaction mixture was then transferred to a 30 mL stainless steel Teflon-lined autoclave and heated to 155 °C where the mixture was kept for 48 hours. After cooling down to room temperature, the solid product was filtered from the reaction liquid. The resulting crystals were thoroughly washed with milli Q water and dried overnight in an oven at 80 °C *prior* to use.

### 2.2.3. Characterization

Morphologies and sizes of the samples were analyzed by a FEI Quanta 250 FEG environmental scanning electron microscope with a customized chamber door (SECOM, Delmic BV). UV light (365 nm) from an LED source outside the vacuum chamber can pass through the door by means of an optically transparent chamber window. The LED source consists of a Thorlabs LEDD1B, T-Cube LED Driver of 365 nm. A dichroic mirror and a 100x 1.4 NA CFI plan APO VC oil objective (Nikon) further direct the UV light onto the sample at the sample stage with an optical power density of 50.0 $\mu W/cm^2$.

### 2.2.4. Liquid cell experiments

The electron transparent $Si_3N_4$ windows used in the *in situ* silver dendrite growth experiments are bought from Silson Ltd. They can be purchased with thicknesses of 30 or 50 nm, either with a square or rectangular shape: 0.1 mm x 0.3 mm, 0.1 mm x 0.1 mm, 0.2 mm x 0.2 mm and 0.25 mm x 0.25 mm membranes. In order to spread the ZnO crystals uniformly over the $Si_3N_4$ window's surface, the $Si_3N_4$ window was placed in an UV-ozone photo reactor (PR-100) for several minutes to make the surface more hydrophilic. A suspension of 3 mg/mL of the ZnO dumbbells in ultrapure water was shaken thoroughly and dispersed in an ultrasonic water bath for 1 minute. Then, 5 µL of this suspension was dropcasted on top of the window, resulting in a thin and uniform layer of ZnO crystals. A droplet of 50 µL of a 10 mM $AgNO_3$

solution was put on top of the ZnO microparticles and the sample holder was properly sealed before mounting into the SEM chamber.

## 2.3. Results and discussion

### 2.3.1. Integrated light- and electron microscopy

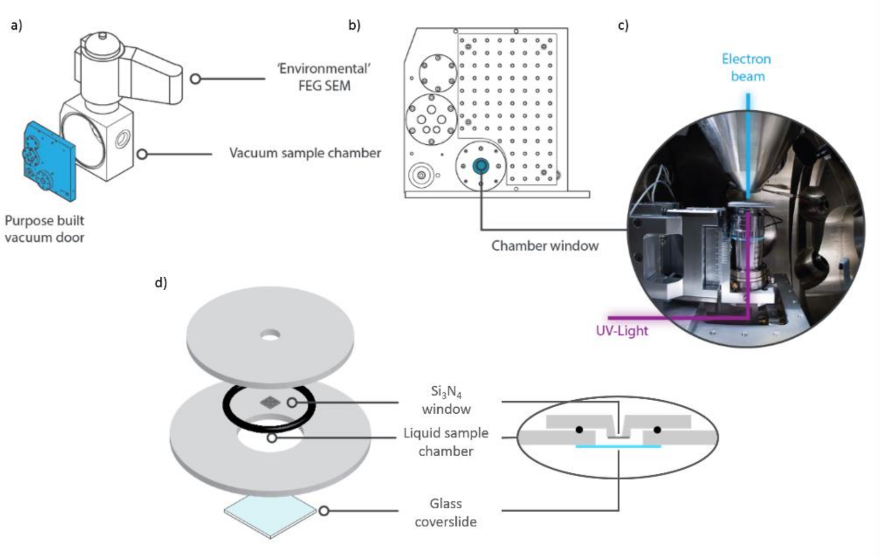

***Figure 2.1.*** *The integrated light- and electron microscope used in these experiments is equipped with a) a customized chamber door (Delmic BV) holding b) an optically transparent window. This chamber window allows 365 nm UV light from the outside to reach the c) high NA objective lens inside the vacuum chamber, guiding the light onto the field of view that is being imaged by SEM. In order to enable the in situ observation of the photocatalytic silver deposition, d) a dedicated sample holder has been developed.*

The integrated light- and electron microscope used in this research consists of a FEI Quanta 250 FEG environmental SEM, equipped with the SECOM platform provided by Delmic BV (**Figure 2.1a**).[13,14] This configuration allows 365 nm UV light from an LED source (Thorlabs) outside of the vacuum chamber, to be coupled in *via* an optically transparent window (**Figure 2.1b**). Inside the vacuum chamber (**Figure 2.1c**), a high NA objective lens (Nikon Plan APO VC 100x, 1.4 NA) enables sample illumination from the bottom, i.e., opposite to the electron gun located above the sample. Such a configuration allows to study *in situ* the photodeposition of metallic silver nanoparticles at the ZnO photocatalysts in an SEM. The possibility of conducting these experiments in one and the same setup implies that sample contamination or alteration can be minimized since there is no need for shuttling the sample between dedicated setups. As to enable the *in situ* investigation, a dedicated liquid cell has been developed (**Figure 2.1d**) to allow the immersion of the photocatalytic material in an aqueous silver nitrate solution while inside the vacuum of the SEM sample chamber. This liquid cell consists of a glass cover slip at the bottom and a 50 nm thick electron transparent $Si_3N_4$ window (Silson Ltd.) at the top of the cell. Both windows are held together by two metal plates that are separated by an O-ring to ensure proper sealing and spacing, resulting in a cell volume of 50 µL. The photocatalyst material is deposited on the $Si_3N_4$ surface facing the inside of the liquid cell, where it is submersed in the reagent solution if the cell is completely filled. In this approach, the integrated optical microscope enables to restrict the photo-stimulation of ZnO crystals to the field of view. Without this spatial control, and while maintaining the same UV photon flux, photocatalyst activation and oxygen formation would be induced on all ZnO crystals, including those outside the field of view. With this setup it is certainly possible to directly correlate optical images to the detailed scanning electron micrographs. As illustration, optical transmission images of silver nanostructures photo-deposited on ZnO particles can be consulted in **Figure S2.3** in the Supporting Information. Clearly, the amount of detail resolved in the SEM images surpasses the typical diffraction limited optical images.

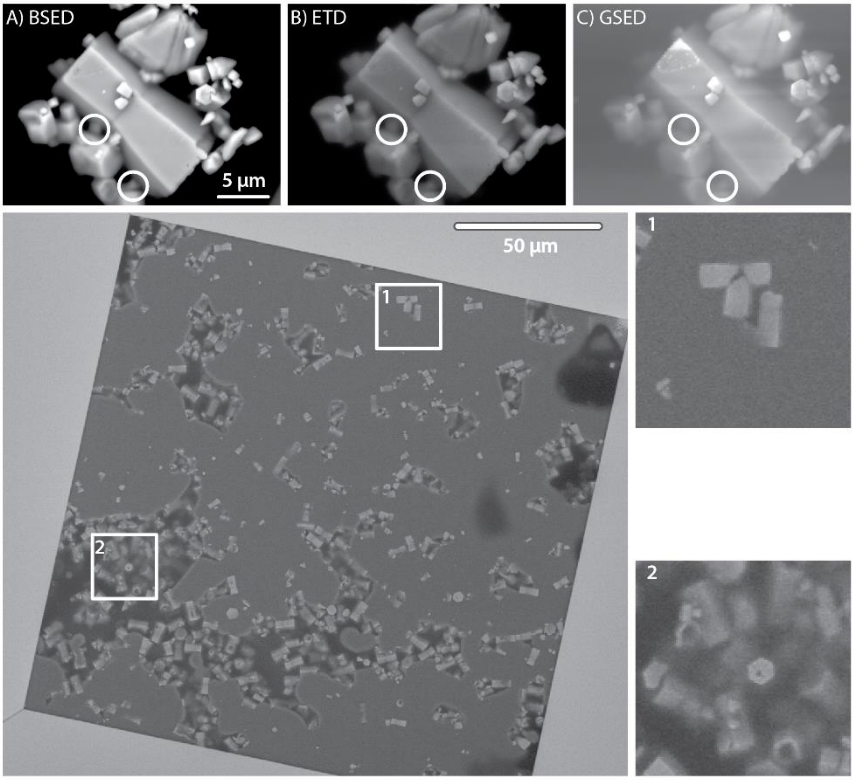

***Figure 2.2.*** *SEM images of ZnO particles obtained with a a) BSED, b) ETD and c) GSED (2 mbar) to demonstrate resolution differences when imaging through a 50 nm thick* $Si_3N_4$ *window at 20 kV acceleration voltage and spot size 4. The gray circles*

*highlight structures revealing resolution in depth. The images are ordered according to decreasing resolution. d) Influence of the presence of liquid on the signal-to-noise ratio during SEM imaging with an ETD in an inadequately assembled liquid cell.*

During imaging in the liquid cell, the electron beam has to pass through a 50 nm thick $Si_3N_4$ window in order to reach the sample surface. This will lead to increased electron scattering and decreasing signal-to-noise ratio, hence, resolution loss is inevitable.[a,15,16] Image resolution for different imaging modes is typically investigated using gold nanoparticles dispersed on a $Si_3N_4$ window, as has been discussed for biological samples by Liv et al.[11] This study led to the general conclusion that back scattered electron detection (BSED) at 20 kV is mostly suited to obtain the highest possible resolution in the lateral dimension. By using small-sized gold nanoparticles, however, no information on the axial resolution is obtained. Furthermore, as biological samples are mostly composed of organic structures, contrast differentiation based on the atomic weight is limited compared to higher atomic number elements typically making up inorganic samples. As such, there is limited information concerning the effect of different SEM detectors on the axial imaging performance on semiconductor materials as used in this work. In **Figure 2.2a-c**, a comparison between the imaging capacity of a BSED, an Everhart-Thornley Detector (ETD) and a Gaseous Secondary Electron Detector (GSED) is made for an ensemble of ZnO particles deposited below the 50 nm thick $Si_3N_4$ window. These images are obtained with a 20 kV acceleration voltage and spot size 4, in the absence of liquid. Note that the GSED image (**Figure 2.2c**) is captured at an increased chamber pressure of 2 mbar. When targeting structural features close to the $Si_3N_4$ window, the resolution obtained with all three detectors is very similar. However, the ETD and GSED images rapidly become blurry with increased imaging depth, whereas crystal features further away from the $Si_3N_4$ window remain sharp in the BSED image. For example, based on the shape and dimensions of the central ZnO crystal, it can be estimated that the crystalline structures highlighted with the gray circles in **Figure 2.2a-c** are located approximately 2.4 µm below the $Si_3N_4$ window. Clearly, these structures are best resolved in **Figure 2.2a**, which corresponds to previous findings that the BSED detector is preferred for imaging through a $Si_3N_4$ window although the differences are minimal. The more pronounced resolution loss at extended imaging depths in secondary electron (SE) images compared to BSE images can be explained by a combined effect of the higher absorption of low energy secondary electrons by the $Si_3N_4$ window and the general decreased signal that is generated from lower lying structures.

The structures in direct contact with the $Si_3N_4$ window in **Figure 2.2a-c** show signs of charging at the ZnO crystals, as the detector signal is locally saturated. This charging will be effectively reduced once the sample holder is filled with liquid. The presence of a liquid, water in these experiments, will

---

[a] See Annex to Chapter 2, p 37

however in its turn lead to increased scattering. Therefore, in the next step, the effect of an aqueous reagent solution on the imaging quality in the liquid cell is investigated. In **Figure 2.2d**, a mounted liquid cell is shown in which a major part of the ZnO crystals is submersed in the aqueous solution, e.g. inset (1). Clearly, only structures that are in close contact with the $Si_3N_4$ surface can be imaged. A fraction of the ZnO particles are, however, still contained within residual air pockets, e.g. inset (2), and are characterized by an increased imaging depth. This example clearly demonstrates the exact effect of drastically increased electron beam scattering on the imaging quality. Despite the inherent loss of imaging depth when samples are effectively submersed in a liquid, the crystal areas within close vicinity of the $Si_3N_4$ window can still be observed at the nanoscale. Further, air pockets underneath the $Si_3N_4$ window need to be avoided if the photocatalytic silver deposition is to be quantitatively investigated.

### 2.3.2. Impact of electron beam

It has been reported that electron beam irradiation can initiate metal deposition on both semiconductors and non-conductive surfaces by the direct reduction of metal ions even in absence of a photocatalytic process.[17–19] Therefore, the impact of the electron beam needs to be minimized to correctly interpret the *in situ* photocatalytic silver deposition experiments. The direct electron beam induced metal deposition from an aqueous $AgNO_3$ solution was assessed by scanning the electron beam over ZnO crystals submersed in a 10 mM aqueous $AgNO_3$ solution through a 50 nm thick $Si_3N_4$ window without any UV illumination. The results of this experiment are depicted in **Figure 2.3**. Whereas the initial overview image (**Figure 2.3a**) does not show any signs of silver nanoparticle deposition on the ZnO crystals, a first magnified image (**Figure 2.3b**) clearly reveals the presence of metallic silver nanostructures at the top of the crystals, induced by locally focusing the electron beam. Continued irradiation causes additional growth of the existing silver nanostructures up to several micrometers in size. This process is clearly observed in **Figure 2.3c and d**, displaying SEM images after 40 and 80 seconds of continuous scanning electron micro-imaging. After these series of magnified images, an overview image was taken of the initial field of view (FOV) (**Figure 2.3e**). The dashed square highlights the presence of a light gray area on the $Si_3N_4$ window which corresponds to the reduced FOV used to image in **Figure 2.3b-d**. A closer look at the regions around the ZnO crystal in the magnified images (**Figure 2.3b-d**) reveals the gradual appearance of silver deposits on the $Si_3N_4$ window.[18,19] In an additional experiment, the electron beam was deliberately focused in spot mode onto the ZnO crystal depicted in **Figure 2.3f**. The red cross in the schematic representation indicates the electron beam position. In this case an even more extended and branched silver structure is formed at the location of the electron beam.

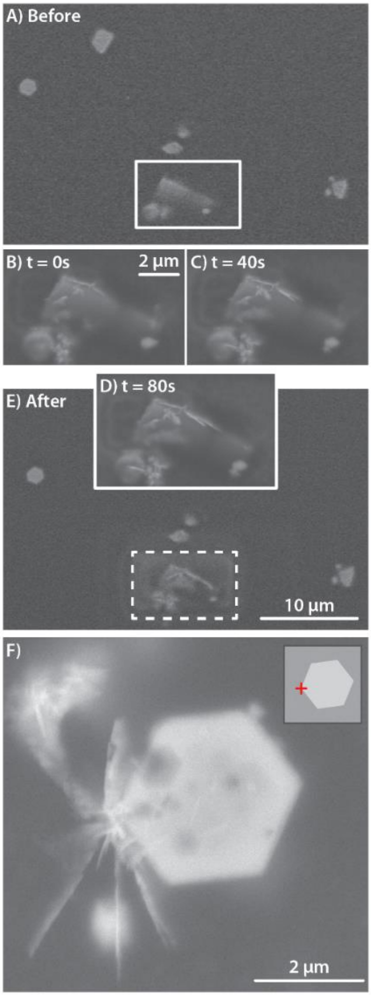

***Figure 2.3.*** *SEM images of electron beam induced silver deposition recorded with an ETD. (a) Overview image of the initial stage of ZnO crystals in the liquid cell. Magnified SEM micrographs of two crystals after (b) 0 s, (c) 40 s and (d) 80 s of continuous electron beam irradiation, showing metallic silver deposition on the ZnO crystals. (e) An SEM micrograph of the same FOV as shown for the initial stage, suggesting the presence of silver deposition on the $Si_3N_4$ window. (f) BSED image of the silver deposition induced by the electron beam in spot mode focused at the corner of the ZnO particle as indicated by the red cross in the schematic representation.*

These initial liquid cell experiments in absence of UV illumination clearly show the ability of an electron beam to induce metallic silver deposition from a dilute aqueous $AgNO_3$ solution used for photodeposition experiments. This process needs to be minimized to avoid interference with *in situ* photodeposition studies. An indication of the electron beam impact can be obtained by calculating the photon-to-electron ratio for the *in situ* experiment. As the photocatalyst is irradiated with 50 µW.cm$^{-2}$ of 365 nm UV light during the 120 s movie, approximately $1.1 \cdot 10^{16}$ photons reach the sample FOV (32.8 x 32.8 $\mu m^2$). In order to obtain sufficiently resolved SEM images of the silver photodeposition, and this at reasonable frame rates, a pixel dwell time of 10 µs and a 786 x 512 image size have been selected in combination with a 20 kV acceleration voltage and spot size 3. This results in a frame rate of 0.25 Hz and yields a current of 180 nA. Hence, during the acquisition of a 120 s movie, approximately $1.4 \cdot 10^{11}$ electrons reach the sample FOV (43.5 x 29 $\mu m^2$). Based on this, the photon-to-electron ratio for the applied experimental conditions can be calculated to exceed $8 \cdot 10^4$. However, it is merely an estimation of the photon-to-electron flux in the sample, as interaction of the electron beam with the liquid contained sample is complex. Besides electron scattering and absorption resulting in a decreased amount of electrons effectively reaching the ZnO particle, inelastic scattering and the creation of hydrated electrons result in additional electrons reaching the ZnO surface.[20] Additionally, the effectiveness with which electrons and photons lead to metal deposition needs to be considered. An in-depth investigation into these phenomena is not trivial and falls outside the scope of the current study, but will be necessary if detailed quantitative analysis of integrated experiments is required.

### 2.3.3. *In situ* silver photodeposition

After determining the suitable imaging conditions, the first photocatalytic experiment was performed inside the SEM. ZnO crystals were drop casted from an aqueous suspension onto the $Si_3N_4$ window, and after drying, the liquid cell was assembled containing 50 µl of an aqueous 10 mM $AgNO_3$ solution and properly sealed (see Supporting Information for a more detailed explanation). After mounting the liquid cell into the SEM, a 120 seconds movie was acquired with the conditions as described above (see Supporting Movie S1).

**Figure 2.4a** shows the first frame of the SEM movie, after which UV irradiation was initiated. Two crystals of interest are analyzed in depth, i.e., the central vertically oriented dumbbell crystal and the horizontally oriented dumbbell crystal at the top center of the image, both indicated by white squares. Magnifications of these crystals of interest are shown after 0 s, 40 s, 80 s and 120 s of UV irradiation in **Figure 2.4b-e** and **Figure 2.4f-i** respectively. The full image obtained after 120 seconds is shown in **Figure 2.4j**. Additionally, after acquiring the movie, the two crystals of interest were imaged in more detail as is shown in **Figure 2.4k and l**. These images are obtained independently from the movie and are aimed at providing more detailed information on the size, number and location of the silver nanoparticles formed at the ZnO surface.

From **Figure 2.4b**, taken before the UV irradiation was started, it is evident that some silver deposition has already occurred at the top left edge of the crystal. This local deposit was caused by focusing the electron beam on this particular location *prior* to the movie acquisition. Over the course of the movie, photo-induced silver dendrite growth is observed to continue at this silver deposit which acts as an efficient electron sink (**Figure 2.4b-e**). Additionally, the photodeposition leads to silver nanoparticles deposited at the ZnO crystal edges (**Figure 2.4k**). Also for the second crystal the SEM focusing *prior* to the photodeposition experiment leads to some silver nanoparticle depositions however this crystal does not show the subsequent formation of extended silver dendrite structures (**Figure 2.4f-i**). Silver photodeposition mainly leads to nanoparticle formation predominantly located at the crystals' edges. This deposition can be nicely tracked over the course of the movie and the image acquired afterwards (**Figure 2.4l**) clearly shows the size and shape of these metal nanoparticles.

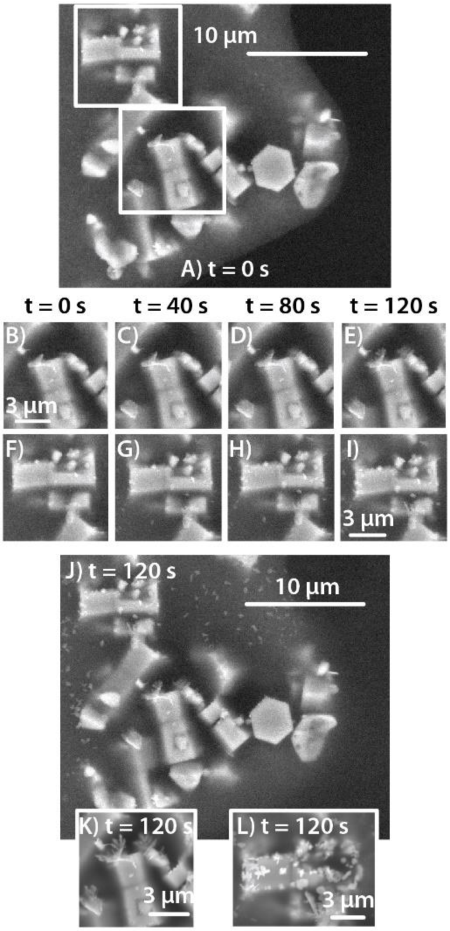

***Figure 2.4.*** *Scanning electron micrographs of (a) the first and (j) the last frame of a 120 s movie of the in situ photo-induced silver metal deposition on ZnO dumbbell-shaped crystals. (b-e) and (f-i) depict enlarged images of two crystals of interest after*

*0 s, 40 s, 80 s and 120 s of UV light illumination. (k) and (l) show SEM images of both crystals after the in situ experiment, acquired with optimized imaging settings. All images are obtained using the GSED.*

The background in **Figure 2.4a and j** is inhomogeneous. Whereas the left part is light gray, the right part is darker gray and both areas are separated by a sharp interface. This difference can be explained by the difference in media present in both areas. Whereas ZnO particles at the left side are in a gaseous environment, as indicated by the increased imaging depth, the particles at the right side of the image are still submersed in the reagent solution. This color assignment is opposite to what was observed earlier in **Figure 2.2d** and is attributed to the use of the GSED detector in the liquid cell experiment. With the GSED detector, imaging samples at atmospheric pressure (**Figure 2.2c**) typically leads to a gray background as a result of the increased environmental pressure in the sample holder; this in contrast to the dark background obtained with other detectors (**Figure 2.2a-b**). Furthermore, the interface between the gaseous environment and the liquid moves towards the right during the experiment, due to the intrinsic oxygen generation by the photocatalytic reaction (**Equation 1 and 2**).

$$Ag^{+} + e^{-} \rightarrow Ag^{0} \qquad \textbf{(1)}$$

$$2H_2O + 4h^{+} \rightarrow O_2 + 4H^{+} \qquad \textbf{(2)}$$

This local oxygen accumulation does, however, not seem to hamper further observation of the photodeposition process as continuous growth of Ag nanoparticles at the left part of the image is still visible. This observation can be explained by a residual aqueous film that surrounds the ZnO photocatalysts. Since gas formation is inherent to this photocatalytic experiment, further adaptation of the wet sample holder design could be considered to minimize the accumulation of air pockets underneath the $Si_3N_4$ window.

Another important observation at the left part of the image is the gradual appearance of whitish spots which can only be linked to silver nanoparticle formation at the $Si_3N_4$ window. This is in agreement with literature reports on the characterization of *in situ* metal nanoparticle growth on $Si_3N_4$ windows under electron beam irradiation in scanning or transmission electron microscopy.[17–19] These spots were not observed before in our lab when studying the silver photodeposition in a regular optical microscope (**Figure S2.2**) and they do not appear in the area where the $Si_3N_4$ window is still fully wetted by the aqueous silver nitrate solution. It is thus very likely that the local silver reduction by the scanning electron beam leads to this nanoparticle formation. In the residual thin aqueous film, present at the left hand side of the image, these nanoparticles are trapped whereas at the right hand side, the nanoparticles seem to be efficiently removed from the window due to gravity and convection. Note that in **Figure 2.3b-d**, where the effect of the electron beam on a ZnO photocatalyst was evaluated, also similar silver nanoparticle deposits at the $Si_3N_4$ window can be observed. In this reduced field of view, the local electron dose was much higher than in this experiment, resulting in silver nanoparticles which were not (efficiently) removed by the surrounding liquid.

Clearly, when the electron beam passes through the $Si_3N_4$ window and interacts with the liquid, a complex combination of phenomena occurs simultaneously. Physically, the electron beam can induce convection which is caused by the transfer of momentum and heat from the electron beam to the system.[16,21] Chemically, the electron beam can create ions, free radicals and hydrated electrons, which can subsequently lead to secondary chemical reactions.[20] Therefore, it is important to mention that it is not yet possible to straightforwardly quantify this kind of *in situ* photocatalytic experiments as the individual physical and chemical processes initiated by the electron beam are not yet fully understood.[22]

## 2.4. Conclusion

The novel integrated light- and electron microscope is successfully applied in combination with a liquid cell to visualize silver nanostructure photodeposition on ZnO crystals in real time inside the vacuum conditions of the SEM chamber. Initially, the imaging quality obtained with different detectors through a 50 nm thick $Si_3N_4$ window and the presence of a liquid inside the imaging cell was checked. Further, we observed that the electron beam has a non-negligible contribution to the silver deposition from a $AgNO_3$ solution. Nevertheless, the described research is a first step towards the real time investigation of the structure-activity relationship of dumbbell-shaped ZnO crystals and other photocatalysts. Here the silver co-catalyst photodeposition can act as a probe reaction for determining reduction hotspots at the photocatalytic surface. There is clearly still room to further optimize the experimental conditions. A deeper investigation into different imaging conditions is needed in order to reduce the impact of the electron beam and an improved liquid cell design might reduce the formation of air pockets underneath the $Si_3N_4$ window. In general, a more thorough understanding and quantification of the microscale processes which are induced by the highly energetic electron beam is necessary.

Ultimately, this line of research will lead to extremely accurate and insightful information on the structure-activity relationship of varying optically active materials under realistic conditions, i.e., atmospheric pressure and even submersed in liquid.[23] A direct extension of the research described in this paper would be the observation of different dendrite growth rates on distinct crystallographic features, e.g. crystal edges or defects. Further optimization of the liquid cell will moreover allow photocatalytic performance studies of nanostructured materials by means of fluorogenic reactions, revealing the structure-activity relationship with super-resolution precision. Clearly, the developed integrated approach is superior to the commonly applied bulk experiments, since indirect measurements only provide ensemble averaged information and fail to capture the underlying molecular processes.

## 2.5. References

(1) Chatterjee, D.; Dasgupta, S. *J. Photochem. Photobiol. C Photochem. Rev.* **2005**, *6* (2–3), 186–205.

(2) Tachikawa, T.; Yamashita, S.; Majima, T. *J. Am. Chem. Soc.* **2011**, *133* (18), 7197–7204.

(3) Chen, P.; Zhou, X.; Shen, H.; Andoy, N. M.; Choudhary, E.; Han, K.-S.; Liu, G.; Meng, W. *Chem. Soc. Rev.* **2010**, *39* (12), 4560–4570.

(4) Sambur, J. B.; Chen, P. *Annu. Rev. Phys. Chem.* **2014**, *65* (1), 395–422.

(5) Laurier, K. G. M.; Poets, M.; Vermoortele, F.; Cremer, G. De; Martens, J. a.; Uji-i, H.; De Vos, D. E.; Hofkens, J.; Roeffaers, M. B. J. *Chem. Commun.* **2012**, *48*, 1559.

(6) Chan, S. C.; Barteau, M. a. *Langmuir* **2005**, *21* (12), 5588–5595.

(7) Maicu, M.; Hidalgo, M. C.; Colón, G.; Navío, J. A. *J. Photochem. Photobiol. A Chem.* **2011**, *217* (2–3), 275–283.

(8) Dunn, S.; Sharp, S.; Burgess, S. *Nanotechnology* **2009**, *20* (11), 115604.

(9) Matsumoto, Y.; Ida, S.; Inoue, T. *J. Phys. Chem.* **2008**, *112*, 11614–11616.

(10) Pacholski, C.; Kornowski, A.; Weller, H. *Angew. Chemie - Int. Ed.* **2004**, *43* (36), 4774–4777.

(11) Liv, N.; Lazic, I.; Kruit, P.; Hoogenboom, J. P. *Ultramicroscopy* **2014**, *143*, 93–99.

(12) Wen, F.; Li, W.; Moon, J. H.; Kim, J. H. *Solid State Commun.* **2005**, *135* (1–2), 34–37.

(13) Liv, N.; Zonnevylle, A. C.; Narvaez, A. C.; Effting, A. P. J.; Voorneveld, P. W.; Lucas, M. S.; Hardwick, J. C.; Wepf, R. A.; Kruit, P.; Hoogenboom, J. P. *PLoS One* **2013**, *8* (2), 1–9.

(14) Zonnevylle, A. C.; Van Tol, R. F. C.; Liv, N.; Narvaez, A. C.; Effting, A. P. J.; Kruit, P.; Hoogenboom, J. P. *J. Microsc.* **2013**, *252* (1), 58–70.

(15) Klein, K. L.; Anderson, I. M.; De Jonge, N. *J. Microsc.* **2011**, *242* (2), 117–123.

(16) de Jonge, N.; Ross, F. M.; Jonge, N. De; Ross, F. M.; de Jonge, N. *Nat Nanotechnol* **2011**, *6* (11), 695–704.

(17) Eugenii U., D.; Schardein, G.; Wright, J. C.; Hastings, J. T. *Nanoscale* **2011**, *3* (7), 2709–2717.

(18) Halka, V.; Schmid, M. J.; Avrutskiy, V.; Ma, X.; Schuster, R. *Angew. Chemie - Int. Ed.* **2011**, *50* (20), 4692–4695.

(19) Zheng, H. M.; Smith, R. K.; Jun, Y. W.; Kisielowski, C.; Dahmen, U.; Alivisatos, A. P. *Science* **2009**, *324* (5932), 1309–1312.

(20) White, E. R.; Mecklenburg, M.; Singer, S. B.; Aloni, S.; Regan, B. C. *Appl. Phys. Express* **2011**, *4* (5), 3–6.

(21) Marks, L. D.; Zhang, J. P. *Ultramicroscopy* **1992**, *41* (4), 419–422.

(22) Jensen, E.; Købler, C.; Jensen, P. S.; Mølhave, K. *Ultramicroscopy* **2013**, *129*, 63–69.

(23) Debroye, E.; Van Loon, J.; Yuan, H.; Janssen, K. P. F.; Lou, Z.; Kim, S.; Majima, T.; Roeffaers, M. B. J. *J. Phys. Chem. Lett.* **2017**, *8*, 340–346.

## 2.6. Supporting information

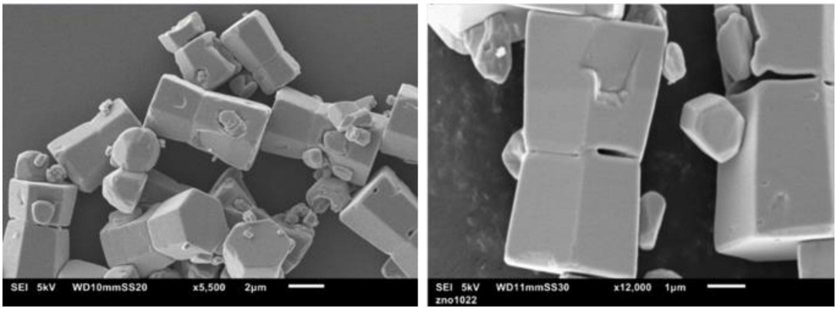

***Figure S2.1.*** *SEM images of typical dumbbell-shaped ZnO microcrystals as prepared.*

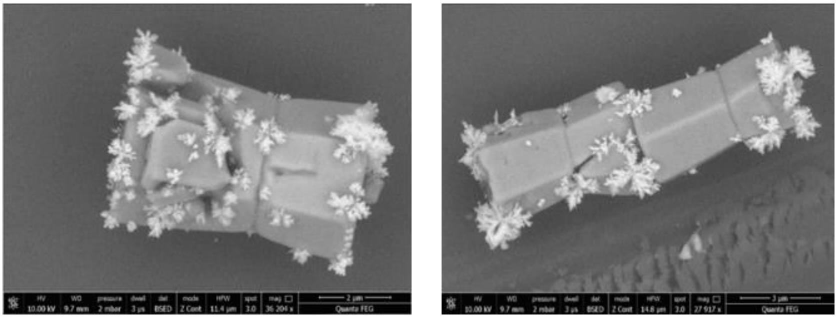

***Figure S2.2.*** *SEM images of ZnO dumbbell crystals after photodeposition of silver nanostructures with UV light for 20 seconds.*

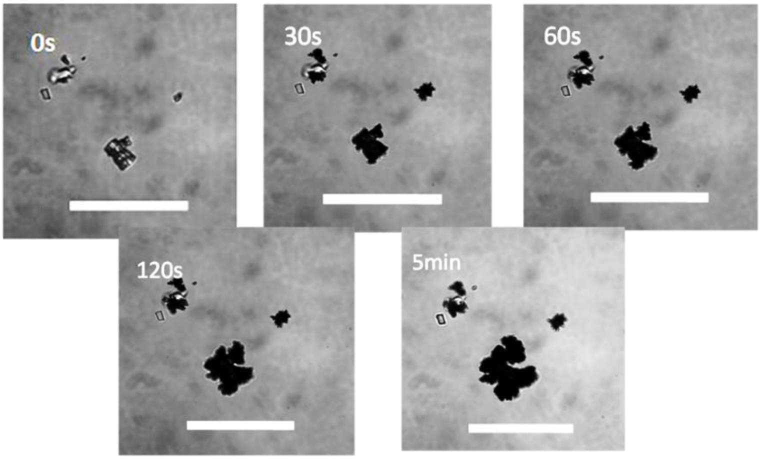

***Figure S2.3.*** *Optical transmission images of silver dendrite growth under influence of UV irradiation. Images are obtained at different time intervals, as indicated in the sub-images. Scale bar = 30 µm.*

Link to the movie available from the Wiley Online Library: https://www.dropbox.com/sh/wxuafuifpqis3du/AACylwLI0cyX5CdTGxxEh1h7a?dl=0

# Annex to Chapter 2

*During the preliminary defense of this PhD manuscript, a discussion on the use of different electron transparent windows and the imaging performance through such windows was requested.*

When performing SEM on a sample contained in a liquid cell, the electron transparent window compromises the imaging resolution.[1] The first successful application of a liquid cell relied on the use of a reinforced 145 nm thick polyimide window.[2] However, nowadays $Si_3N_4$ membranes are typically used for this purpose to increase the imaging resolution as it is easily manufactured with even thinner membranes, homogeneous composition and thickness.[3] Developments in the semiconductor industry further add to the performance of $Si_3N_4$ based liquid cells. For example, electrodes can now be incorporated onto the membranes, enabling *in situ* investigations of electrochemical reactions.[4]

Current attempts to further increase the performance of liquid phase SEM are focused on applying state of the art materials such as graphene oxide, graphene and boron nitride.[1] Using these materials could increase imaging resolution due to their reduced atomic number and the possibility to manufacture them in single atomic layers with high breaking strengths. Not only would resolution be improved, also reduced electron beam energies could be used, reducing the excitation volume, sample damage and charging. However, their use is not yet straightforward. It is difficult to deposit and seal a material of a single atomic layer onto a liquid cell without introducing defects and the dimensions of the electron transparent membrane should be reduced. Additionally, an important consideration towards the applicability of graphene as electron transparent material in an ILEM is its tendency to quench fluorescence.[5]

When performing SEM on samples in liquid, moderate electron beam energies are typically applied (< 50 kV) to investigate samples in close vicinity to the electron transparent membrane. The resolution is therefore determined by the interaction volume of the backscattered electrons (BSE) which results from the nature of the sample, the surrounding liquid, the thickness and atomic number of the electron transparent membrane and the acceleration voltage used for imaging purposes.[1]

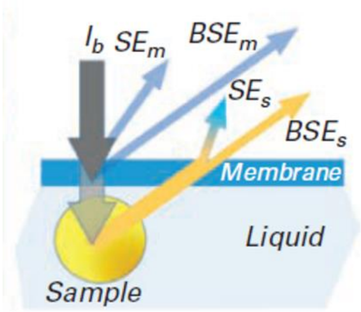

***Figure A1.1**. The major electron imaging signals generated when imaging a sample in liquid through a $Si_3N_4$ window. $I_b$ = incident beam, BSE = backscattered electrons, SE = secondary electrons, m = membrane, s = sample. Reproduced with permission from Ref.* [1]

To better understand contrast generation upon imaging through a $Si_3N_4$ window, the multiple interactions of electrons with the different components need to be considered (**Figure A1.1**). Electron scattering at the window broadens the electron beam.[6] This effect was found to be minor; the beam diameter only broadened up to 3 nm when imaging through a 50 nm thick $Si_3N_4$ window with 20 kV. Furthermore, electrons are also scattered in the backward and forward directions.[2,6,7] In the backward direction, BSE's and SE's ($SE_m$ and $BSE_m$) give rise to background signals on both the BSE and ETD detectors. A homogeneous contribution is obtained on the ETD as the composition and thickness of the membrane is homogeneous and only SE's generated in the first few nanometers of the $Si_3N_4$ window can escape from the membrane. On the other hand, unscattered primary beam electrons and highly energetic forward scattered electrons exiting the membrane interact with the sample and give rise to SE and BSE signals ($SE_s$ and $BSE_s$). Even though SE's are insufficiently energetic to leave the liquid cell, a detectable SE signal might still be generated from the sample due to the interaction of BSE's with the membrane. BSE's on the other hand, are sufficiently energetic to travel through the membrane, resulting in the superior performance of the BSED for imaging samples contained in a liquid cell, through an electron transparent membrane.

A minimal primary electron beam energy is required to penetrate the $Si_3N_4$ window and image the lower lying samples. However, as increasing the primary beam energy leads to an increased penetration depth, the beam might even probe through the sample, increasing unwanted phenomena such as solvent heating. Therefore, optimal imaging conditions apply depending on the system under investigation. de Nishiyama et al. found that 20 kV was optimal for imaging Au nanoparticles in water through a 50 nm thick $Si_3N_4$ window.[8]

## References

(1) Kolmakov, A. In *Liquid Cell Electron Microscopy*; Ross, F. M., Ed.; Cambridge University Press: Cambridge, 2017; pp 78–105.

(2) Thiberge, S.; Nechushtan, A.; Sprinzak, D.; Gileadi, O.; Behar, V.; Zik, O.; Chowers, Y.; Michaeli, S.; Schlessinger, J.; Moses, E. *PNAS* **2004**, *101*, 3346–3351.

(3) Liv, N.; Slingeland, D. S. B. V. O.; Baudoin, J.; Kruit, P.; Piston, D. W.; Hoogenboom, J. P. *ACS Nano* **2016**, *10*, 265–273.

(4) de Jonge, N.; Ross, F. M.; Jonge, N. De; Ross, F. M.; de Jonge, N. *Nat Nanotechnol* **2011**, *6* (11), 695–704.

(5) Gaudreau, L.; Tielrooij, K. J.; Prawiroatmodjo, G. E. D. K.; Osmond, J.; Garcia de Abajo, F. J.; Koppens, F. H. L. *Nano Lett.* **2013**, *13*, 2030–2035.

(6) Liv, N.; Lazic, I.; Kruit, P.; Hoogenboom, J. P. *Ultramicroscopy* **2014**, *143*, 93–99.

(7) Thiberge, S.; Zik, O.; Moses, E. *Rev. Sci. Instrum.* **2004**, *75* (7), 2280–2289.

(8) Nishiyama, H.; Suga, M.; Ogura, T.; Maruyama, Y.; Koizumi, M.; Mio, K.; Kitamura, S.; Sato, C. *J. Struct. Biol.* **2010**, *169*, 438–449.

# Chapter 3

## Facet-Dependent Photoreduction on Single ZnO Crystals

Elke Debroye,* **Jordi Van Loon**,* Haifeng Yuan, Kris P.F. Janssen, Zaizhu Lou, Sooyeon Kim, Tetsuro Majima, Maarten B.J. Roeffaers

Adapted with permission from: *J. Phys. Chem. Lett.* **2017**, 8, 340−346

* Joint first authors

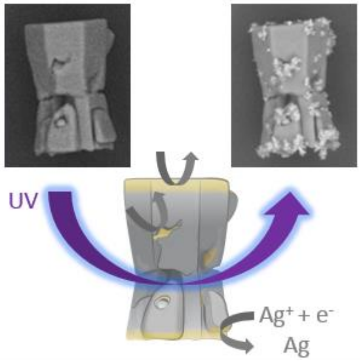

Photocatalytic reactions occur at the crystal-solution interface, hence, specific crystal facet expression and surface defects can play an important role. Here, we investigate the structure related photoreduction at zinc oxide (ZnO) microparticles, via integrated light and electron microscopy in combination with silver metal photodeposition. This enables a direct visualization of the photoreduction activity at specific crystallographic features. It is found that silver nanoparticle photodeposition on dumbbell-shaped crystals mainly takes place at the edges of O-terminated $(000\bar{1})$ polar facets. In contrast, on ZnO microrods photodeposition is more homogeneously distributed with an increased activity at $\{10\bar{1}\bar{1}\}$ facets. Additional time-resolved measurements reveal a direct spatial link between the enhanced photoactivity and increased charge carrier lifetimes. These findings contradict earlier findings based on indirect, bulk scale experiments, assigning the highest photocatalytic activity to polar facets. The presented research demonstrates the need for advanced microscopy techniques to directly probe the location of photocatalytic activity.

## Disclaimer

http://pubs.acs.org/doi/abs/10.1021/acs.jpclett.6b02577

## Contributions

E.D. and J.V.L. have contributed equally to this work. M.B.J.R., T.M., and E.D. conceived the experiments. E.D. and J.V.L. performed the photodeposition experiments. J.V.L. and K.P.F.J. are in charge of building and maintaining the ILEM setup. E.D., Z.L., and S.K. performed the time-resolved PL measurements and H.Y. assisted with the analysis and interpretation of the measurements. E.D., J.V.L., and M.B.J.R. prepared the manuscript with contributions from all coauthors.

# Chapter 3 - Facet-Dependent Photoreduction on Single ZnO Crystals

## 3.1. Introduction

Zinc oxide (ZnO) photocatalysts have shown great potential for applications in environmental remediation as they can for example be used in wastewater treatment, converting contaminants into harmless substances.[1,2] It is generally accepted that structural and morphological features influence the performance of semiconductor photocatalytic nanomaterials, including ZnO.[3–6] Literature reports synthesis procedures of a wide range of ZnO crystals with different morphologies and sizes, enabling an indirect investigation of structure-dependent photocatalytic activity by specifically expressing certain crystallographic facets.[7–12] Particularly for rod-like ZnO crystals, a lot of effort has been put in changing the ratio of oxygen- $(000\bar{1})$ or zinc- $(0001)$ terminated polar facets to non-polar crystal facets. The different crystallographic facets with the corresponding indices are shown for a representative dumbbell-shaped particle in **Figure 3.1a**. In general, it has been found that a higher ratio of polar to non-polar crystal facets greatly enhances the overall performance of the ZnO photocatalyst.[13–18] Typically, a relative and absolute quantification of polar versus non-polar crystal facets obtained by electron microscopy is linked to the overall photocatalytic performance determined by monitoring the bulk photodegradation of colored or fluorescent compounds.[10,14–17] Clearly, the knowledge on the facet-dependent photocatalytic performance of ZnO is mostly based on indirect evidence obtained from ensemble-averaged experiments. However, the observed photocatalytic performance does not only depend on the facet abundance, also the crystal size and the nature and density of crystal defects is of importance. All of these factors are highly intertwined and are readily altered by slight changes to the synthesis conditions. An approach that enables direct visualization of the structure-activity relationship is thus highly needed.

## 3.2. Experimental section

### 3.2.1. Materials and reagents

Zinc acetate dihydrate ($ZnO(CH_3COO)_2 \cdot 2H_2O$, ≥98.0%, Sigma-Aldrich), zinc nitrate hexahydrate ($ZnO(NO_3)_2 \cdot 6H_2O$, Reagent Grade, 98%, Sigma-Aldrich), sodium hydroxide (NaOH, >99%, VWR Chemicals), potassium hydroxide (KOH, >99%, Sigma-Aldrich), silver nitrate ($AgNO_3$, ≥99.0%, Sigma-Aldrich) and acetic acid ($CH_3COOH$, ≥99.0%, Sigma-Aldrich) were used as received without further purification. In all experimental procedures, milli Q water (Millipore) has been employed. Hydrothermal reactions were conducted in stainless steel Teflon-lined autoclaves in a Thermo Scientific Heratherm oven

(OGS60). Suspensions were dispersed in a 60 W Branson 2200 Ultrasonic bath equipped with thermostatic heating.

### 3.2.2. Synthesis ZnO dumbbells[19]

4.4 g of $ZnO(CH_3COO)_2 \cdot 2H_2O$ was dissolved in 20 mL of milli Q water under vigorous stirring. The pH of the clear zinc acetate solution was adjusted to pH 8 with a 4 M aqueous NaOH solution. The resulting reaction mixture was then transferred to a 30 mL stainless steel Teflon-lined autoclave and heated to 155 °C where the mixture was kept for 48 hours. After cooling down to room temperature, the solid product was filtered from the reaction liquid. The resulting crystals were thoroughly washed with milli Q water and dried overnight in an oven at 80 °C prior to use.

### 3.2.3. Synthesis ZnO microrods[20]

14.868 g of $ZnO(NO_3)_2 \cdot 6H_2O$ was dissolved in 50 mL of milli Q water at room temperature, resulting in a 0.5 M zinc nitrate aqueous solution. The pH of the solution was increased to pH 12 by adding dropwise a 1.5 M aqueous KOH solution, followed by vigorous stirring for 10 min. The white slurry mixture was transferred into a 30 mL stainless steel Teflon-lined autoclave and the hydrothermal reaction was conducted at 180 °C in an oven for 20 hours. After the reaction was completed, the suspension was cooled down and the final product was collected by pressure filtration. The white powder was thoroughly washed with milli Q water and dried overnight in an oven at 120 °C for 12 hours.

### 3.2.4. Glass cleaning and sample preparation for ILEM experiments

The glass coverslips were cleaned with milli Q ultrapure water followed by thermal treatment at 460 °C overnight. In order to spread the ZnO crystals uniformly over the glass surface, the coverslip was placed in an UV-ozone photo reactor (PR-100) for several minutes to make the surface more hydrophilic. A suspension of 1 mg/mL of the ZnO crystals in ultrapure water was shaken thoroughly and dispersed in an ultrasonic water bath for 1 minute. Then, 15 µL of this suspension was dropcasted on top of the glass coverslip, resulting in a thin and uniform layer of ZnO crystals after drying in the dark.

### 3.2.5. Photodeposition of silver nanoparticles on the ZnO crystal surface

After obtaining initial SEM micrographs on the ZnO crystal of interest, the sample chamber was vented to atmospheric pressure and a droplet of 1 mM aqueous silver nitrate was added on the top of the envisioned ZnO crystal on the glass coverslip. The ZnO photocatalyst was subsequently illuminated for 20 seconds with 365 nm UV light from an LED source outside the vacuum chamber coupled in via an optically transparent window in the chamber door.

Afterwards, the liquid was carefully removed before pumping down the EM chamber and recording new SEM images.

### 3.2.6. Glass cleaning and sample preparation for single-particle photoluminescence experiments

The glass coverslips were purchased from Matsunami Glass and cleaned by sonication in a 20% detergent solution (As One, Cleanace) for 6 hours, followed by five times sonication in warm water for 30 minutes. Finally, the coverslips were rinsed with milli Q ultrapure water (Millipore). 15 µL of the well-dispersed 1 mg/2 mL aqueous suspensions of the ZnO crystals were drop-casted on the cleaned coverslip. The coverslip was dried in the dark to immobilize the particles on the surface.

### 3.2.7. Single-particle photoluminescence measurements by confocal microscopy

Single-particle photoluminescence images and decay profiles of the ZnO samples were recorded using an objective-scanning confocal microscope system (PicoQuant, MicroTime 200) coupled with an Olympus IX71 inverted fluorescence microscope. The samples were excited through an oil-immersion objective lens (Olympus, UPlanSApo, 1.40 NA, 100x) using a circular-polarized 405 nm pulsed laser (0.45 µW, PicoQuant, FWHM = 54 ps, 20 MHz) controlled by a PDL-800B driver (PicoQuant). The emission from the sample was collected by the same objective and detected by a single-photon avalanche photodiode (Micro Photon Devices, PDM 50CT) through a dichroic beam splitter (Chroma, 405rdc), long pass filter (Chroma, HQ430CP) and a 75 µm pinhole for spatial filtering to reject out-of-focus signals. All the experimental data were obtained at room temperature.

### 3.2.8. Photoluminescence decay profile analysis

Since the decay profiles correspond to a biexponential decay, the amplitude weighted average lifetime ($\tau_{amp}$) is determined as a means of the average charge carrier lifetime along the length of the crystals. The analysis is performed using SymPhoTime (PicoQuant, Germany) and is based on the following formula:

$$\tau_{amp} = \{(A_1.\ \tau_1) + (A_2.\ \tau_2)\} / (A_1 + A_2)$$

$\tau$ corresponds to the decay components and A to the respective amplitudes.

## 3.3. Results and discussion

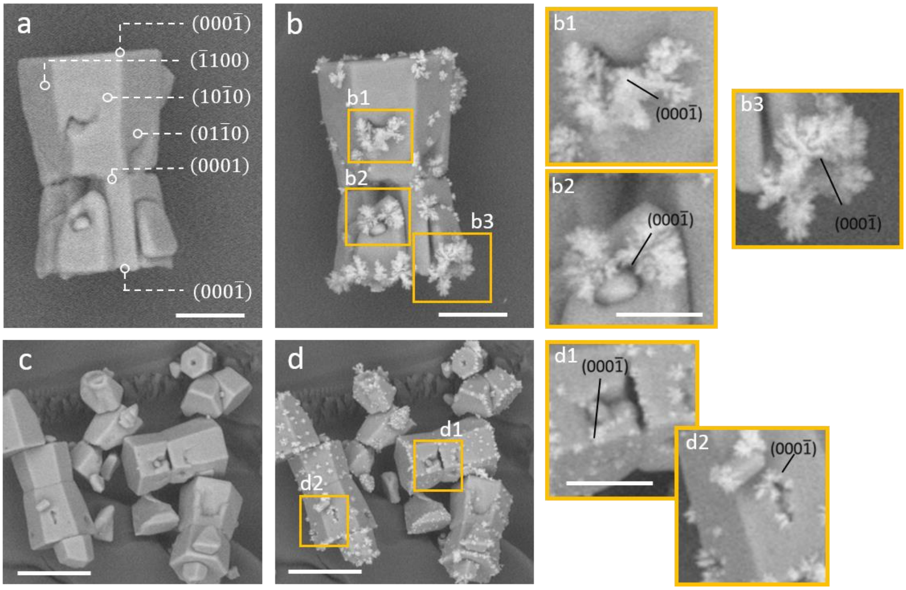

***Figure 3.1.*** *(a, c) SEM images of dumbbell-shaped ZnO crystals obtained before and (b, d) after UV photodeposition of silver nanostructures (20 seconds of illumination). The principle facets of hexagonally shaped ZnO crystals are indicated with their Miller-Bravais notation in (a).*[13] *As the non-polar side facets of hexagonal ZnO crystals belong to the same equivalent family of lattice planes, they can also be denoted as* $\{10\bar{1}0\}$*.The images are obtained with a back scattered electron detector (BSED). The insets offer a more detailed view on the exact location of the silver photodeposition. Scale bars: 2 µm (a, b), 1 µm (b2), 5 µm (c, d) and 2 µm (d1).*

The accessibility of photogenerated charge carriers at the photocatalyst surface can be directly observed by means of the photoreduction of silver ions to silver nanoparticles.[21] The UV photodeposition of silver on ZnO crystals is often used to improve the photocatalytic performance as the silver acts as an efficient trap for the photogenerated electrons, reducing the probability of electron-hole pair recombination.[22–25] However, so far the facet-dependent photodeposition of silver nanoparticles has not been studied in great detail.[26–28] In this work, the photo-induced silver deposition is explored at the single-particle level for two commonly encountered ZnO structures with different crystallographic facets using an integrated light and electron microscope (ILEM).[29,30] For this purpose, an optical microscope was integrated into a FEI Quanta 250 FEG environmental scanning electron microscope (SEM) using the SECOM platform of Delmic (**Scheme S3.1**).[31,32] This ILEM configuration allows the nanoscale observation of ZnO crystals by SEM, before and after UV-induced silver co-catalyst deposition.[30] As such, silver metal deposition acts as a probe reaction to monitor the influence of catalyst structural features on the photo-induced activity.[23,33–35]The combination of SEM with optical microscopy was indispensable in this study, as the required resolution for a proper structural investigation could not be obtained with the optical microscope used to provide the UV irradiation. On the other hand, a correlative approach, in which structural SEM imaging and UV-mediated silver photodeposition is achieved by means of two dedicated setups, is in principle possible. However, this requires the sample to be repeatedly transferred between setups, which is time consuming and increases the risk of sample contamination and losing the regions of interest (ROI).

Hexagonally shaped ZnO crystals (4 µm in diameter x 7 µm in length) were prepared according to the synthesis procedure reported by Wen et al.[19] Representative SEM images of the dumbbell-like ZnO microcrystals prepared via this method are presented in **Figure 3.1**. The electron micrographs in **Figure 3.1a and c** were obtained after the sample was drop casted onto a cover slide for optical microscopy and prior to the UV photodeposition of silver nanoparticles from an aqueous silver nitrate solution. The crystallographic facets and the presence of structural imperfections on the bare ZnO can be readily observed from these micrographs. Note that the $(0001)$ and $(000\bar{1})$ facets in these dumbbells were identified through an additional experiment, by selectively dissolving the $(000\bar{1})$ facet in acetic acid (**Figure S3.2**).[36] **Figure 3.1b and d** show the corresponding electron micrographs obtained after UV photodeposition of silver nanoparticles. The photodeposition procedure consisted of venting the sample chamber to atmospheric pressure, adding a 1 mM aqueous silver nitrate solution to the ZnO particles deposited on the glass slide, followed by a 20 second illumination from the bottom side with 365 nm UV light. Afterwards, the liquid was carefully removed using tissue paper before pumping down the EM chamber and recording the SEM images of the same photocatalyst particles. Since the surface of the pristine ZnO crystals can be studied from the scanning electron micrograph acquired before silver photodeposition, the actual locations of the photodeposited silver nanoparticles can be related to specific crystal facets and/or structural imperfections at the ZnO surface, prior to being covered by silver.

Zooming in on **Figure 3.1b**, the deposited silver nanoparticles are readily visible in the back scattered electron (BSE) micrographs as bright features at the ZnO surface. Clearly, structural imperfections and the crystal edges between the $(000\bar{1})$ and the lateral $\{10\bar{1}0\}$ facets display a strongly increased tendency to photoreduce silver ions compared to the main $(000\bar{1})$ and $\{10\bar{1}0\}$ facets themselves. The effect of these structural imperfections is highlighted in the insets that show enlarged images of selected ROI. Similar observations can be made for the ensemble of ZnO crystals shown in **Figure 3.1c**. However, after silver deposition (**Figure 3.1d**), it is revealed that structural imperfections are not homogeneously active. The photodeposition seems to primarily take place at the edges assigned to local O-terminated $(000\bar{1})$ crystal facets. Nonetheless, some so-called non-polar planes of the crystals in **Figure 3.1d** show silver deposition that cannot be directly correlated to any structural defect; this photodeposition might be attributed to crystal imperfections that remain unresolved in the recorded electron micrographs. Furthermore, even within individual particles not all structural defects show equal photoreduction activity.

In order to minimize the risk for electron beam induced structural damage, the beam currents were kept as low as possible. This was also necessary to keep sample charging to a minimum as imaging was performed on non-conducting cover glasses. Still, electrons could remain accumulated on the ZnO particles. Before performing the photocatalytic experiments, the sample chamber was vented, bringing in gas molecules that are known to efficiently neutralize surface charge. As such, the influence of the mild SEM conditions is assumed to have a negligible influence on the outcome of this work.

Another point of attention was the used imaging geometry (**Scheme S3.1**) with SEM structural imaging from the top of the ZnO crystal and UV illumination via the optical microscope from the bottom side. Hence, exciton formation preferentially takes place in the bottom 100 nm inside the ZnO crystals. These excitons diffuse through the bulk of the particle towards the crystal surface where reactions can take place. The charge carrier diffusion inside these ZnO crystals (vide infra) exceeds the typical particle thickness used in this study. This reasoning is also supported by our experimental observations. Besides clear photoreduction activity at the top crystal facets, the edge of the $(000\bar{1})$ in the slightly tilted crystal shown in **Figure 3.1d** does not show a gradient in activity from the bottom to the top.

The structure-activity relationship was quantified in more detail by inspecting 25 individual dumbbell-shaped ZnO crystals from the same batch, before and after UV-induced silver photodeposition. (Five are displayed in **Figure 3.1**, the others can be consulted in **Figure S3.3**.) The correlation of silver photodepositions to specific structural features of the ZnO photocatalyst reveals that about 50% of the silver nanoparticles are deposited at the outlines of structural imperfections at the non-polar facets, 45% at the edges of the O-terminated polar facets and the remaining 5% are distributed randomly at what appear to be defect-free locations. The latter is concluded based on the available structural resolution offered by the recorded scanning electron micrographs. This observation is remarkable since literature mostly suggests that the polar $(0001)$ or $(000\bar{1})$ crystal facets are the most photocatalytically active.[10,14–17]

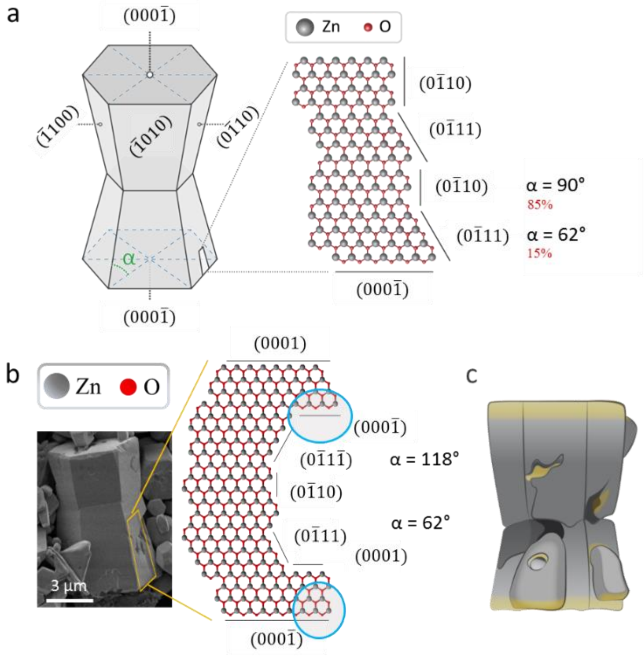

***Figure 3.2.*** *(a) The Miller-Bravais indices of the principle facets of the schematic hexagonally shaped ZnO crystal are shown.*[13] *The enlarged view gives a detailed picture of the pyramidal facets in dumbbell-shaped crystals consisting of alternating semi-polar* $\{10\bar{1}1\}$ *and non-polar* $\{1\bar{1}00\}$ *crystal facets. Their relative contribution was calculated based on the distribution of the pyramidal α-value measured for 30 dumbbell-shaped ZnO crystals (**Figure S3.3**). (b) Besides semi-polar* $\{10\bar{1}1\}$ *and non-polar* $\{1\bar{1}00\}$ *crystal facets, pits and grooves feature polar Zn- and O-terminated facets. The blue circles highlight the most active silver photodeposition sites as found in this study. Scale bar: 2 µm. (c) The yellow shade highlights the zones with elevated photoreduction activity at the outline of the O-terminated* $(000\bar{1})$ *facets at the crystal extremes as well as in the structural imperfections.*

To further rationalize this observation, we turned to literature where the structural characteristics of ZnO crystals have been described in detail.[36-38] Instead of the simplified representation of hexagonally shaped ZnO crystals that is often used in photocatalytic studies (**Figure 3.2a**), extensive investigations have been performed to determine the intrinsic crystal facets of pyramidal shaped ZnO crystals. High-angle annular dark-field scanning transmission electron microscopy (HAADF-STEM) revealed that the $\{0001\}$ basal planes are almost atomically flat containing a very small amount of defects, while the pyramidal planes consist of alternating $\{10\bar{1}0\}$ and $\{10\bar{1}1\}$ crystal facets (**Figure 3.2a**); the semi-polar $\{10\bar{1}1\}$ facets are oxygen terminated.[37,38] From the average angle of 85 ° between the pyramidal facets and the polar (0001) planes (**Figure S3.3**) it is estimated that around 15% of the total area of the pyramidal plane displays a semi-polar $\{10\bar{1}1\}$ character, since pure $\{10\bar{1}1\}$ facets should make a 62 ° angle while perfect $\{10\bar{1}0\}$ facets should be at exactly 90 °. Furthermore, scanning tunneling microscopy has revealed an additional roughness at the pyramidal ZnO planes due to the presence of horizontally oriented grooves.[39] Besides the semi-polar and non-polar facets, these surface imperfections feature additional polar Zn- and O-terminated facets. **Figure 3.2b** displays a schematic representation of these different crystal facets at a structural imperfection on the pyramidal plane. The enhanced photoactivity of semi-polar $\{10\bar{1}1\}$ pyramidal crystal facets has previously been proposed by Chang et al. based on the bulk performance of different ZnO crystal morphologies.[13] Hydroxylation of the under-coordinated oxygen facets would enhance electron diffusion toward these facets.[36,40,41]

Differences in charge carrier mobility were assessed via spatially- and temporally-resolved photoluminescence (PL) measurements on individual ZnO crystals. It has previously been reported that exciton lifetimes in ZnO vary with crystal morphology.[42,43] Moreover, the results presented here clearly show spatial variations in charge carrier lifetimes within individual ZnO crystals. **Figure 3.3a** shows that the PL decay strongly depends on the position along the c-axis of the dumbbell-shaped crystal with the longest lifetimes recorded near the oxygen terminated $(000\bar{1})$ facet. As such, this effect seems to be directly correlated to the crystal length, as confirmed by plotting the relative increase in PL decay times near the O-terminated $(000\bar{1})$ plane versus the Zn-terminated $(0001)$ plane in function of the distance between the O- and Zn-terminated polar planes (**Figure 3.3c**). The longer charge carrier lifetimes detected at the crystallographic edges of the O-terminated $(000\bar{1})$ crystal faces and at the outlines of structural defects correspond to longer free carrier diffusion lengths (DL) according to DL ≈ $(D\,\tau)^{1/2}$, in which τ represents the typical photoluminescence lifetime of a few nanoseconds for ZnO and D represents the diffusion coefficient. The charge carrier diffusion length in ZnO can be estimated to be a few micrometers; the effective diffusion coefficient for ZnO rods is 0.5 $cm^2\ s^{-1}$, as obtained from literature.[43] This additionally confirms the validity of our earlier assumptions that electrons formed near the bottom surface of the ZnO crystals can indeed diffuse through the bulk of the particles to reach the top surface and result in silver nanoparticle photodeposition.

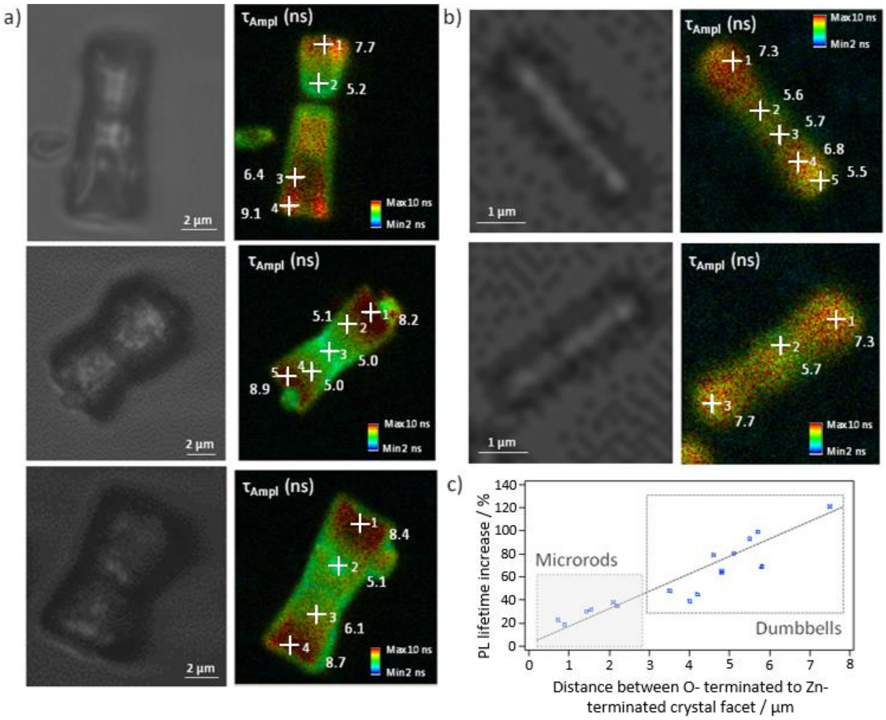

***Figure 3.3.*** *Spatially and temporally resolved PL measurements on individual ZnO crystals after excitation with a ps-pulsed 405 nm laser using a confocal microscope. Distribution map of free charge carrier lifetimes for (a) three dumbbell-shaped ZnO crystals and (b) two ZnO microrods. (c) Correlation of the relative increase in PL decay times near the O-terminated polar plane versus the Zn-terminated* $(0001)$ *plane in function of the distance between both crystallographic facets.*

Note that the due to practical limitations, photoluminescence lifetime experiments were determined using 405 nm laser excitation and visible photoluminescence (430 - 850 nm) detection. Hence, these results are related to crystal imperfections rather than exciton emission. The significant correlation between the structural defect photoluminescence lifetime and the zones with enhanced silver photodeposition are undeniable. **Figure S3.6** shows the related emission spectra recorded at the different positions along the ZnO crystals. The positions with enhanced lifetime are related to red-shifted emission which is typically assigned to zones with enhanced concentrations of crystallographic imperfections.[b] As the role of defects on exciton lifetime and photocatalytic performance has already been actively discussed in literature, this observation can further be investigated by UV excitation. The blue circles in **Figure 3.2b** highlight the most active silver photodeposition sites at the edges of O-terminated polar faces occurring at the top and bottom planes of the crystal, as well as in structural imperfections.

Interestingly, rod-like ZnO crystals are sometimes encountered in a batch of dumbbell-shaped crystals (see right side of **Figure S3.4a and b**). These particles display a markedly different photoreduction performance compared to the dumbbell-shaped ZnO crystals, as a more homogeneous silver nanoparticle photodeposition (inset **Figure S3.4a.1**) is observed on the seemingly defect-free crystal side faces (inset **Figure S3.4b.1**). In order to further investigate the activity of such ZnO microrods with respect to photo-induced silver deposition, a batch of ZnO microrods was synthesized as described by Razavi et al.[20] In **Figure 3.4**, electron micrographs of microrods before and after silver nanoparticle photodeposition are shown; the experimental procedure was identical to that for the dumbbell-shaped particles described before. Clearly, at the current resolution of the scanning electron micrographs, structural imperfections are less commonly encountered compared to the dumbbell-shaped sample. However, the observation that silver photodeposition occurs more homogeneously at crystal edges and $\{10\bar{1}0\}$ facets of the rod-like ZnO crystals is confirmed in this batch (**Figure 3.4b and c**). Importantly, an additional crystal facet seems to have developed in these crystals. At the boundary between the $(000\bar{1})$ and the $\{10\bar{1}0\}$ side facet, $\{10\bar{1}\bar{1}\}$ facets can be recognized. This semi-polar $\{10\bar{1}\bar{1}\}$ Zn-terminated facet has previously been observed as a step-wise transition of the polar $(000\bar{1})$ O-terminated face into the pyramidal $\{10\bar{1}0\}$ facets in a stack of ZnO nano-pyramids.[37] Ensemble photocatalytic activity measurements of these complex nano-pyramids indicated that these facets lead to an increased photocatalytic activity. Our photodeposition measurements support this hypothesis, as the largest silver nanoparticle deposits are observed at these facets. Similar to the ZnO dumbbells, time-resolved PL studies on individual ZnO microrods (**Figure 3.3b**) demonstrate increased free charge carrier lifetimes near the O-terminated polar facets, indicating an enhanced charge carrier diffusion towards these crystal facets.

---

[b] A variety of different visible PL emission colors have been reported for ZnO materials. This PL is generally attributed to different types of defects, e.g. Zn and oxygen vacancies, Zn and oxygen interstitials, etc.[44] Green PL, emission centered around 520 nm, is often associated to singly ionized oxygen vacancies,[44] whereas red emission seems to be linked to oxygen interstitials and/or Zn vacancies.[45] Therefore, more detailed studies on the link between the recorded PL spectra, the associated structural defects and the local photocatalytic performance needs to be investigated in future research.

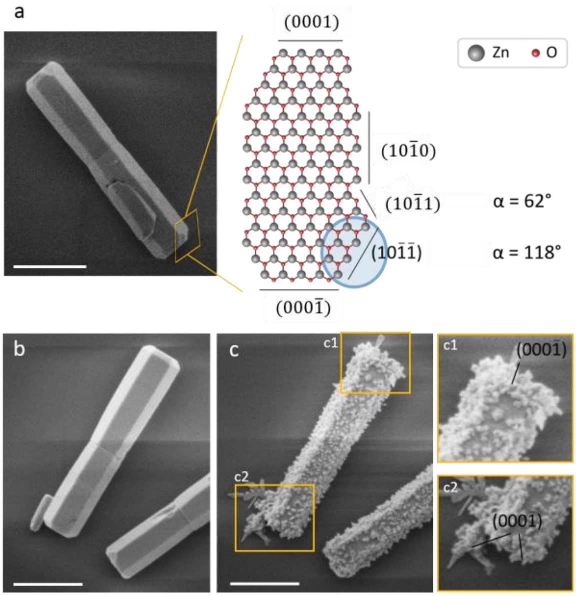

***Figure 3.4.*** *(a) SEM image of a ZnO microrod and schematic representation displaying the crystallographic Zn-terminated* $\{10\bar{1}\bar{1}\}$ *semi-polar facets adjacent to the O-terminated polar face. (b) SEM image of a ZnO microrod obtained before and (c) after 20 seconds of UV-induced photodeposition of silver nanostructures. The insets c.1 and c.2 reveal that the boundary areas of the polar* $(000\bar{1})$ *crystal faces towards the* $\{10\bar{1}\bar{1}\}$ *facets display an increased photo-induced silver deposition. Scale bars: 1 µm.*

In their pioneering work, Pacholski et al.[26] demonstrated that the photodeposition of silver on very small ZnO nanocrystals occurred at one particular tip, which was assigned to be the O-terminated polar face. Looking closely at these electron micrographs and keeping in mind the observations made in this study, the silver nanoparticles do not seem to be located at the O-terminated polar tip itself, but at what appears to be the $\{10\bar{1}\bar{1}\}$ facet.

In order to correctly relate silver nanoparticle photodeposition to facet-dependent electron accessibility, any contribution of preferential silver cation chemisorption at these facets should be ruled out, as this would locally enhance photodeposition. To minimize the effect of preferential electrostatic attraction of silver cations, the described experiments were performed at pH 10 as the bulk isoelectric point of ZnO was determined to be at pH 8.7-10.3.[36] Protonation of the O-terminated polar face was reported to induce a downward band bending, decreasing the recombination probability of the photogenerated charges and inducing a directional electron diffusion towards this polar facet.[36,41] This model has been confirmed by our experimental results as they reveal longer charge carrier lifetimes at the outlines of O-terminated $(000\bar{1})$ facets and structural imperfections as discussed previously (**Figure 3.3**).

This study further proves that the photocatalytic activity of ZnO particles is the result of several factors. Via the applied ILEM approach, crystal facets and surface imperfections can straightforwardly be related to the photocatalytic activity. As such, differences in silver deposition between the ZnO dumbbells and microrods reveal that edge of the O-terminated $(000\bar{1})$ facet shows an enhanced photocatalytic activity. In contrast to the dumbbell-shaped crystals where this edge is very sharp, the activity can directly be linked to a clearly developed $(10\bar{1}\bar{1})$ facet in the microrod sample. Further, the activity of the $\{10\bar{1}0\}$ side facets in the dumbbell-shaped crystals can straightforwardly be associated to structural imperfections and more specifically to the $(000\bar{1})$ facet at these sites. In the microrods, no surface imperfections could be resolved in the obtained scanning electron micrographs, so this link cannot be directly made. However, we assume that crystallographic imperfections and the related crystal facets are at the origin of the observed photocatalytic deposition. Note that at the bulk scale both ZnO samples showed a similar activity in the photoreduction of resazurin to the fluorescent resorufin. This further supports the idea that many important aspects that determine the overall photocatalytic experiments are masked in a typical bulk activity measurement and that rational optimization relies on the in depth insights that can be generated via microscopic observations.

## 3.4. Conclusion

By using UV photoreduction of silver ions as probe reaction, correlative light and electron microscopy experiments have revealed a notable intraparticle heterogeneity in photoreduction activity for ZnO crystals. On dumbbell-shaped ZnO crystals, about half of the silver photodeposition occurs at the crystallographic edges of the O-terminated $(000\bar{1})$ polar planes, whereas the other half is observed at the O-terminated facets of structural imperfections. Identical experiments performed on seemingly defect-free ZnO microrods confirmed that the edges of O-terminated polar facets, outlined with $\{10\bar{1}\bar{1}\}$ facets, display the highest photodeposition activity. Until now, the most active crystal facets have been determined by monitoring the bulk scale photodecomposition efficiency of ZnO crystals with different sizes and morphologies.[10,14–17] However, such a bulk-scale approach does not provide a direct structure-activity link, since only idealized crystals consisting of defect-free crystal facets are considered. This work reveals that the influence of structural imperfections on the photocatalytic performance should not be neglected. The presented approach, i.e. detailed structural characterization of individual photocatalysts using SEM, both before and after performing photodeposition, is crucial to correctly rationalize the activity pattern. Besides photoreduction, a lead- or manganese-based approach could be applied to reveal locations with enhanced photo-oxidation activity. Alternatively, fluorogenic reactions could enable an investigation of the structure-activity relationship at the nanoscale. In general, spatially- and temporally-resolved studies will greatly contribute to a better understanding, further optimization and even rationalization of catalyst design. Furthermore, the observed intraparticle distribution of charge carrier PL decays is also of interest in the field of composite mesocrystals. Exact knowledge of the surface and internal structures is necessary to achieve efficient charge transfer processes, which are important for catalysis, optoelectronics, sensing and energy conversion.[46]

## 3.5. References

(1) Chatterjee, D.; Dasgupta, S. *J. Photochem. Photobiol. C Photochem. Rev.* **2005**, *6* (2–3), 186–205.
(2) Mills, A.; Le Hunte, S. *J. Photochem. Photobiol. A Chem.* **1997**, *108* (1), 1–35.
(3) Chen, P.; Zhou, X.; Shen, H.; Andoy, N. M.; Choudhary, E.; Han, K.-S.; Liu, G.; Meng, W. *Chem. Soc. Rev.* **2010**, *39* (12), 4560–4570.
(4) Sambur, J. B.; Chen, P. *Annu. Rev. Phys. Chem.* **2014**, *65* (1), 395–422.
(5) Li, R.; Zhang, F.; Wang, D.; Yang, J.; Li, M.; Zhu, J.; Zhou, X.; Han, H.; Li, C. *Nat. Commun.* **2013**, *4*, 1432.
(6) Tachikawa, T.; Yamashita, S.; Majima, T. *J. Am. Chem. Soc.* **2011**, *133* (18), 7197–7204.
(7) Han, X. G.; He, H. Z.; Kuang, Q.; Zhou, X.; Zhang, X. H.; Xu, T.; Xie, Z. X.; Zheng, L. S. *J. Phys. Chem. C* **2009**, *113* (2), 584–589.
(8) Chang, J.; Ahmed, R.; Wang, H.; Liu, H.; Li, R.; Wang, P.; Waclawik, E. R. **2013**.
(9) Liu, T.-J.; Wang, Q.; Jiang, P. *RSC Adv.* **2013**, *3* (31), 12662–12670.
(10) Boppella, R.; Anjaneyulu, K.; Basak, P.; Manorama, S. V. *J. Phys. Chem. C* **2013**, *117* (9), 4597–4605.
(11) Gupta, J.; Bhargava, P.; Bahadur, D. *Phys. B Condens. Matter* **2014**, *448*, 16–19.
(12) Flores, N. M.; Pal, U.; Sandoval, A. *RSC Adv.* **2014**, *4* (77), 41099–41110.
(13) Chang, J.; Waclawik, E. R. *CrystEngComm* **2012**, *14* (11), 4041.
(14) Jang, E. S.; Won, J. H.; Hwang, S. J.; Choy, J. H. *Adv. Mater.* **2006**, *18* (24), 3309–3312.
(15) Zeng, J. H.; Jin, B. Bin; Wang, Y. F. *Chem. Phys. Lett.* **2009**, *472* (1–3), 90–95.
(16) Huang, M.; Yan, Y.; Feng, W.; Weng, S.; Zheng, Z.; Fu, X.; Liu, P. *Cryst. Growth Des.* **2014**, *14* (5), 2179–2186.
(17) Mclaren, A.; Valdes-Solis, T.; Li, G.; Tsang, S. C. *J. Am. Chem. Soc.* **2009**, *131* (35), 12540–12541.
(18) Jeon, E. H.; Yang, S.; Kim, Y.; Kim, N.; Shin, H.-J.; Baik, J.; Kim, H. S.; Lee, H. *Nanoscale Res. Lett.* **2015**, *10* (1), 361.
(19) Wen, F.; Li, W.; Moon, J. H.; Kim, J. H. *Solid State Commun.* **2005**, *135* (1–2), 34–37.
(20) Kiomarsipour, N.; Shoja Razavi, R. *Superlattices Microstruct.* **2012**, *52* (4), 704–710.
(21) Laurier, K. G. M.; Poets, M.; Vermoortele, F.; Cremer, G. De; Martens, J. A.; Uji-i, H.; De Vos, D. E.; Hofkens, J.; Roeffaers, M. B. J. *Chem. Commun.* **2012**, *48* (10), 1559–1561.
(22) Zhu, Y.; Liu, D.; Lai, Y.; Meng, M. *J. Nanoparticle Res.* **2014**, *16* (3).
(23) Chan, S. C.; Barteau, M. a. *Langmuir* **2005**, *21* (12), 5588–5595.
(24) Maicu, M.; Hidalgo, M. C.; Colón, G.; Navío, J. A. *J. Photochem. Photobiol. A Chem.* **2011**, *217* (2–3), 275–283.
(25) Dunn, S.; Sharp, S.; Burgess, S. *Nanotechnology* **2009**, *20* (11), 115604.
(26) Pacholski, C.; Kornowski, A.; Weller, H. *Angew. Chemie - Int. Ed.* **2004**, *43*

(36), 4774–4777.
(27) Bouzid, H.; Faisal, M.; Harraz, F. A.; Al-Sayari, S. A.; Ismail, A. A. *Catal. Today* **2015**, *252*, 20–26.
(28) Satheeshkumar, E.; Yang, J. *J. Raman Spectrosc.* **2014**, *45* (6), 407–413.
(29) Yuan, H.; Debroye, E.; Janssen, K.; Naiki, H.; Steuwe, C.; Lu, G.; Moris, M.; Orgiu, E.; Uji-I, H.; De Schryver, F.; Samorì, P.; Hofkens, J.; Roeffaers, M. *J. Phys. Chem. Lett.* **2016**, *7* (3), 561–566.
(30) Debroye, E.; Van Loon, J.; Gu, X.; Franklin, T.; Hofkens, J.; Janssen, K. P. F.; Roeffaers, M. B. J. *Part. Part. Syst. Charact.* **2016**, *33*, 412–418.
(31) Liv, N.; Zonnevylle, A. C.; Narvaez, A. C.; Effting, A. P. J.; Voorneveld, P. W.; Lucas, M. S.; Hardwick, J. C.; Wepf, R. A.; Kruit, P.; Hoogenboom, J. P. *PLoS One* **2013**, *8* (2), 1–9.
(32) Zonnevylle, A. C.; Van Tol, R. F. C.; Liv, N.; Narvaez, A. C.; Effting, A. P. J.; Kruit, P.; Hoogenboom, J. P. *J. Microsc.* **2013**, *252* (1), 58–70.
(33) Matsumoto, Y.; Ida, S.; Inoue, T. *J. Phys. Chem.* **2008**, *112*, 11614–11616.
(34) Morris Hotsenpiller, P. a.; Bolt, J. D.; Farneth, W. E.; Lowekamp, J. B.; Rohrer, G. S. *J. Phys. Chem. B* **1998**, *102* (17), 3216–3226.
(35) Giocondi, J. L.; Salvador, P. a.; Rohrer, G. S. *Top. Catal.* **2007**, *44* (4), 529–533.
(36) Valtiner, M.; Borodin, S.; Grundmeier, G. *Langmuir* **2008**, *24* (10), 5350–5358.
(37) Tang, D.; Allard, L. F.; Boley, A.; Smith, D. J.; Liu, J. *J. Mater. Sci.* **2013**, *48* (10), 3857–3862.
(38) Song, T.; Choung, J. W.; Park, J.-G.; Park, W. Il; Rogers, J. A.; Paik, U. *Adv. Mater.* **2008**, *20*, 4464–4469.
(39) Dulub, O.; Boatner, L. A.; Diebold, U. *Surf. Sci.* **2002**, *519* (3), 201–217.
(40) Wöll, C. *Prog. Surf. Sci.* **2007**, *82* (2–3), 55–120.
(41) Wang, J.; Wang, Z.; Huang, B.; Ma, Y.; Liu, Y.; Qin, X.; Zhang, X.; Dai, Y. ACS *Appl. Mater. Interfaces* **2012**, *4* (8), 4024–4030.
(42) Lin, C.-Y.; Lai, Y.-H.; Chen, H.-W.; Chen, J.-G.; Kung, C.-W.; Vittal, R.; Ho, K.-C. *Energy Environ. Sci*. **2011**, *4* (9), 3448.
(43) Chang, R.; Ithisuphalap, K.; Kretzschmar, I. AIMS *Mater. Sci*. **2016**, *3* (1), 51–65.
(44) Özgür, Ü.; Alivov, Y. I.; Liu, C.; Teke, A.; Reshchikov, M. A.; Özgür, Ü.; Alivov, Y. I.; Liu, C.; Teke, A.; Reshchikov, M. A.; Do, S.; Avrutin, V. *J. Appl. Phys.* **2005**, *98*, 1–95.
(45) Yang L.L., Zhao Q.X.,Willander M., Yang J.H., Ivanov I. *J Appl Phys.* **2009**;*105*,:053503–7.
(46) Bian, Z.; Tachikawa, T.; Zhang, P.; Fujitsuka, M.; Majima, T. *Nat. Commun.* **2014**, *5*, 3038.

## 3.6. Supporting information

X-ray diffractograms of the dumbbell and microrod ZnO samples

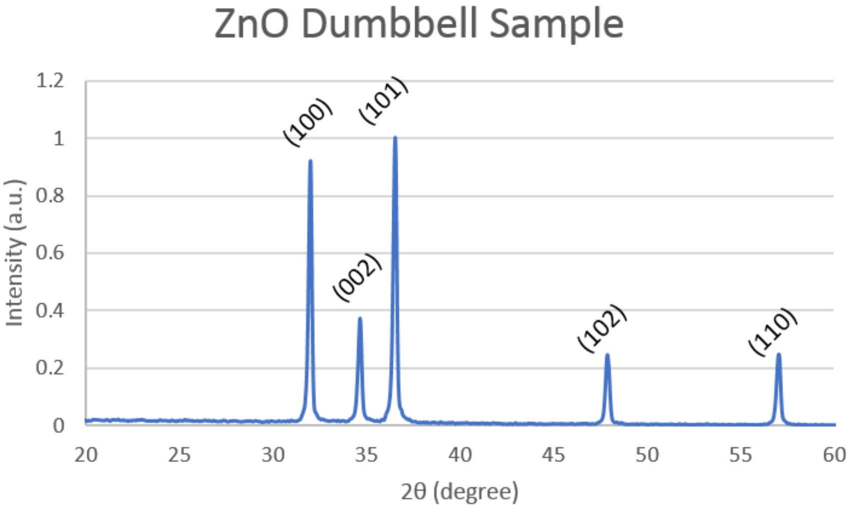

***Graph S3.1.*** *XRD spectrum of the synthesized dumbbell crystal sample.*

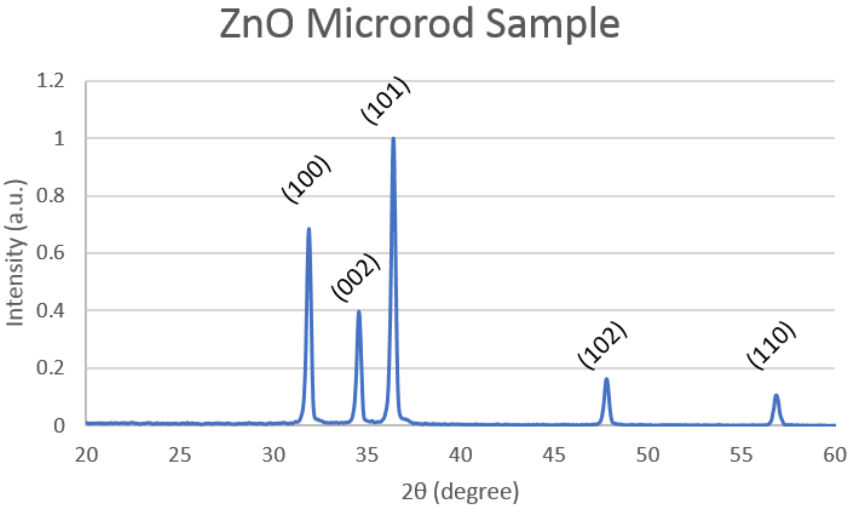

***Graph S3.2.*** *XRD spectrum of the synthesized microrod crystal sample.*

## ILEM specifications

Samples were analyzed by a FEI Quanta 250 FEG environmental scanning electron microscope with a customized chamber door (SECOM, Delmic BV). UV light generated by a Thorlabs LEDD1B, T-Cube LED Driver of 365 nm is directed into the SEM vacuum chamber by means of an optically transparent chamber window. A dichroic mirror and a 100x 1.4 NA CFI plan APO VC oil objective (Nikon) further direct the UV light onto the photocatalyst particles at the sample stage with an optical power density of 50.0 μW/cm$^2$. Such a configuration allows the study of silver photodeposition on ZnO photocatalysts using SEM in a correlated fashion. The possibility of conducting these experiments in one and the same setup implies that there is no need for shuttling the sample between dedicated setups which restricts sample contamination or alteration.

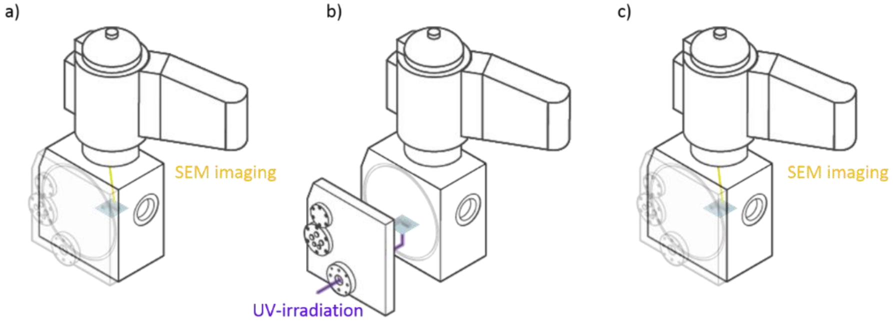

***Scheme S3.1.*** *The integrated light- and electron microscope (ILEM) is applied to perform SEM imaging on the sample (a) before and (c) after deposition. (b) The ILEM is equipped with a customized chamber door (Delmic BV) featuring an optically transparent window that allows 365 nm UV light from outside the door to reach the high NA objective lens on the inside, guiding the light onto the field of view that is being imaged by SEM, without the needs to transfer the sample between dedicated systems.*[30]

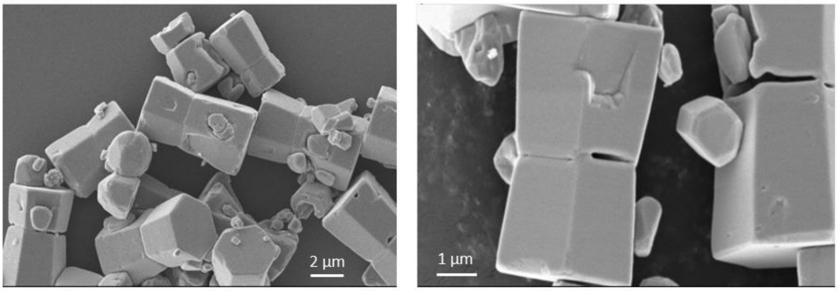

***Figure S3.1.*** *SEM images of typical dumbbell-shaped ZnO microcrystals as prepared.*

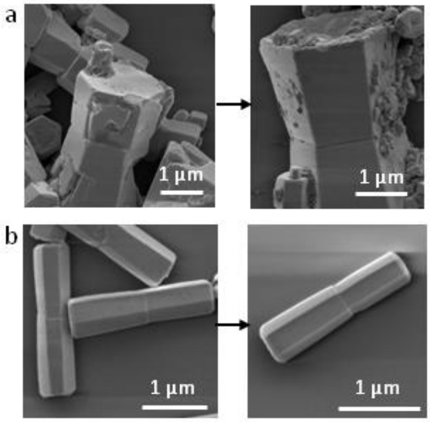

***Figure S3.2.*** *Acidic dissolution experiments. SEM images of (a) ZnO dumbbell crystals and (b) ZnO microrods before (left panel) and after (right panel) treatment with a 0.01 M aqueous solution of acetic acid, pH 4. The droplet of acetic acid was left for 5 minutes on the glass coverslip and then rinsed with milli Q ultrapure water, readily leading to the degeneration of the oxygen terminated* $(000\bar{1})$ *facet.*[36]

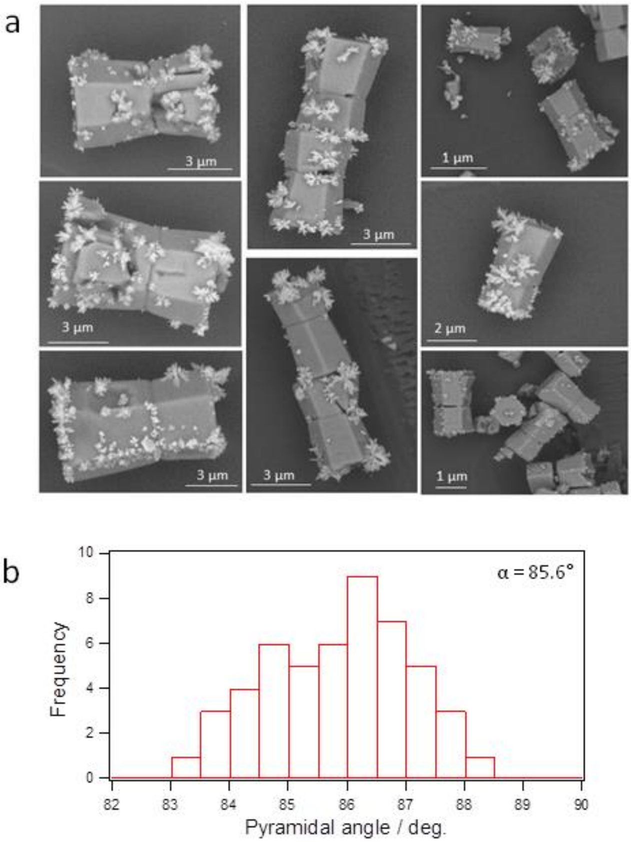

***Figure S3.3.*** *SEM images of ZnO dumbbell crystals after silver photodeposition during 20 seconds of illumination with UV light.*

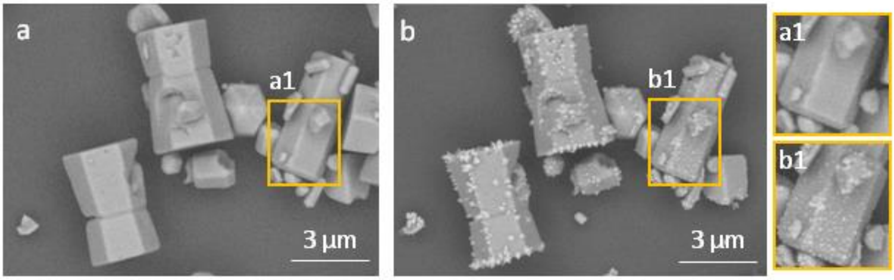

***Figure S3.4.*** *SEM images of ZnO microcrystals obtained before (a) and after (b) silver photodeposition during 20 seconds of illumination with UV light. A rod-like ZnO crystal is observed in this batch of dumbbell-shaped crystals (see right side of micrographs). On this ZnO microrod, a more homogeneous silver nanoparticle photodeposition (inset a.1) is observed on the seemingly defect free crystal side faces (inset b.1).*

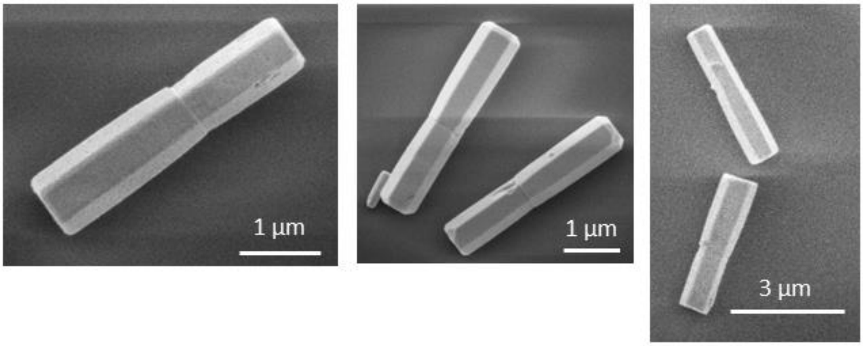

***Figure S3.5.*** *SEM images of typical rod-like ZnO crystals as prepared.*

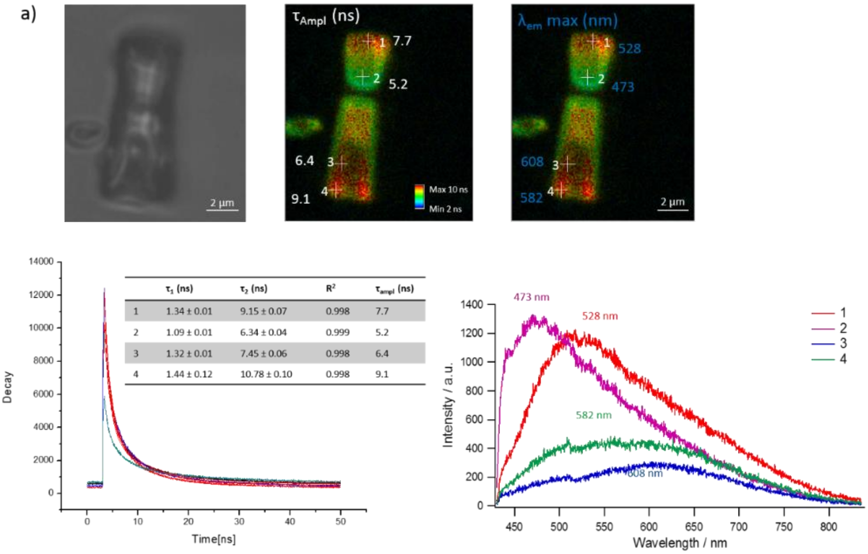

| | $\tau_1$ (ns) | $\tau_2$ (ns) | $R^2$ | $\tau_{ampl}$ (ns) |
|---|---|---|---|---|
| 1 | 1.34 ± 0.01 | 9.15 ± 0.07 | 0.998 | 7.7 |
| 2 | 1.09 ± 0.01 | 6.34 ± 0.04 | 0.999 | 5.2 |
| 3 | 1.32 ± 0.01 | 7.45 ± 0.06 | 0.998 | 6.4 |
| 4 | 1.44 ± 0.12 | 10.78 ± 0.10 | 0.998 | 9.1 |

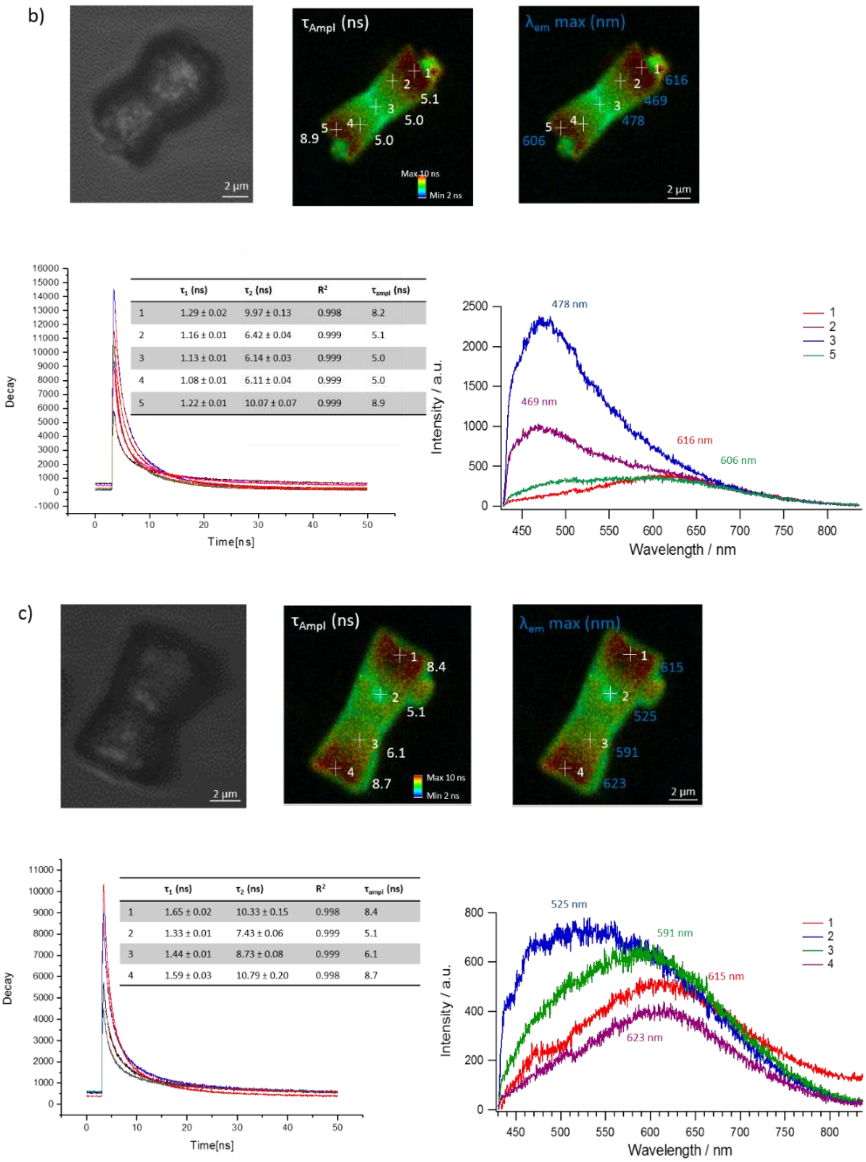

|  | $\tau_1$ (ns) | $\tau_2$ (ns) | $R^2$ | $\tau_{ampl}$ (ns) |
|---|---|---|---|---|
| 1 | 1.29 ± 0.02 | 9.97 ± 0.13 | 0.998 | 8.2 |
| 2 | 1.16 ± 0.01 | 6.42 ± 0.04 | 0.999 | 5.1 |
| 3 | 1.13 ± 0.01 | 6.14 ± 0.03 | 0.999 | 5.0 |
| 4 | 1.08 ± 0.01 | 6.11 ± 0.04 | 0.999 | 5.0 |
| 5 | 1.22 ± 0.01 | 10.07 ± 0.07 | 0.999 | 8.9 |

|  | $\tau_1$ (ns) | $\tau_2$ (ns) | $R^2$ | $\tau_{ampl}$ (ns) |
|---|---|---|---|---|
| 1 | 1.65 ± 0.02 | 10.33 ± 0.15 | 0.998 | 8.4 |
| 2 | 1.33 ± 0.01 | 7.43 ± 0.06 | 0.999 | 5.1 |
| 3 | 1.44 ± 0.01 | 8.73 ± 0.08 | 0.999 | 6.1 |
| 4 | 1.59 ± 0.03 | 10.79 ± 0.20 | 0.998 | 8.7 |

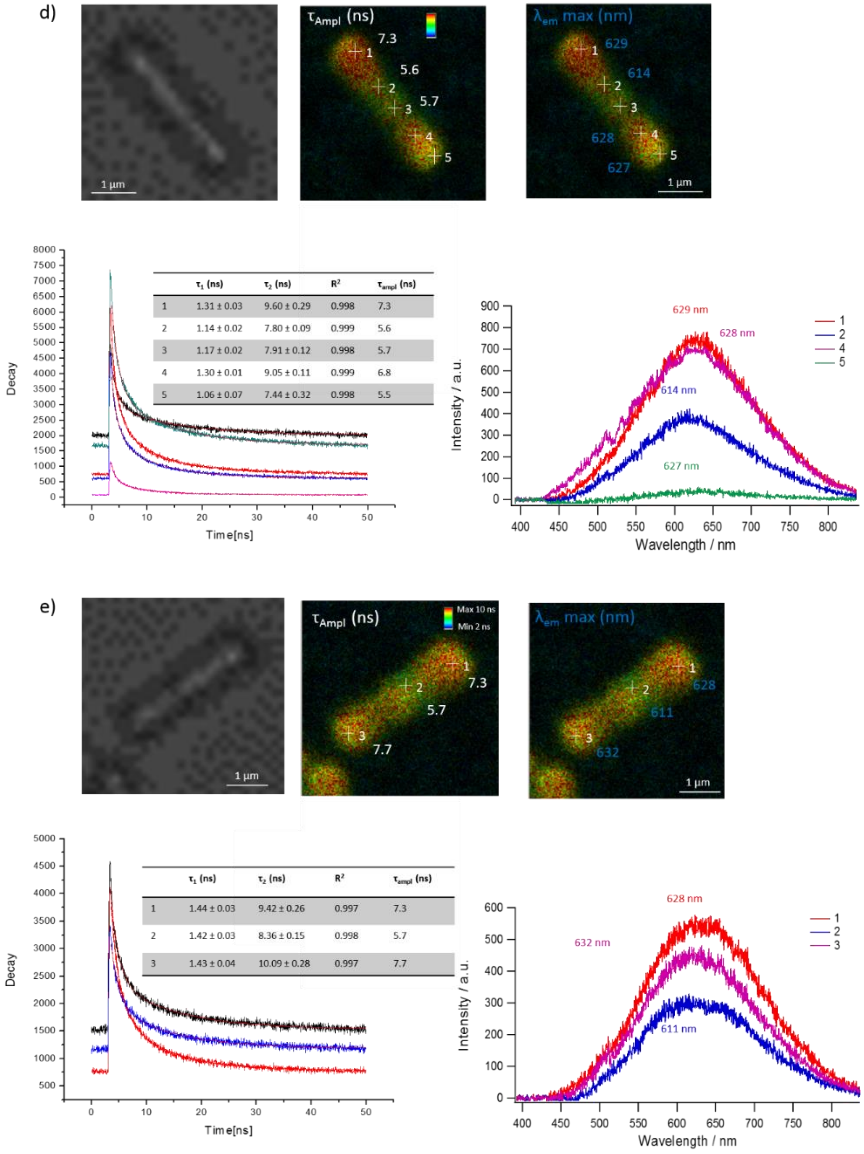

|  | $\tau_1$ (ns) | $\tau_2$ (ns) | $R^2$ | $\tau_{ampl}$ (ns) |
|---|---|---|---|---|
| 1 | 1.31 ± 0.03 | 9.60 ± 0.29 | 0.998 | 7.3 |
| 2 | 1.14 ± 0.02 | 7.80 ± 0.09 | 0.999 | 5.6 |
| 3 | 1.17 ± 0.02 | 7.91 ± 0.12 | 0.998 | 5.7 |
| 4 | 1.30 ± 0.01 | 9.05 ± 0.11 | 0.999 | 6.8 |
| 5 | 1.06 ± 0.07 | 7.44 ± 0.32 | 0.998 | 5.5 |

|  | $\tau_1$ (ns) | $\tau_2$ (ns) | $R^2$ | $\tau_{ampl}$ (ns) |
|---|---|---|---|---|
| 1 | 1.44 ± 0.03 | 9.42 ± 0.26 | 0.997 | 7.3 |
| 2 | 1.42 ± 0.03 | 8.36 ± 0.15 | 0.998 | 5.7 |
| 3 | 1.43 ± 0.04 | 10.09 ± 0.28 | 0.997 | 7.7 |

***Figure S3.6.*** *Data of the photoluminescent lifetime experiments that are represented in* ***Figure 3*** *in the main article. Data includes, from top left to bottom right, the transmission image, the PL lifetime image with the probed positions (Both included in the manuscript as well), the PL lifetime image with the emission maxima for the probed positions, the measured lifetime decay data, the table with the fitted parameters and the obtained PL emission spectra with the wavelengths of the corresponding emission maxima.*

# Chapter 4

## Rationalizing Acid Zeolite Performance at the Nanoscale by Correlative Fluorescence and Electron Microscopy

**Jordi Van Loon**, Kris P.F. Janssen, Thomas Franklin, Alexey V. Kubarev, Julian A. Steele, Elke Debroye, Eric Breynaert, Johan A. Martens, Maarten B.J. Roeffaers

Adapted with permission from: *ACS Catal.* **2017**, *7*, 5234–5242

The performance of zeolites as solid acid catalysts is strongly influenced by the accessibility of active sites. However, synthetic zeolites typically grow as complex aggregates of small nanocrystallites rather than perfect single crystals. The structural complexity must therefore play a decisive role in zeolite catalyst applicability. Traditional tools for the characterization of heterogeneous catalysts are unable to directly relate nanometer scale structural properties to the corresponding catalytic performance. In this work, an innovative correlative super-resolution fluorescence and scanning electron microscope is applied and the appropriate analysis procedures are developed to investigate the effect of small-port H-mordenite (H-MOR) morphology on the catalytic performance, along with the effects of extensive acid leaching. These correlative measurements revealed catalytic activity at the interface between intergrown H-MOR crystallites that was assumed inaccessible, without compromising the shape selective properties. Furthermore, it was found that extensive acid leaching led to an etching of the originally accessible microporous structure, rather than the formation of an extended mesoporous structure. The associated transition of small-port to large-port H-MOR therefore did not render the full catalyst particle functional for catalysis. The applied characterization technique allows a straightforward investigation of the zeolite structure-activity relationship beyond the single-particle level. We conclude that such information will ultimately lead to an accurate understanding of the relationship between the bulk scale catalyst behavior and the nanoscale structural features, enabling a rationalization of catalyst design.

## Disclaimer

http://pubs.acs.org/doi/10.1021/acscatal.7b01148

## Contributions

J.V.L. and M.B.J.R. conceived the experiments. J.V.L. performed the correlative experiments and the bulk scale activity testing and was responsible for data analysis. J.A.S. did the Raman measurements and E.B. conducted the NMR characterization. J.V.L., T.F. and K.P.F.J. are in charge of building and maintaining the ILEM setup. J.V.L., and M.B.J.R. prepared the manuscript with contributions from all coauthors.

# Chapter 4 - Rationalizing Acid Zeolite Performance at the Nanoscale by Correlative Fluorescence and Electron Microscopy

## 4.1. Introduction

Zeolites are widely used as solid acid catalysts in both laboratory-scale research and industrial chemical processes.[1–3] Their catalytic activity and chemoselectivity are strongly influenced by the accessibility of individual active sites that are located within the characteristic ordered microporous structure.[4] Structural imperfections such as defects and meso- and macropores are therefore believed to be key determinants of catalyst performance.[5,6] This is specifically true for zeolites with unidirectional pore systems, such as mordenites (MOR). The MOR framework consists of 12- and 8- membered ring channels running along the crystallographic c axis and a network of side pockets oriented along the b axis that are not effectively interconnecting the pores along the c axis.[7] Since molecular transport of most organic molecules can only occur through the 7.0 Å × 6.5 Å sized 12-membered ring (12MR) channels, the MOR framework porosity can be regarded as unidirectional. As a consequence, molecular diffusion is easily obstructed and as-synthesized mordenite crystals therefore often display restricted mass transport.[8] According to literature, this so-called small-port (SP) behavior is most probably caused by crystallographic stacking faults or extra-framework aluminium species deposited in the micropores.[7,9–11] The obstructed molecular accessibility in the micropores of such small-port mordenites (SP-MORs) limits the catalytic activity to pore entrances located near the outer surface of the crystals.[8] These mass transport constraints are typically circumvented by applying post-synthetic dealumination, such as acid leaching or hydrothermal treatments, to introduce mesopores into the structure.

In this work, a newly developed integrated fluorescence and electron microscope (iFlEM) is applied to investigate the effect of SP-MOR nanocrystallite structure on the catalytic performance. The novelty of this research is two-fold. First, we describe the development of a new tool that for the first time enables catalyst structure to be linked to its performance at the nanoscale. The main advantages of using such an integrated instrument instead of independent microscopes are the strongly reduced risk of sample contamination and that, after an initial alignment of the system, structural images and catalytic activity maps are conveniently overlaid. The second novelty is that, in contrast to idealized, micrometer-large crystals which have been used before, this work employed a commonly applied industrial zeolite batch, containing a large amount of complex intergrown particles.

The latter is of importance since most synthetic zeolite batches, including mordenites, do not consist of perfect uniform crystals, but rather a wide range of particle morphologies is present. It often follows that zeolite particles exhibit complex intergrowths and obvious structural defects.[11,12] The influence of this structural complexity on the catalytic performance or post-synthetic dealumination, is not yet understood at the relevant length scales, mainly because traditional analytical methods used in zeolite and catalysis research are unable to directly link the effects of structural imperfections to the impact on the catalytic performance.[4,5,12,13] Particularly for zeolites with a one dimensional porous structure, pore blocking has a tremendous effect on catalyst performance, but this has so far not been directly related to the local catalyst structure.[14] For example, electron microscopy enables the investigation of structural details down to the atomic scale.[15] However, a direct correlation of this structurally resolved information to the catalytic performance, which is typically measured at the bulk scale, cannot be made due to the intrinsically large inter- and intraparticle heterogeneity. At best, the outcome of ensemble averaged catalyst testing can lead to generalized insights on the interplay between catalyst structure and activity.

Fluorescence microscopy has undeniably proven its ability to characterize and visualize the catalytic performance down to the level of individual catalytic conversions.[16,17] More specifically, the optical transparency of zeolites enables the catalytic performance to be mapped out at the nanoscale through Nanometer Accuracy by Stochastic Chemical reActions, or NASCA.[18–20] The interpretation of these spatially resolved performance maps depends on morphological features that can typically be resolved from corresponding optical transmission images of the same catalyst particle. This approach is therefore limited to micrometer-sized crystals with well recognizable morphologies and structures. For example, fluorescence microscopy investigations have led to the elucidation of the impact of intergrowth structures within large H-ZSM-5 crystals on pore accessibility, chemical mobility and catalytic performance.[19,21,22] Alternatively, a number of uniform nanometer sized metal catalyst particles has been investigated.[8,23–25] These spatially resolved studies have so far demonstrated the impact of inter- and intraparticle heterogeneities on the overall catalytic performance.[26] Together these investigations only focused on either large, perfect crystals or relatively small particles that are assumed to be uniform in size and morphology. However, this is not representative for actual industrially employed catalyst powders containing non-uniform nanoparticles and complex aggregates of nanocrystallites. Therefore, it is essential to correlate the nanoscale activity maps recorded by NASCA microscopy to structural information of the same particle at the same length scale.[16]

Detailed structure-activity relationships at the level of individual zeolite catalyst particles were recently obtained by the Weckhuysen group by combining transmission electron microscopy (TEM) with diffraction-limited confocal laser scanning microscopy.[27,28] While very powerful, these static experiments are focused on investigating prestained samples and do not enable super-resolution imaging of the catalytic activity at the nanoscale. Furthermore, care has to be taken not to compromise the local catalyst structure during the sample slicing prior to the experiment. Peng Chen and co-workers alternatively employed correlative fluorescence microscopy and scanning electron microscopy (SEM) to link catalytic activity to the structure of metal nanoparticles.[24,29,30]

This brief summary of earlier efforts to investigate the catalyst structure-activity relationship down to the nanoscale illustrates the relevance of developing an iFlEM approach as applied in the reported work. By linking nanoscale catalyst performance and structure, we uncover the significance of crystal intergrowths that induce extra-framework porosity and their role on catalyst performance before and after acid leaching. Furthermore, it was discovered that there is no significant mesopore creation through extensive acid leaching, demonstrating the need for an additional hydrothermal treatment in order to truly circumvent the small-port behavior of MOR zeolites.

## 4.2. Experimental section

### 4.2.1. Integrated fluorescence and electron microscope

The iFlEM setup consists of an inverted epifluorescence wide-field microscope integrated into an SEM (FEI Quanta 250 FEG), by means of a customized chamber door (SECOM, Delmic BV) (**Figure 4.1**).[31,32] On the outside of the sample chamber, a 532 nm diode pump solid state laser (Omicron laserage) is directed through the chamber window by means of a 442/532 nm dichroic mirror with accompanying excitation filter (**Figure 4.1b**). A 100× 1.4NA CFI plan APO VC oil objective lens (Nikon) located inside the vacuum chamber provides the wide field excitation of the sample. As such, this system provides 1.9 $kW.cm^{-2}$ of excitation light on the sample. To operate the system under vacuum conditions (approximately $1\times10^{-4}$ Pa), 1-Ethyl-3-methylimidazolium acetate is applied as immersion liquid. The generated fluorescence is guided through the optically transparent window and passes through the dichroic mirror and a 542 nm LP emission filter, followed by a 2.5× camera lens in front of the EMCCD camera (Hamamatsu C9100-23B). The optically transparent chamber window is key to the functioning of the integrated system as it allows fluorescence and excitation light to travel through the chamber door. Hence, after venting the system, catalytic activity mapping can be started immediately. The described configuration provides a $32.8 \times 32.8$ $\mu m^2$ field of view and a $64 \times 64$ $nm^2$ pixel size on the investigated sample. Wide-field fluorescence movies were acquired with 30 ms exposure time. The linear polarized light experiments are performed after introducing a Glan-Thompson polarizer (Thorlabs) into the optical pathway before the dichroic mirror. A detailed schematic representation of the iFlEM is provided in the supporting information (**Scheme S4.1**).

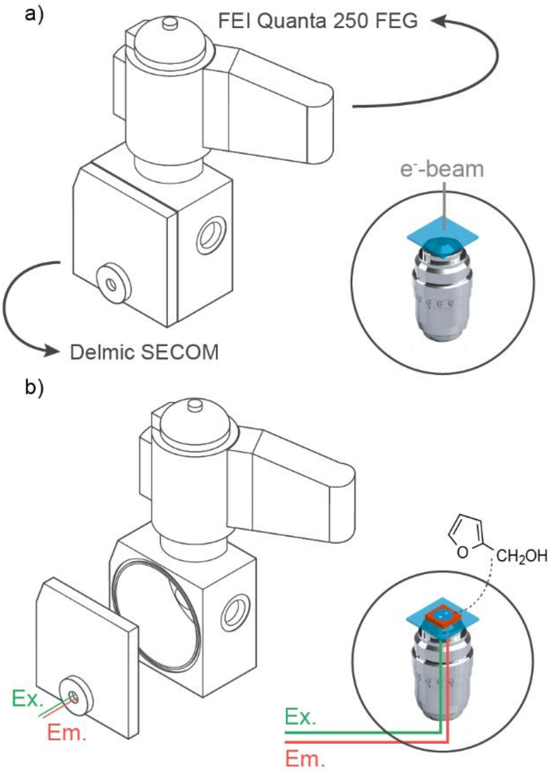

***Figure 4.1.*** *Schematic representation of the iFlEM showing the chamber window that is fitted into the customized SEM chamber door and is essential to the presented approach. The design is based on the SECOM platform (Delmic B.V.). Both subimages also show an inside view of the electron beam/sample/objective lens configuration in the situation that a) a structural image is being acquired with SEM and b) the single turnover precise catalytic activity map is obtained after bringing the sample to atmospheric pressure, attaching a perfusion chamber to the cover slide and adding the reagent solution.*

### 4.2.2.Sample preparation

The SP-MOR sample was obtained from Tosoh Corporation (HSZ-620HOA, Si/Al ratio: 7.5). Two droplets of a 10 mg/ml mordenite in milli Q water suspension were spin-coated onto single-molecule clean cover slides at 3000 rpm for 60 s. These single-molecule clean 22 x 22 #1 cover slides were prepared by calcination for over 24 h in a static air oven at 450 °C, followed by a 1 h ozone treatment in a UV-reactor (Ultra violet products, PR-100). The spin-coated samples were additionally calcined in a static air oven at 450 °C to remove any impurities that could lead to residual fluorescence in the zeolite sample. To ensure that no structural changes were induced in the sample, a stepwise heating scheme was used (Heating ramp of 1 °C/min and a 1 h dwell time at 80 °C and 150 °C, at 450 °C the temperature was held for at least 48 h).

### 4.2.3. Correlated data acquisition

The correlated NASCA experiments were always performed in a similar fashion. The prepared cover slide was attached onto a metal plate sample holder and mounted into the iFlEM. SEM images of the crystals were taken (2 kV, SE, high vacuum mode) (**Figure 4.1a**) after which the sample chamber of the SEM was vented to atmospheric pressure and the chamber door was opened (**Figure 4.1b**). Next, a perfusion chamber (PC8R-1.0-CoverWell, Grace Bio labs) was attached onto the cover slide and 50 µl of an 18 wt% FFA (Sigma Aldrich, 98%, purified through vacuum distillation prior to use) solution in milli Q water was added with a micropipette. Through a set of experiments with varying concentrations, this amount was established as the optimal concentration. The addition of FFA as the fluorogenic reagent leads to the formation of oligomeric reaction products, by means of the acid-catalyzed condensation reaction that is catalyzed on the Brønsted acid sites of the zeolite (**Scheme S4.2**).[17] These oligomers are composed of a conjugated backbone structure that provides the fluorescent properties to enable their observation in fluorescence experiments with single-molecule sensitivity.[19] In the NASCA experiment conducted on the acid leached sample, a reduced 8 wt% FFA in milli Q water solution was added to ensure the single-molecule sensitivity for this catalytically more active sample. For our experiments, only crystals that show little or no background fluorescence were used.

### 4.2.4. NASCA analysis

By fitting the point spread function of single emitters with a two-dimensional Gaussian function, their exact location is determined. The localizer software used to perform this analysis on the recorded fluorescence movies and produce the quantitative activity maps, is available online (https://bitbucket.org/pdedecker/localizer) as a plugin for both Igor Pro (Wavemetrics) and Matlab (MathWorks).[33] The resolution achieved by this approach is approximately 20 nm.[19] Single fluorescent product molecules reappearing in consecutive frames before photobleaching were counted as one catalytic event. The software has a built-in consolidation functionality that finds reappearing molecules within a certain distance, allowing a certain blinking time. For these specific experiments, a respective distance of 50 nm and blinking time of 90 ms were employed. All the parameters mentioned above were obtained after a careful evaluation of different combinations of the different parameters. The quantitative NASCA images that result from this analysis are obtained by binning the data into 50 × 50 nm$^2$ areas. By additionally considering the imaging depth as a measure for the thickness of every voxel, i.e. 500 nm, the corresponding catalytic activity is obtained, which is represented by assigning a color scale to the resulting activity map.

### 4.2.5.The overlay procedure

The correlated micrographs shown in **Figures 4.2**, **4.3** and **4.4** were created using the image registration tool available in ImageJ. By selecting the same two reference points on both the qualitative activity map (produced using the localizer software) and the electron micrograph, the correct magnification, rotation and translation is obtained that is needed to accurately overlay both images. By merging the resized qualitative activity map and the electron micrograph with the merge channels command, the correlated micrograph is obtained. The cyan colored dots displayed on the SEM micrographs in this work represent the position where at least one turnover has taken place.

### 4.2.6.Molecular size calculation

The molecular diameters of FFA and pyridine were calculated using MarvinSketch (version 15.9.21.0), developed by ChemAxon.

### 4.2.7.Reaction-pore confinement analysis

The Matlab analysis procedure that has been developed to perform the reaction-pore confinement analysis is available online (https://drive.google.com/open?id=0ByLzCpEAweEkbTdHQllxeUlzRkE). In this analysis, the NASCA image data obtained from analyzing the respective linear polarized light experiments, using the localizer software and binning them into 200 × 200 nm$^2$ zones, are used as input. The two separate data sets are carefully screened for drift using a built-in drift check function. The reaction-pore confinement plot in **Figure 4.3e** has been drift corrected for + 64 nm along the y axis. No drift correction was needed to obtain the reaction-pore confinement plot of the $HNO_3$ leached sample. A second parameter is set as the lower limit (LL). As such, any bins in the image only composed of fluorescent background molecules are filtered out. The LL for the analysis of the performed experiments is set to 5 turnovers. Finally, an upper threshold is set for the transparency range that qualitatively displays the number of turnovers detected within the respective bins. The threshold is set at 10% of the maximal bin value obtained by summing the turnovers of both linear polarized light experiments in every bin.

### 4.2.8.Acid leaching

Dealumination has been achieved by refluxing 1 g of the SP-MOR zeolite sample at 90 °C for 8 h using 20 ml of a 1 M $HNO_3$ (Sigma-Aldrich, 65%) in milli Q solution while vigorously stirring the slurry. The acid leached zeolite was separated from the acidic solution by means of Büchner-filtration using warm distilled water until the permeate obtained a neutral pH. Finally, the zeolite was dried in a static air oven for 24 h at 85 °C.

### 4.2.9.Bulk scale characterization

Elemental analysis of the $HNO_3$ leached sample has been performed using ICP-OES (Varian 720-ES). $N_2$-adsorption isotherms have been obtained at -196 °C (Micromeritics 3Flex 3400 physisorption instrument). The reference and $HNO_3$ treated samples have been degassed prior to the experiment for 4 h at 250 °C under vacuum conditions (1 Pa). The specific surface area has been obtained by BET-analysis. $^{27}Al$ spectra were acquired on a Bruker 500 MHz spectrometer, spinning the sample at 10 kHz at the magic angle. The spectra were recorded using a one pulse sequence with pi/12 pulses of 2.90 μs using a recycle delay of 0.8 s and referenced to a solution of 0.5 M $Al(NO_3)_3$ dissolved in 0.5 M $HNO_3$. Each spectrum was acquired with 1024 scans using a spectral width of 19607 Hz recorded with a 2048 point FID size and processed with a 5 Hz apodization.

### 4.2.10. Bulk scale reactivity testing

The bulk scale naphthalene isopropylation reaction was performed in the liquid phase using a high-pressure 15 ml TOP reactor for 8 h at 200 °C and under $2 \times 10^6$ Pa of $N_2$ gas (99.999%). A figure of the apparatus was added to the supporting information (**Figure S4.1**). The reaction mixture consisted of 1.84 mmol naphthalene (Sigma-Aldrich, ≥ 99%), 4 mmol 2-propanol (Biosolve ≥ 99.8%), 9 ml cyclohexane (Sigma-Aldrich, ≥ 99.8%) and 100 mg of the MOR catalyst. The catalyst powder is used as provided by the manufacturer or as obtained after acid leaching, i.e. crystal size 1-3 µm and average particle size 18 µm. After 8 h of reaction the reactor was cooled by placing it in an ice bath. The reaction mixture was analyzed using a gas chromatograph (Shimadzu, CP-Sil 8, FID detector) in split injection mode (split ratio 20) using $N_2$ carrier gas. After injection, the temperature was programmed as follows: 5 min hold at 40 °C, heating to 280 °C at 4 °C/min and finally a 10 min holding time. 2 mmol n-tetradecane (TCI, ≥ 99%) was added as internal standard for quantitative gas chromatography (GC) analysis. Identification of the compounds was carried out using gas chromatography-mass spectrometry.

### 4.2.11. Pyridine staining

Prior to pyridine adsorption, the mordenite sample is dropcasted and calcined as described in the sample preparation paragraph. After calcination, the cover slides, that are contained in glass vails, are cooled down to approximately 280 °C. At this point two droplets of pyridine (Sigma Aldrich, ≥ 99%) are pipetted onto the bottom of the vail, the glass vail is closed using its lid and the sample is left for several hours for the adsorption to take place.

### 4.2.12. Raman experiments

The Raman experiments were performed using a Zeiss 100x 1.3 NA oil immersion objective lens and a Coherent argon-ion gas laser, tuned to operate at 488 nm. This resulted in a spot size of approximately 460 nm and a spatial resolution of approximately 230 nm, used to probe intergrown particles at discrete locations. The micro-probe power density used was 15 kW.cm$^{-2}$, which is well below the damage threshold limit. The relative amount of pyridine adsorbed at the different positions in the different samples is quantified by determining the ratio of the pyridine to mordenite band intensity from the Raman spectra.

## 4.3. Results and discussion

Using the iFlEM approach, detailed electron micrographs of the H-MOR catalyst particle at study are collected from the top of the sample and linked to catalytic activity maps of the same catalyst particle obtained from the bottom-side of the sample (**Figure 4.1**). The latter is achieved by measuring single catalytic turnovers using the fluorescence microscope after addition of an aqueous furfuryl alcohol (FFA) solution. Localization and accumulation of the individual fluorescent reaction products results in nanoscale activity maps.[17,19] **Figure 4.2a** shows a typical scanning electron micrograph of an intergrown crystal in an industrial H-MOR batch, which mainly contains aggregated SP-MOR crystals. The corresponding schematic representation is presented in **Figure 4.2b**. The different MOR crystals that make up the aggregate are pseudo-colored as a guide for the eye and to simplify the later discussion. Here, the small blue H-MOR crystal protrudes the larger orange crystal and at the opposite side a large defect is present. Judging from the shape of the defect, it likely results from another intergrown crystallite that has broken off. After this detailed morphological characterization, FFA was added to the SP-MOR cluster, enabling the visualization of single acid-catalyzed turnovers by recording the fluorescent FFA oligomer formation. The individual fluorescent reaction products were subsequently localized with nanometer precision and their locations (cyan dots) overlaid with the high-resolution SEM image, as shown in **Figure 4.2c**. Since the optical focus was centered around the middle of the aggregate, the recorded catalytic events originate from an optical slice around the center of the aggregate of approximately 500 nm thick (**Scheme S4.1**). This is also apparent from the location of the recorded catalytic events with respect to the scanning electron micrograph.

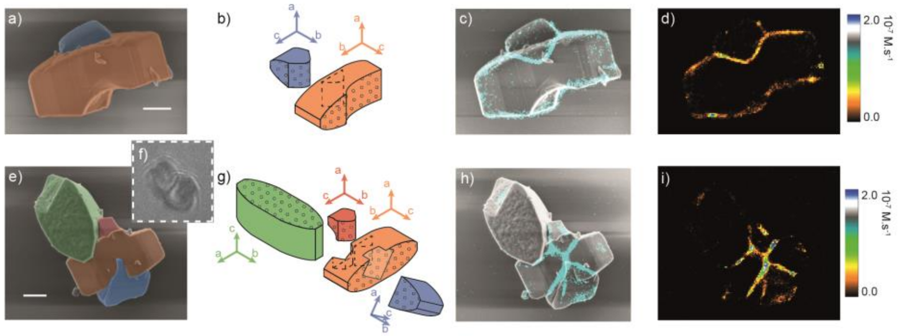

***Figure 4.2.*** *Images recorded using the iFlEM of two intergrown SP-MOR particles. (a, e) Pseudo-colored scanning electron micrographs of intergrown crystallites and (b, g) the corresponding schematic representations indicating the different crystallographic axes. The (001) facets, where the 12MR channels surface, are marked by the dotted pattern indicating the 12MR pore entrances (For the original images, see* ***Figure S4.2*** *and* ***Figure S4.3****). (c, h) Overlay images of the detected individual fluorescent products (cyan dots) on the scanning electron micrographs, referred to as correlative micrographs and (d, i) the quantitative NASCA images obtained by binning the turnovers in 50 × 50 nm$^2$ zones. (f) Optical transmission image of the second aggregate. Scale bars: 1 µm.*

The majority of the observed catalytic events is clustered in a zone of about 300 nm wide, delineating the outer surface of the aggregated particle. This is indicative for small-port behavior as the size of the FFA reagent molecule should enable diffusion through the 12MR channels (molecular diameter is about 6.1 Å) and earlier research on MFI type zeolites with a characteristic 10MR microporous structure has additionally revealed full accessibility.[8,17,34] Importantly, experiments in this work are performed shortly after the addition of FFA and during this period the catalytic activity remains constant. The observed small-port behavior is therefore assumed to be an effect of mass transport limitations rather than pore blocking, which might gradually occur by accumulation of oligomers. In the latter case, the catalytic activity would decrease during the experiment. Secondly, varying numbers of turnovers are observed within the active zone. The small-port behavior becomes even clearer when looking at the NASCA image obtained in **Figure 4.2d** by binning the measured catalytic turnovers into 50 × 50 nm$^2$ zones, which yields a quantitative view on the matter. In the main crystal (orange), most of the acid-catalyzed oligomerization reactions are limited to two opposite crystal facets. Based on the crystallographic structure, in combination with the morphology of the crystals, these slightly curved and roughened facets are identified as the crystallographic (001) facets where the 12MR pores are surfacing.[8,35] This observation shows that catalytic conversions in SP-MOR are limited to the acid sites available in the first few hundreds of nanometers behind the 12MR pore mouths. At the other facets the microporous zeolite framework and, hence, the catalytically active sites, are not accessible towards the FFA substrate. Note that the sparse turnovers detected at these facets can be related to acid sites at the outer surface or minute crystal imperfections. Surprisingly, also a significant number of catalytic turnovers is observed away from the outer surface and inside the main crystal, in the zone underneath the intergrown crystal at the top. The width of this catalytically active zone is comparable to that at the (001) facets at the crystal exterior. Judging from the shape of this catalytically active area, it can be assigned to the interface between the intergrown crystals, i.e. the highly defective area between the blue and orange crystals. Note that the activity of this region is similar to that observed at the readily accessible (001) facets and that no activity gradient is observed from the outside of the crystal towards the most deeply buried part of the intergrowth. It can therefore be concluded that the extra-framework porosity at this interface is sufficient to allow reagent molecules to readily reach the active sites along the intergrowth.

**Figure 4.2e and f** display the scanning electron micrograph and optical transmission image of another SP-MOR aggregate in this industrial H-MOR batch. A direct comparison clearly demonstrates that the structural complexity of small particles in typical zeolite samples cannot be captured by diffraction limited optical imaging. From the scanning electron micrograph, the structural details of this aggregate can be resolved, with the corresponding schematic representation shown in **Figure 4.2g**. The crystal at the top part (green) is a nearly complete crystal with an obvious defect at the top. Again, from the shape of the defect, it seems to have resulted from a broken off intergrown crystallite. Judging from the morphology of the particle (*vide supra*) the 12MR micropores run perpendicular to the rough (001) top facet along the optical z axis. In the center of the aggregate another large crystal (orange) is present, perpendicular to the top (green) crystal. The 12MR pores in this crystal run parallel to the imaging plane, connecting the curved (001) facets where two more protruding crystals (red and blue) are present. The slightly different orientation of these two protruding crystals suggests that both are independent of each other.

Similar to the first aggregate (**Figure 4.2a-d**), the catalytic reactivity of this particle was measured by adding the fluorogenic FFA reagent solution and subsequently localizing the individual catalytic turnovers. **Figure 4.2h** shows the positions of localized individual catalytic events overlaid with the corresponding electron micrograph. The corresponding NASCA image is shown in **Figure 4.2i**. The interface of the central crystal (orange) with the intergrown crystals (red and blue) results in a highly active x-shaped zone of activity. Additionally, significant catalytic activity is observed at the interface between the central (orange) and top (green) crystals. The width of the catalytically active zones, measuring about 300 nm, and the absence of an activity gradient within this zone is in line with earlier observations on the first aggregate. The absence of catalytic activity in the upper (green) crystal can be explained by the orientation of the crystal; the 12MR micropores run parallel to the propagation direction of the excitation light (optical Z axis). As the fluorescent product molecules are spatially constrained within the microporous structure, the molecules will be aligned along the micropore orientation. This results in a minimal overlap between the electric field vector of the excitation light and the transition dipole moment of the fluorescent product molecules.[8,36]

Clearly, the absence of a perfect co-alignment between the crystal lattices of the intergrown crystals results in a local discontinuity of the zeolite framework at the boundary between these SP-MOR crystals. The resulting extra-framework porosity facilitates molecular diffusion and leads to an enhanced molecular accessibility. As such, this results in a zone of high catalytic activity at the interface between the individual crystallites, away from the outer surface. The catalytic activity at these intergrowths accounts for respectively 28 and 67% of the total catalytic activity observed in the two examples. This data clearly underlines the importance of intergrowths on the overall performance of these H-MOR zeolites. At the same time, these results, showing activity away from the outer surface, also indicate that an aluminium gradient cannot be the origin of the observed activity profile, i.e. active crystallite edges and inactive crystallite center. On the other hand, it cannot be deduced from these observations whether this catalytic activity is only linked to acid sites within the SP-MOR micropores or if some portion of the activity is linked to defect sites at the highly defected interface. This is important, since the latter would have a negative impact on the shape selectivity.[37,38] Whereas product molecules formed within the confinement of the microporous structure are expected to be aligned along the 12MR pore direction, molecules formed on active sites directly located on the highly accessible intergrowth boundary should not show any preferential orientation.[8,36] Hence, the orientation of the fluorescent product molecules with respect to the one-dimensional porous structure is a good indicator of the pore confinement, which is crucial for shape selectivity. The orientation of fluorescent reaction products can be straightforwardly visualized by implementing linear polarized excitation light.[36]

To quantitatively investigate the pore confinement of individual fluorescent reaction products, an aggregate of three intergrown crystals from the same SP-MOR batch was examined in **Figure 4.3**. In this cluster, the 12MR pores of the respective crystals are oriented almost perpendicular to each other. The aggregate itself was oriented in such a way that the 12MR pores of the individual crystals are along the optical X, Y and Z axes. When exciting with circular polarized light (**Figure 4.3a**), fluorescent oligomers oriented in the XY-plane are detected. A schematic representation of the cluster in which the different axes are assigned is given in **Figure 4.3b**. As observed in **Figure 4.2c** and **h**, catalytic activity is limited to zones of about 300 nm thickness starting from the 12MR pore mouths at the (001) facets and around the intergrowth interfaces. Note that the catalytically active zone along the interface between the middle (green) and left (orange) crystals is broader than the previously observed 300 nm (**Figure 4.2c** and **h**). As the catalytic activity map is a 2D projection of single-turnovers taking place within a 500 nm thick optical slice (*vide supra*), the width of the projection will depend on the relative orientation of the intergrowth structure to the optical section. Clearly, this interface does not follow any of the crystallographic axes of the other two intergrown crystals.

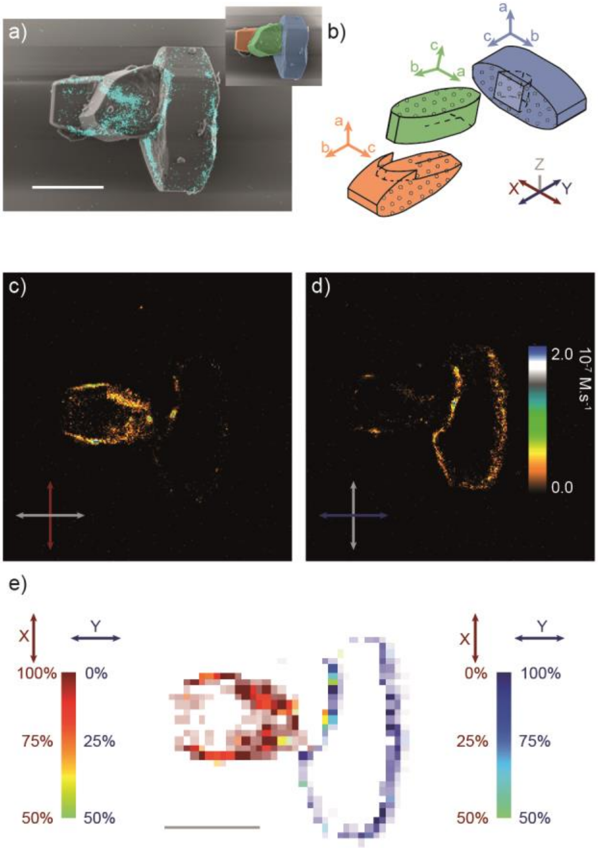

***Figure 4.3.*** *(a) Correlative structure-activity micrograph of a cluster of three intergrown crystallites obtained with circular polarized excitation light (For the original SEM image see* ***Figure S4.4****) and (b) the respective schematic representation with corresponding crystallographic- and optical axes. Pore mouths of the 12MR are marked by the dotted pattern. The corresponding quantitative activity maps (accumulated activity recorded in 50 × 50 nm$^2$ project zones) are obtained with linear polarized excitation light along the one-dimensional porous structure in (c) the left (orange) crystal, i.e. the optical x axis, and (d) the right (blue) crystal, i.e. the optical y axis; the polarization direction is indicated by the highlighted optical axis. (e) The reaction-pore confinement plot obtained by combining the information from (c) and (d), and after binning into 200 × 200 nm$^2$ areas. Scale bars: 3 µm.*

The introduction of a Glan-Thompson polarizer into the excitation pathway of the iFlEM polarizes the excitation light and allows its rotation over $360^0$ in the optical XY-plane. Next, we quantitatively investigate the polarization dependence by specifically employing two perpendicular polarization directions; first along the optical X axis, parallel to the 12MR pores of the orange crystal (**Figure 4.3c**), and, second, along the optical Y axis, parallel to the 12MR pores in the blue crystal (**Figure 4.3d**). This investigation reveals that the formed fluorescent product molecules at the (001) facets of the respective crystals are mostly confined to their respective 12MR pores. When the excitation polarization is oriented along the direction of the 12MR pores of the orange crystal (i.e. the optical X axis), the number of catalytic turnovers observed in the blue crystal reduces drastically compared to the situation in which circular polarization was employed. Even though the catalytic reaction still occurs, the fluorescent product molecules are no longer efficiently excited, as the polarization direction of the excitation light is perpendicular to the orientation of the molecular excitation transition dipole moment. On the other hand, the opposite effect is observed when the polarization plane is oriented parallel to the optical Y axis (**Figure 4.3d**). In this case, the blue crystal exhibits the majority of the catalytic activity and only a fraction remains excitable and detectable in the orange crystal. Surprisingly, the same observation holds for the fluorescent product molecules formed at the intergrowth regions of the two crystals with the middle green crystal. As the 12MR pores of the latter crystal are oriented along the optical Z axis, no significant contribution to the catalytic activity map is expected from the molecules confined within the microporous structure. Therefore, this is direct proof of the pore-confinement of reaction products near crystalline defect such as intergrowth interfaces.

Combining the information from **Figure 4.3c and d** into one reaction-pore confinement plot shows the local orientation of product molecules with respect to the 12MR pores: red-to-green and blue-to-green color scales are indicative of a transition from a situation in which all fluorescent product molecules are confined within the 12MR pores in the orange and blue crystals, respectively, to a situation where there is no preferential orientation (green) (**Figure 4.3e**). The color intensity of each pixel provides a qualitative indication of the relative number of turnovers occurring in this zone. The reaction-pore confinement plot resulting from the aggregate in **Figure 4.3** mainly shows red and blue zones, corresponding to a confinement of approximately 86% over the whole particle. This value is obtained by determining the ratio of the number of fluorescent product molecules oriented along the local microporous structure, to the total number of catalytic turnovers observed over the catalyst particle. As such, this number represents the shape selectivity of the individual catalyst particle based on the FFA probe reaction.

The reaction-pore confinement determined during this experiment reveals that active sites are predominantly confined within the microporous structure as reaction products are preferentially oriented along the one-dimensional 12MR pores. However, catalytic activity is observed on all intergrowth structures, regardless of the crystallographic facets that are included. The formation of the crystallographic surface is therefore assumed to be incomplete where intergrowth formation has taken place. This leads to an opening up of the microporous structure. Additionally, active sites accessible through intergrowth structures are as reactive as those accessible through the intrinsic pore mouths on the (001) facets. This is an indication that mass transport inside intergrowths is unrestricted. As such, intergrowth structures are regarded as macroporous voids that facilitate mass transport towards catalytically active sites located within the opened up crystallographic framework.

One method commonly applied to enhance molecular transport in SP-MOR catalysts is acid leaching, removing both framework and extra-framework aluminium species hindering molecular transport along the 12MR pores. Already in 1983, Raatz et al. reported that selective leaching of about 20% of the total aluminium content converts SP-MOR into the large-port form.[10] Since then, such post-synthetic treatments have become routine practice in H-MOR catalytic research.[39] The sample under investigation in this study was submitted to acid leaching by refluxing the SP-MOR zeolite sample in a $HNO_3$ solution.[40] Typically, the effect of this procedure on the zeolite and its catalytic performance is investigated by means of bulk-scale analysis, such as atomic spectroscopy to determine bulk Si/Al ratio, or solid state nuclear magnetic resonance (NMR) to discriminate between framework ($Al^{IV}$) and extra-framework aluminium ($Al^{VI}$). Here, bulk analysis using inductively coupled plasma optical emission spectrometry (ICP-OES) revealed that about 30% of the aluminium was removed from the zeolite sample and $^{27}Al$ NMR data additionally showed a slight preference towards extra-framework $Al^{VI}$ removal.[c] $N_2$-physisorption revealed a small increase in micropore and external surface area. Finally, also a bulk scale naphthalene isopropylation reaction was performed on the mordenite catalysts.[d] As such, the reactivity trends and shape selectivity properties, observed at the single particle level, before and after acid leaching, could be validated using an industrially relevant bulk scale process. The naphthalene isopropylation reaction revealed an increased activity from < 1% conversion, to 8% after $HNO_3$ leaching, indicating that after the SP-MOR sample indeed became more active towards the alkylation of bulky organic molecules after the acid treatment. A summary of these bulk scale experiments can be consulted in the supporting information.

A combination of the newly developed iFlEM approach with the analysis tools introduced above provides a novel way to investigate the effects of acid leaching beyond the bulk scale. **Figure 4.4** reveals the reaction-pore

---

[c] See Annex 1 to Chapter 4, p95

[d] See Annex 2 to Chapter 4, p96

confinement for an $HNO_3$ treated aggregate consisting of three orthogonally intergrown crystals. The orange crystal is oriented with its 12MR pores running along the optical y axis and the 12MR pores in the green crystal run parallel to the optical z axis. Additionally, a smaller crystallite (blue) is intergrown with the green crystal.

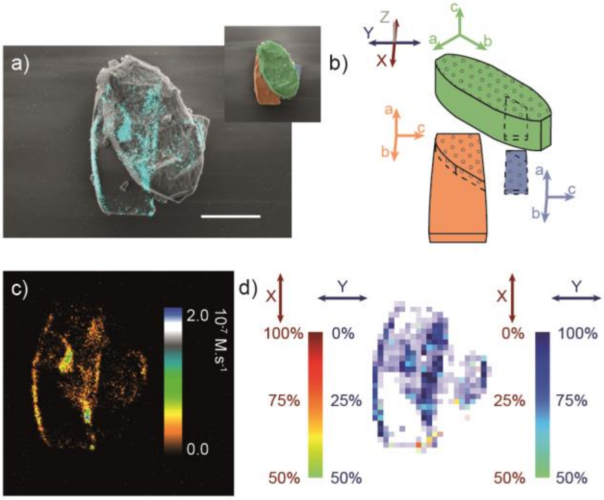

*Figure 4.4.* *(a) Correlative structure-activity micrograph of three intergrown crystallites treated with $HNO_3$ obtained with circular polarized excitation light (For the original SEM image see **Figure S4.5**) and (b) the respective schematic representation. The (001) facets, where the 12MR channels surface, are marked by the dotted pattern. (c) The corresponding quantitative activity map is obtained by using a 60% reduced fluorogenic reagent concentration compared to the previous experiments and the recorded activity is accumulated in 50 × 50 nm$^2$ zones. (d) The molecular confinement plot is recorded by combining the information from the linear polarized excitation experiments as introduced in **Figure 4.3e** and after rebinning into 200 × 200 nm$^2$ areas. Scale bar: 2 µm.*

The correlated micrograph and quantitative activity map in **Figure 4.4a** and **c** show that the catalytic activity in the acid leached particle still predominantly resides at the edges of the orange crystal and the intergrowth, between the orange and green crystals. Furthermore, there is a zone of moderate catalytic activity in the green crystal which is attributed to the small intergrown blue crystal. As it is located beneath the green crystal, both the morphology of this crystal and the exact orientation of the intergrowth remain unresolved by means of SEM imaging. However, based on the information obtained from the reaction-pore confinement plot (**Figure 4.4d**), it is fair to assume that the orientation of the blue crystal is similar to that of the larger orange crystal. Note that the fluorogenic reagent concentration was reduced because of the increased reactivity over the untreated H-MOR sample (**Figure S4.7**). This increased reactivity is in line with the results from the bulk scale naphthalene isopropylation reaction. Additionally, the reaction-pore confinement plot in

**Figure 4.4d** only reveals a slightly reduced molecular confinement of 83%. These results further confirm the earlier assumption that the formation of intercrystalline intergrowths lead to a locally enhanced access to the microporous structure. The effect of the acid treatment would otherwise be much more effective if the intergrowths existed of combined micro-, meso-, and macroporous regions.

The presented nanoscale structure-activity experiments are a representative subset of a larger number of experiments (n = 10) and reveal that the location of the catalytic activity in H-MOR zeolites is not dramatically influenced by typical acid leaching. In earlier research, Liu et al. demonstrated that severe dealumination, removing more than 50% of the framework aluminium, was necessary to render the full catalyst particles accessible.[8] In their work, dealumination was achieved by means of a combined hydrothermal and acid treatment. Where acid leaching mainly enhances the local reactivity by etching the easily accessible microporous structure, the hydrothermal treatment introduces extensive meso- and macoporous defects that render the full catalyst particle accessible.

Intergrowth structures are affected to the same extent as the intrinsically active edges of the crystals, despite the former being much more defected. Even though over 30% of the aluminium has been removed, the H-MOR still displayed the typical reaction distribution and shape selective properties associated with small-port behavior, and therefore no transition from small-port to large-port H-MOR seemed to have taken place. Small- or large-port behavior is typically revealed by performing static benzene uptake experiments,[9,10] pyridine adsorption has been investigated using Raman spectroscopy to mimic such static experiments and confirms our findings based on the FFA oligomerization reaction. This approach involves the investigation of pyridine uptake before and after acid leaching in targeted areas of an intergrown particle; the crystallite edge, center and on the interparticle intergrowth. The results are shown in the supporting information (**Figure S4.8** and **Table S4.4**).

The pyridine uptake experiments indeed show an opening up of the microporous network and thus a transition of small-port to large-port H-MOR, even though pyridine is a bulkier molecule than the FFA reagent (molecular diameter for pyridine is about 6.7 Å). This significantly increased pyridine uptake in all three selected areas of the acid leached particle seems to contradict the outcome of the NASCA experiments. The discrepancy between both experiments can be explained by the dynamic aspect of the NASCA experiments in which molecular transport also plays a significant role. On the contrary, the pyridine distribution is determined after reaching equilibrium. Hence, we believe that the fluorogenic reaction gives a more accurate picture of the catalytically relevant domains. Alternatively, the presented observations could be interpreted as being an effect of Al zoning, however, this effect has not been reported for the MOR sample.[8]

## 4.4. Conclusion

In conclusion, the catalytic performance of acid zeolite nanocrystallites was studied by linking the catalytic performance, as observed in super-resolution fluorescence microscopy, to structural features of the same crystallite recorded by scanning electron microscopy. This enabled, for the first time, a direct observation of the effect of defects and intergrowths, commonly present in powdered zeolite batches, on the overall performance. First, intercrystalline intergrowth structures in SP-MOR aggregates were demonstrated to have a major contribution to the overall activity. The molecular confinement plots revealed that reaction products at the defect-rich intergrowth boundary preferentially align with the 12MR pores rather than taking random orientations. Hence, catalytically active sites at intergrowths are mainly located within the microporous structure. The intergrowth structure is therefore identified as a void space that allows unrestricted mass transport, enabling reactions to occur in the adjacent micropores. Secondly, dealumination by acid leaching mainly affects the intergrowths and the crystal edges. Surprisingly, even though more than 30% of aluminium was removed and pyridine adsorption experiments showed a transition from small-port to large-port H-MOR, the reactivity pattern was not altered. Furthermore, a similar reaction-pore-confinement is observed on the crystal edges and intergrowths, before and after acid leaching, indicating the importance of such intergrowths for the overall catalyst performance. This is relevant information with the aim of rationalizing catalyst synthesis. Full catalytic utilization of the zeolite material on the other hand requires more severe post-synthetic treatments e.g. more extensive acid leaching or a combination with hydrothermal treatment.[8,36,41] Future research should focus on the role of intercrystalline intergrowth structures with respect to catalyst coking and mesopore creation through hydrothermal treatment. Additionally, this line of research would benefit from the development of an *in situ* liquid cell that enables truly integrated experiments, allowing the fluorogenic reaction to be conducted within the vacuum of the SEM chamber.

## 4.5. References

(1) Maria, J. C.; Avelino, C. *Zeolites and Catalysis: Synthesis, Reactions and Applications*; Jiri, C., Avelino, C., Stacey, M. Z., Eds.; Wiley-VCH: Weinheim, 2010.

(2) James, A. D.; George, W. H.; Michel, B. *Handbook of Heterogeneous Catalysis*; Gerhard, E., Helmut, K., Ferdi, S., Jens, W., Eds.; Wiley-VCH: Weinheim, 2008.

(3) Jens, H. *Industrial Catalysis: A Practical Approach*, 2nd ed.; Jens, H., Ed.; Wiley-VCH: Weinheim, 2006.

(4) De Cremer, G.; Sels, B. F.; De Vos, D. E.; Hofkens, J.; Roeffaers, M. B. J. *Chem. Soc. Rev.* **2010**, *39* (12), 4703–4717.

(5) Janssen, K. P. F.; De Cremer, G.; Neely, R. K.; Kubarev, A. V.; Van Loon, J.; Martens, J. A.; De Vos, D. E.; Roeffaers, M. B. J.; Hofkens, J. *Chem. Soc. Rev.* **2014**, *43* (4), 990–1006.

(6) Rolison, D. R. *Science* **2003**, *299* (2003), 1698–1701.

(7) Meier, W. M. *Zeitschrift fur Krist. - New Cryst. Struct.* **1961**, *115* (5–6), 439–450.

(8) Liu, K. L.; Kubarev, A. V.; Van Loon, J.; Uji-I, H.; De Vos, D. E.; Hofkens, J.; Roeffaers, M. B. J. *ACS Nano* **2014**, *8* (12), 12650–12659.

(9) Freund, E.; Marcilly, C.; Raatz, F. *. Chem. Soc., Chem. Commun.* **1982**, 309–310.

(10) Raatz, F.; Marcilly, C.; Freund, E. *Zeolites* **1985**, *5* (5), 329–333.

(11) van Geem, P. C.; Scholle, K. F. M. G. J.; van der Velden, G. P. M. *J. Phys. Chem.* **1988**, *92*, 1585–1589.

(12) Buurmans, I. L. C.; Weckhuysen, B. M. *Nat. Chem.* **2012**, *4* (11), 873–886.

(13) Weckhuysen, B. M. *Chem. Soc. Rev.* **2010**, *39*, 4557–4559.

(14) Magnoux, P.; Cartraud, P.; Mignard, S.; Guisnet, M. *J. Catal.* **1987**, *106* (1), 242–250.

(15) Lu, J.; Roeffaers, M. B.; Bartholomeeusen, E.; Sels, B. F.; Schryvers, D. *Microsc Microanal* **2014**, *20*, 42–49.

(16) Roeffaers, M. B. J.; Cremer, G. De; Uji-i, H.; Sels, B. F.; Jacobs, P. A.; Schryver, F. C. De; Vos, D. E. De; Hofkens, J. *PNAS* **2007**, *104*, 12603–12609.

(17) Roeffaers, M. B. J.; Sels, B. F.; Uji-i, H.; Blanpain, B.; L'hoëst, P.; Jacobs, P. A.; De Schryver, F. C.; Hofkens, J.; De Vos, D. E. *Angew. Chemie - Int. Ed.* **2007**, *46* (10), 1706–1709.

(18) Roeffaers, M. B. J.; Sels, B. F.; Uji-I, H.; De Schryver, F. C.; Jacobs, P. a; De Vos, D. E.; Hofkens, J. *Nature* **2006**, *439* (7076), 572–575.

(19) Roeffaers, M. B. J.; De Cremer, G.; Libeert, J.; Ameloot, R.; Dedecker, P.; Bons, A. J.; Bückins, M.; Martens, J. A.; Sels, B. F.; De Vos, D. E.; Hofkens, J. *Angew. Chemie - Int. Ed.* **2009**, *48* (49), 9285–9289.

(20) Xu, W.; Kong, J. S.; Yeh, Y.-T. E.; Chen, P. *Nat. Mater.* **2008**, *7* (12), 992–996.

(21) Karwacki, L.; Stavitski, E.; Kox, M. H. F.; Kornatowski, J.; Weckhuysen, B. M. *Angew. Chemie - Int. Ed.* **2007**, *46* (38), 7228–7231.

(22) Tachikawa, T.; Yamashita, S.; Majima, T. *J. Am. Chem. Soc.* **2011**, *133* (18), 7197–7204.

(23) Ristanović, Z.; Kerssens, M. M.; Kubarev, A. V.; Hendriks, F. C.; Dedecker, P.; Hofkens, J.; Roeffaers, M. B. J.; Weckhuysen, B. M. *Angew. Chemie - Int. Ed.* **2015**, No. 307523, 1836–1840.

(24) Zhou, X.; Choudhary, E.; Andoy, N. M.; Zou, N.; Chen, P. *ACS Catal.* **2013**, *3*, 1448–1453.

(25) Han, K. S.; Liu, G.; Zhou, X.; Medina, R. E.; Chen, P. *Nano Lett.* **2012**, *12* (3), 1253–1259.

(26) Plessers, E.; Stassen, I.; Sree, S. P.; Janssen, K. P. F.; Yuan, H.; Martens, J.; Hofkens, J.; De Vos, D.; Roeffaers, M. B. J. *ACS Catal.* **2015**, *5* (11), 6690–6695.

(27) Karreman, M. A.; Buurmans, I. L. C.; Geus, J. W.; Agronskaia, A. V.; Ruiz-Martínez, J.; Gerritsen, H. C.; Weckhuysen, B. M. *Angew. Chemie - Int. Ed.* **2012**, *51* (6), 1428–1431.

(28) Karreman, M. A.; Buurmans, I. L. C.; Agronskaia, A. V.; Geus, J. W.; Gerritsen, H. C.; Weckhuysen, B. M. *Chem. - A Eur. J.* **2013**, *19* (12), 3846–3859.

(29) Sambur, J. B.; Chen, T.-Y.; Choudhary, E.; Chen, G.; Nissen, E. J.; Thomas, E. M.; Zou, N.; Chen, P. *Nature* **2016**, *530* (7588), 77–80.

(30) Andoy, N. M.; Zhou, X.; Choudhary, E.; Shen, H.; Liu, G.; Chen, P. *J. Am. Chem. Soc.* **2013**, *135* (5), 1845–1852.

(31) Liv, N.; Zonnevylle, A. C.; Narvaez, A. C.; Effting, A. P. J.; Voorneveld, P. W.;

Lucas, M. S.; Hardwick, J. C.; Wepf, R. A.; Kruit, P.; Hoogenboom, J. P. *PLoS One* **2013**, *8* (2), 1–9.
(32) de Boer, P.; Hoogenboom, J. P.; Giepmans, B. N. G. *Nat. Methods* **2015**, *12* (6), 503–513.
(33) Dedecker, P.; Duwé, S.; Neely, R. K.; Zhang, J. *J. Biomed. Opt.* **2012**, *17*, 126008.
(34) Roeffaers, M. B. J.; Ameloot, R.; Bons, A. J.; Mortier, W.; De Cremer, G.; De Kloe, R.; Hofkens, J.; De Vos, D. E.; Sels, B. F. *J. Am. Chem. Soc.* **2008**, *130* (41), 13516–13517.
(35) P. Simoncic; Armbruster, T. *Am. Mineral.* **2004**, *89* (2–3), 421–431.
(36) Kubarev, A. V.; Janssen, K. P. F.; Roeffaers, M. B. J. *ChemCatChem* **2015**, *7* (22), 3646–3650.
(37) Csicsery, S. M. *Zeolites* **1984**, *4* (3), 202–213.
(38) Song, C. *Surf. Chem. Catal.* **2000**, *3* (6), 477–496.
(39) van Donk, S.; Janssen, A. H.; Bitter, J. H.; de Jong, K. P. *Catal. Rev.* **2003**, *45* (February 2015), 297–319.
(40) Giudici, R.; Kouwenhoven, H. W.; Prins, R. *Appl. Catal. A Gen.* **2000**, *203* (1), 101–110.
(41) Nesterenko, N. S.; Thibault-Starzyk, F.; Montouillout, V.; Yuschenko, V. V.; Fernandez, C.; Gilson, J. P.; Fajula, F.; Ivanova, I. I. *Microporous Mesoporous Mater.* **2004**, *71* (1–3), 157–166.
(42) Choura, M.; Belgacem, N. M.; Gandini, A. *Macromolecules* **1996**, *29* (11), 3839–3850.
(43) Bertarione, S.; Bonino, F.; Cesano, F.; Damin, A.; Scarano, D.; Zecchina, A. *J. Phys. Chem. B* **2008**, *112* (9), 2580–2589.
(44) Kim, T.; Assary, R. S.; Marshall, C. L.; Gosztola, D. J.; Curtiss, L. A.; Stair, P. C. *ChemCatChem* **2011**, *3* (9), 1451–1458.

## 4.6. Supporting information

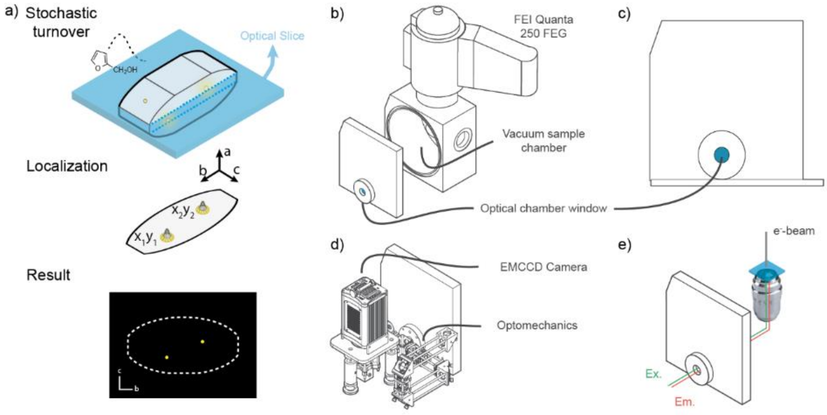

***Scheme S4.1.*** *Schematic representation of the different aspects related to the NASCA experiments and the setup. a) After addition of furfuryl alcohol as the fluorogenic reagent stochastic chemical reactions will occur. Given that they are individually resolved and occurring within the 500 nm thick optical slice, these individual turnovers are detected and subsequently localized by fitting a Gaussian function to their point spread function. After localizing the positions of any detected turnover and accumulating all events occurring within respective bins, the result is a quantitative catalytic activity map. The schematically represented H-MOR particle is accompanied with its respective crystallographic axes, giving an indication of the direction of the one-dimensional porous structure. b) These experiments are performed in a FEI Quanta 250 FEG SEM, equipped with a customized chamber door based on the Secom platform from DELMIC. c) An optically transparent chamber window is integrated into the customized door, d) which contains the necessary optomechanics to perform single turnover precise activity mapping. e) This configuration enables correlative structural and single turnover activity mapping by means of SEM from the top and fluorescence microscopy from the bottom of the sample. The latter is additionally enabled by the incorporation of a vacuum compatible high NA objective lens.*

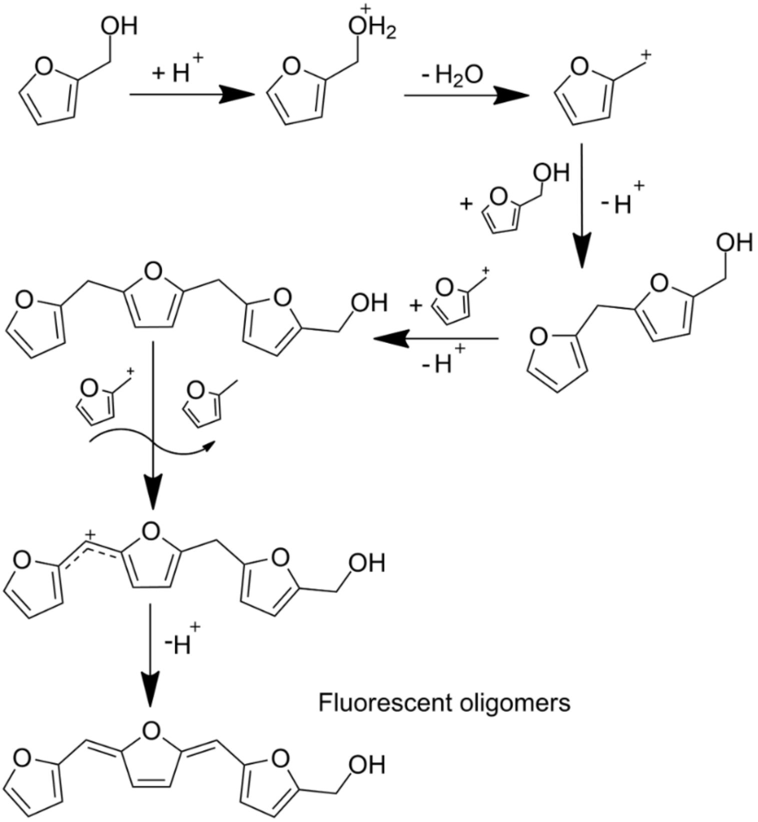

***Scheme S4.2.*** *Reaction scheme of the acid catalyzed furfuryl alcohol oligomerization used as the probe reaction in the described research.*[42–44] *It was shown by Chourra et al. that the trimers with a conjugated system absorb visible light and based on the work of Roeffaers et al., fluorescence resulting from irradiation with 532 nm excitation light is attributed to these species.*[17,42] *The reaction pathway proceeds through an electrophilic aromatic substitution, which represents the major application of solid acid catalysts. The proton that catalyzes the oligomerization reaction is provided by the Brønsted acid sites within the zeolite structure.*

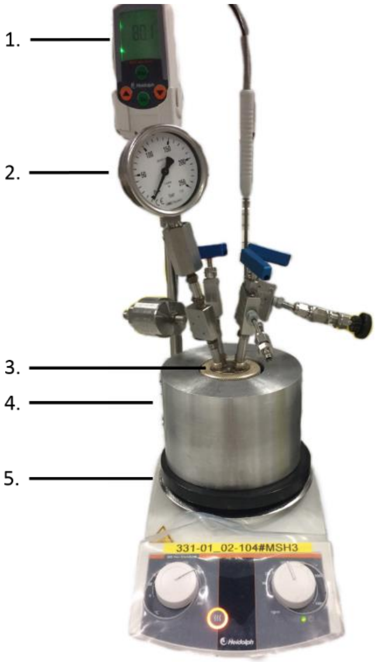

***Figure S 4.1.*** *The apparatus used for the bulk catalysis testing; 1. temperature control, 2. pressure gauge, 3. 15 ml TOP reactor, 4. heating mantle, 5. stirring and heating plate. The reactor was put under 2 × $10^6$ Pa of $N_2$ (99.999%) pressure prior to the experiments through the blue valves.*

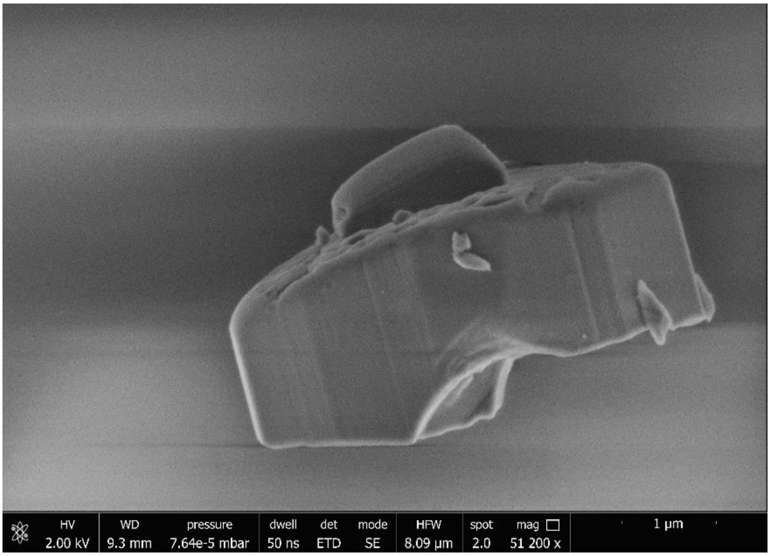

***Figure S4.2.*** *Original SEM image of the small-port mordenite particle investigated in* ***Figure 4.2a-d***.

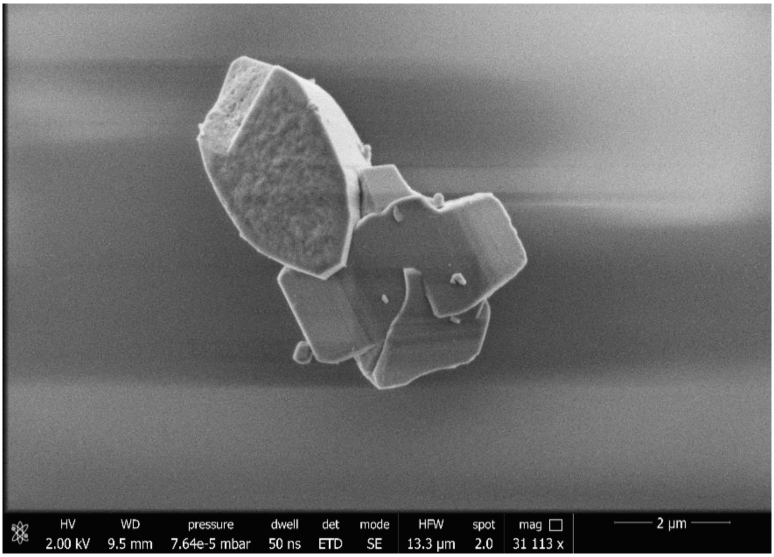

***Figure S4.3.*** *Original SEM image of the small-port mordenite particle investigated in* ***Figure 4.2*****e-i**.

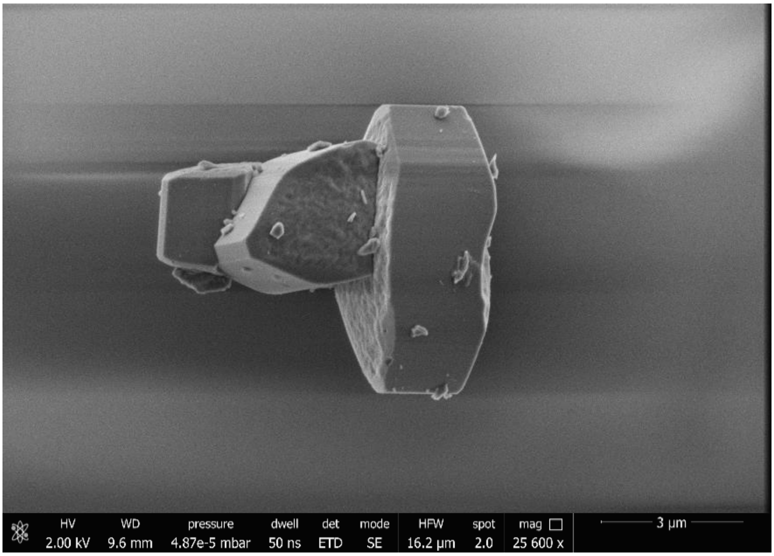

***Figure S4.4.*** *Original SEM image of the small-port mordenite particle investigated in* ***Figure 4.3****.*

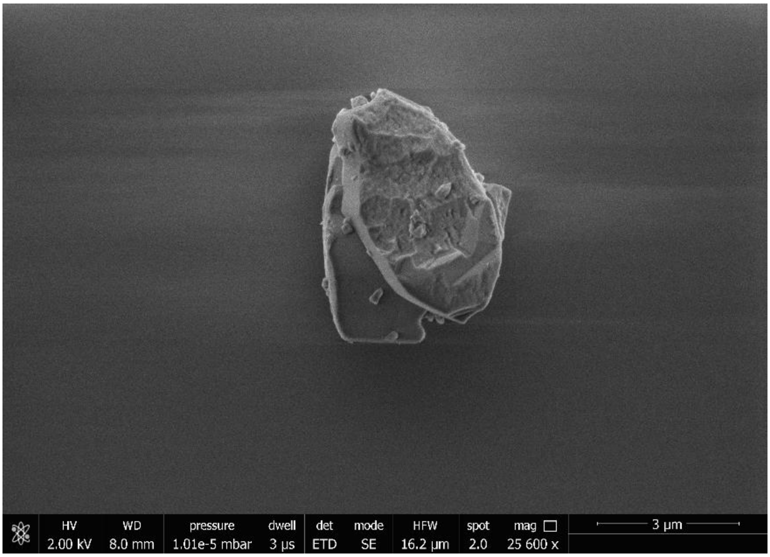

***Figure S4.5.*** *Original SEM image of the $HNO_3$ leached mordenite particle investigated in* ***Figure 4.4****.*

***Table S4.1.*** *Si/Al ratio of the small-port- and $HNO_3$ mordenite samples as determined using ICP analysis.*

| | Si/Al (mol/mol) |
|---|---|
| SP-MOR | 7.5 |
| $HNO_3$ leached MOR | 10.9 |

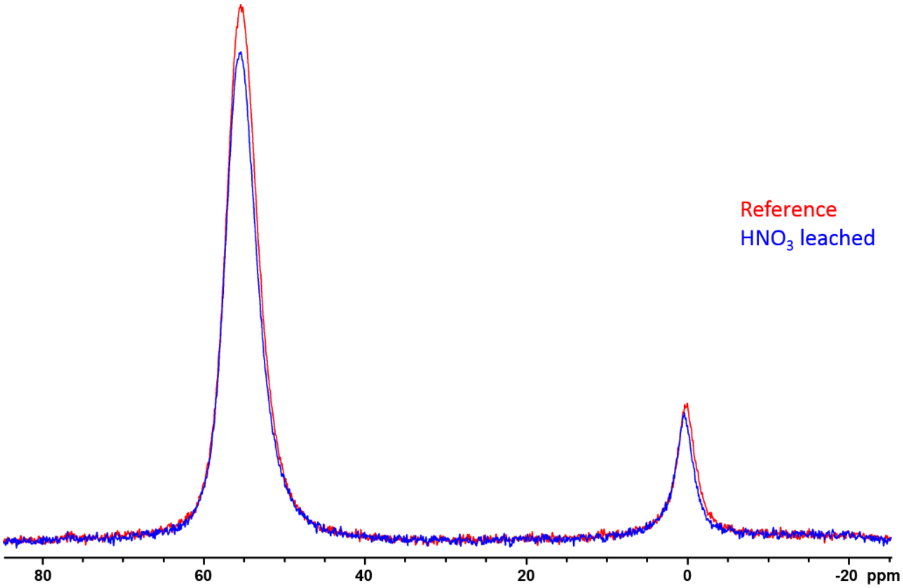

***Figure S4.6.*** *$^{27}$Al-NMR spectra obtained for the small-port mordenite and $HNO_3$ leached mordenite samples.*

The two spectra shown in **Figure S4.6** are the $^{27}$Al-NMR spectra obtained for the small-port mordenite (Red) and $HNO_3$ leached mordenite (Blue) samples. The peak at 50 ppm corresponds to the tetrahedral aluminium species, while the peak at 0 ppm corresponds to the octahedral aluminium species. The relative peak areas are 5638 (50 ppm) and 1020 (0 ppm) for the untreated mordenite sample and 5028 (50 ppm) and 833 (0 ppm) for the $HNO_3$ leached mordenite sample. This corresponds to a reduction of 10.8% tetrahedral aluminium and 18.3% octahedral after acid leaching.

***Table S4.2.*** *$N_2$-physisorption data of the small-port mordenite and $HNO_3$ leached mordenite samples obtained after BET analysis.*

| | SP-MOR | $HNO_3$ leached MOR |
|---|---|---|
| BET Surface area ($m^2/g$) | 542.1 | 567.0 |
| Micropore area ($m^2/g$) | 509.6 | 521.2 |
| External surface area ($m^2/g$) | 32.6 | 42.8 |

***Table S4.3.*** *Conversion and isomer ratio of the naphthalene isopropylation reaction catalyzed by small-port and $HNO_3$ leached mordenite.*

| | SP-MOR | $HNO_3$ leached MOR |
|---|---|---|
| Conversion (%) | < 1 | 8 |
| 2,6/2,7 Ratio | N.A. | 4 |

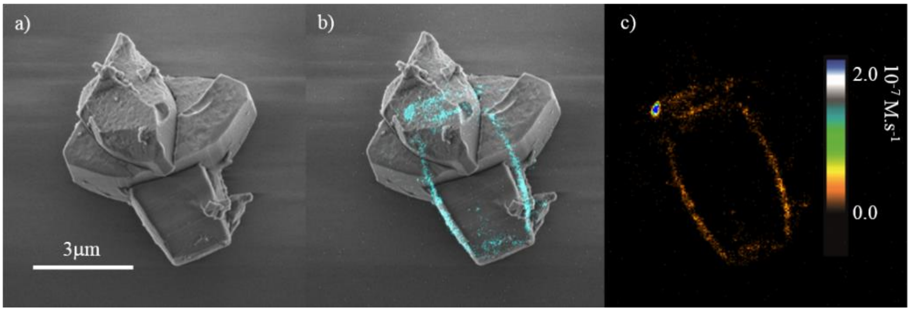

***Figure S4.7.*** *(a) SEM image of an intergrown particle in the SP-MOR batch and (b) the corresponding correlated micrograph. (c) The NASCA image obtained with the original 18wt% FFA in MQ water solution.*

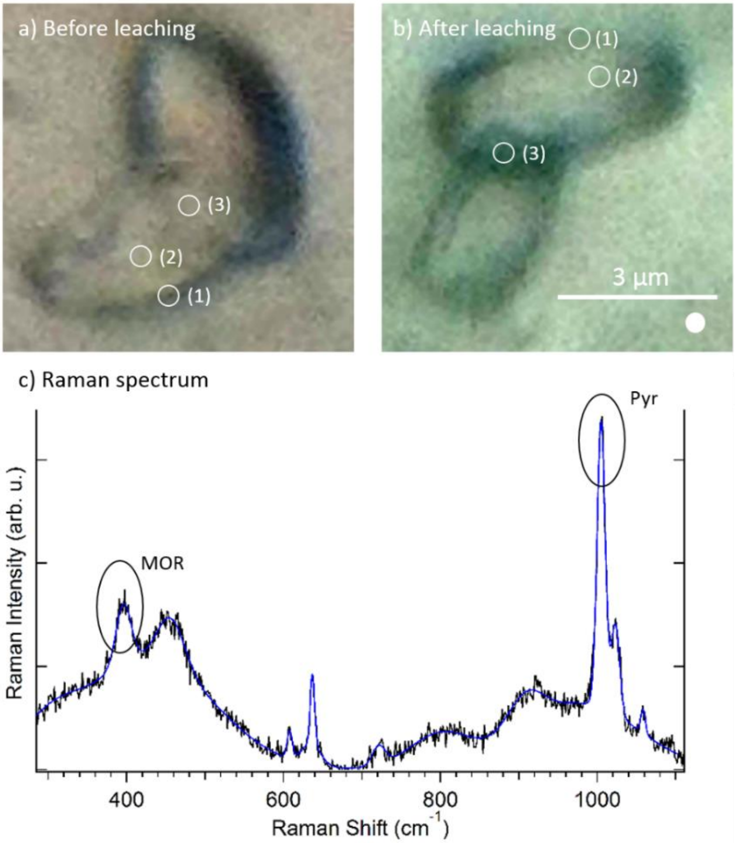

***Figure S4.8.*** *Particles consisting of two intergrown mordenite crystals before (a) and after (b) acid leaching with an indication of the different probed positions; (1) corresponds to the edge and (2) to the center of a flat crystal in the intergrown particle and (3) corresponds to the intergrowth structure of both crystals. (c) The Raman spectrum recorded at the edge of the* $HNO_3$*-leached sample, with the circled peaks showing the respective pyridine and mordenite bands used in analyzing the relative strength of the two signals; i.e. Pyr/MOR ratios in* ***Table S4.4****.*

***Table S4.4.*** *The ratios of the measured pyridine and mordenite Raman signals, derived from spectra recorded at the locations shown in* ***Figure S4.7 a*** *and* ***b****, enabling a quantitative comparison of the relative pyridine uptake in these different areas.*

| | Pyr/MOR ratio | |
|---|---|---|
| | SP-MOR | Leached-MOR |
| Edge (1) | 1.5 | 2.0 |
| Center (2) | 0.3 | 1.4 |
| Intergrowth (3) | 1.6 | 2.4 |

# Annex 1 to Chapter 4

*During the preliminary defense of this PhD manuscript, a reevaluation of the $^{27}$Al-NMR spectra was requested.*

The decreased peak areas in the $^{27}$Al-NMR spectra after acid treatment reveal a preference towards extra-framework $Al^{VI}$ removal. More precisely, the weight averaged peak area related to octahedral Al (0 ppm) decreased 18%, whereas the tetrahedral aluminum content (50 ppm) decreased with 11%. Hence, the ratio of the tetrahedral to octahedral peak area in the untreated sample accounts to 5.5 and increases to 6 after acid leaching. When looking at the raw spectra, however, the decrease of the $Al^{IV}$ peak seems to be most pronounced. Rather than looking at peak intensities the peak area is to be compared and after acid treatment the $Al^{VI}$ peak narrows significantly. This is a known effect that can be attributed to the removal of polymeric extra-framework aluminum species, as this leads to a reduction of quadrupolar line broadening.[1] As a result, the change in peak area is larger.

## References

(1) Engelhardt, G. In *Introduction to Zeolite Science and Practice*; Bekkum, H. Van, Flanigen, E. M., Jansen, J. C., Eds.; Elsevier, 1991.

# Annex 2 to Chapter 4

*During the preliminary defense of this PhD manuscript, a more extensive discussion on the bulk-scale naphthalene isopropylation reaction was requested. More precisely, the relevance of this reaction should be put into perspective and the monoisopropylated product distribution should be assessed.*

Naphthalene dialkylation is industrially performed to obtain precursors to produce polyesters.[1,2] This reaction can result in several isomers of which the 2,7 and 2,6 diisopropylnaphthalene (DIPN) are mostly encountered and the latter is economically most relevant. A great deal of work has therefore been spent to perform this reaction selectively to obtain the correct isomer distribution. This can be achieved by utilizing shape selective zeolite catalysts. In this respect, the characteristic one dimensional porous structure of mordenite zeolites has attracted a lot of interest as the formation of 2,6 DIPN is slightly less sterically hindered compared to the production of 2,7 DIPN.[3–5] However, the application of mordenites to perform this reaction also implies the presence of mass transport limitations due to the bulky nature of these compounds. Dealumination is thus commonly applied to increase reagent and product diffusion, while the shape selectivity should be maintained.

The naphthalene diisopropylation reaction has been investigated on multiple occasions, using different reagents, reaction conditions, catalysts, reactors, etc. The procedure applied in this research is based on the one described by Moreau et al.[6] Thus, naphthalene is reacted with isopropanol in a batch reactor under an increased $N_2$ pressure. (The precise experimental conditions are provided in the experimental section of **Chapter 4**) The results of this reaction are represented in **Table A4.1** and revealed an increased naphthalene conversion from <1% for the untreated sample, to 8% after $HNO_3$ leaching, revealing that acid leaching indeed increases the bulk scale reactivity. However, the limited conversion in the untreated sample renders it impossible to quantitatively compare the shape selective properties of the catalyst with respect to the diisopropylation reaction.

***Table A4.1.*** *Summary of the results obtained from the bulk scale naphthalene isopropylation reaction.*

| Sample | Ref | $HNO_3$ |
|---|---|---|
| Conversion (%) | 0.4 | 7.9 |
| α MIPN (%) | 38 +/- 5 | 21 +/- 0.5 |
| β MIPN (%) | 62 +/- 5 | 70 +/- 0.5 |
| β/α Ratio | 1.6 | 3.3 |
| 2,6 DIPN (%) | 0 | 7 +/- 1 |
| 2,7 DIPN (%) | 0 | 2 +/- 1 |
| 2,6/2,7 Ratio | 0 | 3.5 |

Alternatively, the isomer ratio of β/α monoisopropylnaphthalene (MIPN) was compared to assess the shape selectivity of the sample before and after acid leaching; the formation of α-MIPN is sterically unfavorable compared to β-MIPN.[5] This analysis is similar to comparing the 2,6/2,7 DIPN isomer ratio and, importantly, a sufficient yield of the MIPN isomers is obtained for a quantitative comparison. The β/α ratio is determined to be 1.6 before acid leaching and 3.3 after, revealing that shape selectivity increased after acid leaching. This is in line with our single particle experiments, which show a decreased contribution of catalytic conversions at the H-MOR outer surface after acid leaching.

## References

(1) Chu, S.-J.; Chen, Y.-W. *Appl. Catal. A Gen.* **1995**, *123*, 51–58.

(2) Colon, G.; Ferino, I.; Rombi, E.; Selli, E.; Forni, L.; Magnoux, P.; Guisnet, M. *Appl. Catal. A Gen.* **1998**, *168*, 81--92.

(3) Song, C. *Surf. Chem. Catal.* **2000**, *3* (6), 477–496.

(4) Horsley, J. A.; Fellmann, J. D.; Derouane, E. G.; Freeman, C. M. *J. Catal.* **1994**, *147*, 231–240.

(5) Song, C.; Kirby, S. *Microporous Mater.* **1994**, *2*, 467–476.

(6) Moreau, P.; He, C.; Liu, Z.; Fajula, F. *J. Mol. Catal. A Chem.* **2001**, *168* (1–2), 105–114.

# Chapter 5

## Correlated Super-Resolution Fluorescence and Electron Microscopy Reveals the Catalytic Activity Within Individual ZSM-22 Zeolite Particles

Arunasish Layek,* **Jordi Van Loon**,* Maarten B.J. Roeffaers

Manuscript in preparation

* Joint first authors

Nanocrystalline zeolite particles are applied in a wide range of catalytic reactions. Their size and shape, as well as the distribution of catalytically active sites, significantly vary throughout typical zeolite batches and even within individual particles. This variability leads to a heterogeneous distribution of catalyst performance. Directly investigating the structure-activity relationship at the nanoscale is thus essential for the rational improvement of catalyst materials. In this work, a novel integrated fluorescence and electron microscope is employed to correlatively study the structure and performance of individual ZSM-22 particles. The lateral fusion of multiple elementary nanorods leads to their typical needle-shaped morphology and based on indirect bulk scale experimenting, it has been suggested that this process converts catalytically inactive external Al into catalytically active internal Al. The correlative investigation performed in this research provides direct evidence that this conversion takes place resulting in an inactive zeolite shell of about 30 nm thickness confining the reactivity to the crystal core. Furthermore, nanometer scale catalytic hotspots have been revealed within the catalyst particles and were assumed to result from the presence of structural imperfections that locally increase accessibility into the microporous structure. Linear polarized excitation light experiments further confirmed that catalytic transformations exclusively occurred on acid sites confined within the microporous structure. Clearly, the presented correlative structure-activity investigation provided profound insights about ZSM-22 shape selective properties.

## Contributions

A.L. and J.V.L. contributed equally to this work. Most of the experiments were performed and analyzed by A.L. and J.V.L. J.V.L. is in charge of the ILEM and is responsible for its development. Article writing was done by A.L., J.V.L. and M.B.J.R. All authors were involved in data interpretation.

# Chapter 5 - Correlated super-resolution fluorescence and electron microscopy reveals the catalytic activity within individual ZSM-22 nanorods

## 5.1. Introduction

Zeolites are crystalline microporous aluminosilicates extensively used as heterogeneous catalysts in (petro)chemical and environmental industries.[1-4] Decisive for many applications as catalysts are the acid sites confined within the microporous structure of the zeolite. The number of potential catalytically active acid sites is indicated by the framework Si/Al ratio, as every replacement of a framework Si atom by an Al atom can generate a strong Brønsted acid bridging hydroxyl group. The strength of these Brønsted acid sites depends on the spatial distribution of Al atoms throughout the zeolite crystals. Additionally, the position of the Al atom in the framework is also closely related to acid site accessibility and the confinement of organics inside the microporous structure. The latter can eventually lead to the essential shape selective properties. However, mass transport towards the active sites within catalyst particles is commonly limited due to this tight confinement. This hampers catalyst performance, which is clearly governed by an intricate interplay of multiple factors.[5-7]

ZSM-22 is a high silica zeolite of the TON framework-type consisting of 5-, 6-, and 10-membered ring channels.[5,8] The latter are oriented along the crystallographic c-axis and constitute a unidirectional porous structure inside the ZSM-22 crystals, as only their ca. 0.46 x 0.57 $nm^2$ dimension are sufficiently large to enable considerable mass transport of organic molecules.[9-12] Typically, ZSM-22 particles have been reported to grow as individual rod-like crystals, i.e., the ‘nanorods’, which undergo lateral fusion during the late stages of the synthesis, leading to the typical needle-shaped aggregates (**Figure 5.1**).[13,14] The combination of a one dimensional medium sized pore system and nanometer-scale particle sizes makes it a promising shape-selective acid catalyst in processes such as the dewaxing of petroleum feedstocks,[15,16] (hydro)isomerization of hydrocarbons,[9,17-19] naphtha cracking,[20] methanol to light olefins conversion,[11,21,22] dehydration of glycerol to acrolein,[23] etc.

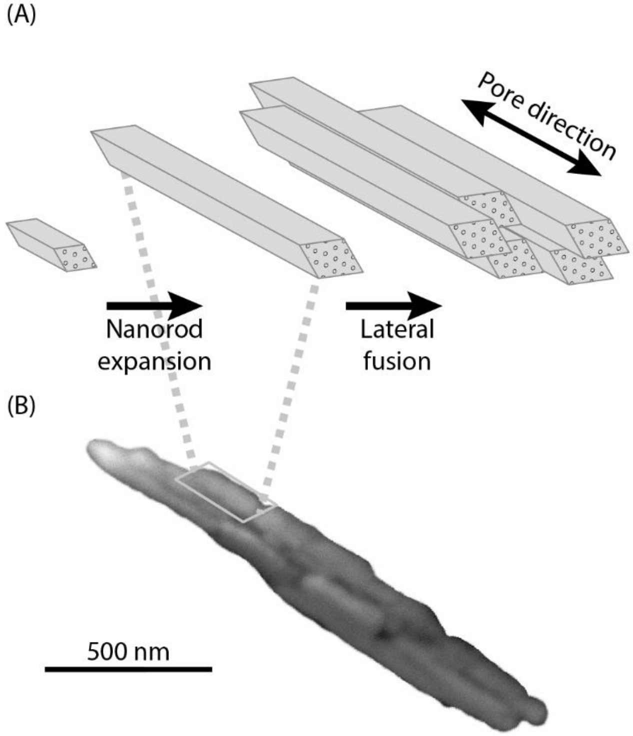

***Figure 5.1.*** *(A) Schematic representation of the three stages that occur during ZSM-22 synthesis; nanorod formation, nanorod expansion and needle formation through lateral nanorod fusion. The direction of the one dimensional porous structure is indicated by the double headed arrow and the crystal faces where the pore openings are located are represented by the dotted planes. (B) A cropped-out SEM image of a typical needle-shaped ZSM-22 particle. Rectangle highlights an individual nanorod that is part of the larger aggregate.*

The growth mechanism of needle-shaped ZSM-22 particles has been described in literature by several groups independently.[13,24,25] Initially, amorphous particles are formed by the coalescence of silica sol grains around which a template (diethanolamine) rich secondary gel precipitates. During synthesis, the silica rich core slowly dissolves while heterogeneous zeolite nucleation takes place at the organophilic surface of the secondary gel. These zeolite crystals are initially silicon rich, but in the later stages of zeolite growth, Al is preferentially incorporated because of an accumulation of aluminate in the mother liquor. As a result, elementary nanorod particles are obtained with an Al enriched outer surface. This is confirmed by combined ICP and XPS.[13,24] Ex situ SEM, TEM and XRD show that in the final stages of ZSM-22 synthesis, these nanorods fuse together laterally and give rise to the larger needle-shaped aggregates. This lateral fusion, observed as a stepwise increase of the particle dimensions, is not correlated to a gain in zeolite yield. It can therefore not be attributed to simple crystal growth. Importantly, this nanorod fusion and increased ZSM-22 particle dimensions lead to a significant increase in catalytic activity which has been attributed to the conversion of inactive external Al into catalytically active internal Al.[13] **Figure 5.1A** schematically represents this growth process.

Thus, individual nanorods with an average diameter of approximately 46 nm, as determined by SEM on 23 different nanorods, are aggregated into needle-shaped crystals and their intergrowths are assumed to be catalytically active. However, the experimental confirmation of this statement is so far only based on indirect evidence, as the intrinsic structural heterogeneity within solid catalytic systems inevitably results in intra- and inter-particle variances in catalytic activity.[26-29] These differences are not straightforwardly revealed using traditional catalyst characterization techniques and exact information on the relationship between catalyst performance and its structure is therefore yet to be obtained. Moreover, the inactive external surface acid sites along with the constrained pore channel system in ZSM-22 would further enhance the shape selectivity by avoiding undesirable reactions. Hence, a quantitative technique to establish a correlation between the catalytic performance and the local nanocrystalline zeolite structure would be desirable. Such a detailed understanding of the structure-activity relationship combined with advanced synthetic and post-synthetic approaches could ultimately lead to an optimized application of ZSM-22 catalysts.

Super-resolution fluorescence microscopy (SRFM) has recently emerged as an effective approach to investigate solid acid catalysts at the single catalyst particle and even single catalytic turnover level.[27,29-31] For example, the technique called nanometer accuracy by stochastic chemical reactions (NASCA) works by adding a specific non-fluorescent fluorogenic reagent to the zeolite sample which is converted into a fluorescent reaction product at the catalytically active sites.[32] By detecting these individual catalytic conversions and localizing their positions with nanometer accuracy, highly precise activity maps of individual catalyst particles can be reconstructed by accumulating the obtained data. One problem that remains, however, is the correlation of these activity maps to the underlying nanoscale structural context that remains unresolved. The latter can be obtained by electron microscopy. For example, scanning electron microscopy (SEM) offers highly resolved structural imaging capabilities to visualize nanoscale structural features and outer particle surfaces. By applying both NASCA and SEM in a combined approach, correlative chemical reactivity mapping and structural imaging of zeolite catalysts would enable a direct visualization of the structure-activity relationship within individual catalysts particles.[33]

In this work, we investigate the catalytic performance of needle-shaped H-ZSM-22 (Si/Al = 75) particles by correlative SRFM and SEM. The highest catalytic activity is revealed in the center of the needle-shaped ZSM-22 particles, whereas the rim of the particles shows significantly less activity.

Moreover, sharp particle tips either show no or very low activity compared to thicker, blunt tips, which are catalytically active. These observations confirm earlier reports based on indirect experiments. Indeed, external Al does not contribute to the catalytic activity as opposed to internal Al. The catalytic activity screening of individual catalyst particles has furthermore revealed nanometer scale catalytic hotspots within the particles. These are attributed to an inhomogeneous active site distribution, owing to a non-uniform and incomplete sideways nanorod fusion which leads to a variation in site accessibility, and an intrinsic Al distribution already present in the nanorods. Additionally, reactivity mapping using linear polarized excitation light confirms that catalytic transformations only take place on active sites located inside the pore channels.

## 5.2. Experimental section

### 5.2.1. Correlative super-resolution fluorescence and scanning electron microscopy

An integrated fluorescence and electron microscope (iFlEM) (**Figure 5.2**) was used to perform the correlative super-resolution fluorescence and scanning electron microscopy experiments. The applied setup is based on the commercially available Secom platform for integrated wide-field fluorescence and electron microscopy, developed by DELMIC B.V., which is built into a FEI Quanta 250 FEG SEM, and has been in-house adjusted to enable super-resolution fluorescence microscopy. The latter was achieved by mounting a 100x 1.4 NA CFI plan APO VC oil immersion objective lens (Nikon) (**Figure 5.2_1**) into the sample stage that is used in combination with 1,3-EMIM acetate as a vacuum compatible immersion liquid. Secondly, an adjustable mount has been integrated into the optical excitation pathway that holds the WF lens. This allows sufficient flexibility for the alignment of the wide field system. The configuration of the microscope implies that both fluorescence excitation and detection are provided from the bottom side up and the SEM is achieved from the top of the sample. Samples are therefore mounted on top of optically transparent cover slides according to the procedure disclosed in the sample preparation section.

Excitation is provided at 532 nm by a diode pump solid state laser (Omicron laserage) and additionally passes through an excitation filter prior to being directed towards the objective lens and the sample by the 442/532 nm dichroic mirror (Chroma) (**Figure 5.2_2**). The transmission of the excitation light into the sample chamber, where the objective lens is located, is enabled by an optically transparent window (**Figure 5.2_3**). The fluorescent signal is captured by the objective lens and passes through the optical chamber window, the dichroic mirror, a 542 nm long pass filter and a 2.5x camera lens, before it is detected using a highly sensitive electron multiplying charge-coupled device (EMCCD) camera (ImagEM Enhanced C9100-23B, Hamamatsu). As such, a 32.8 x 32.8 µm$^2$ field of view is obtained with a 64 x 64 nm$^2$ pixel size. Linear polarized excitation light experiments are enabled by introducing a Glan Thompson polarizer (Thorlabs) on a rotatable mount that has been introduced into the excitation pathway of the iFLEM.

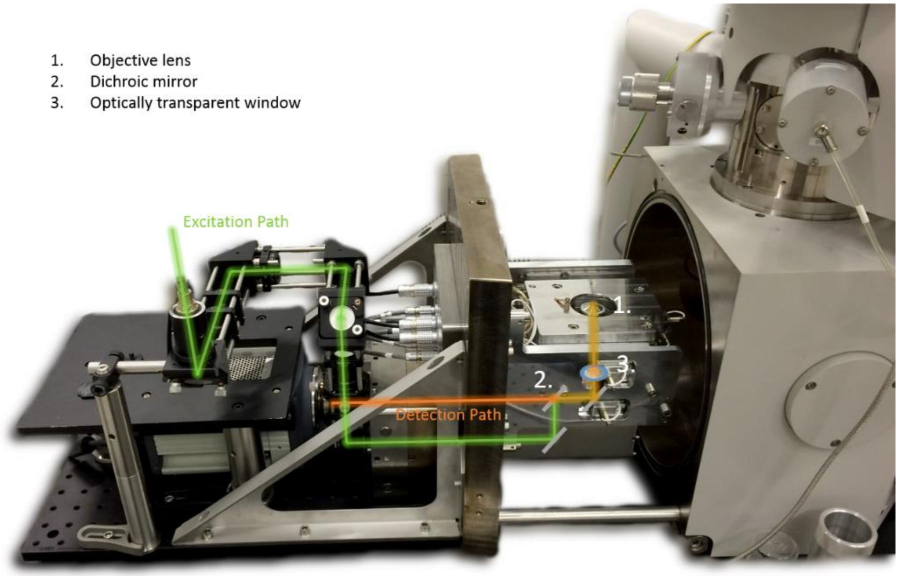

***Figure 5.2.*** *Picture of the iFlEM in the configuration applied for super-resolution fluorescence microscopy (SRFM), i.e. SEM door opened and sample at atmospheric pressure. Both the excitation (green) and detection (orange) paths are depicted, as well as the position of the dichroic mirror (1), the position of the optically transparent window (2) that enables excitation and detection without the need to transfer the sample between dedicated setups, and the objective lens (3). SEM images are obtained under high vacuum conditions prior to SRFM imaging.*

### 5.2.2.Zeolite synthesis

The ZSM-22 sample has been synthesized according to the procedure used by Hayasaka et al.[13]

### 5.2.3.Sample preparation

Single molecule clean ZSM-22 samples (Si/Al = 75) were prepared according to an optimized sample preparation method. Initially, regular glass cover slides (# 1) were calcined in a static air oven at 450 °C for at least 24 h and subsequently ozone treated for 30 min in a UV-reactor (Ultra violet products, PR-100). The ZSM-22 sample is spin-coated onto the cleaned cover slides from a 1 mg / 10 ml ZSM-22 in milli Q water suspension at 2000 rpm for 60 s. Two droplets were added to the cover slide for spin coating. Additionally, the sample containing cover slides were calcined in an oven to remove any organic contaminants from the microporous structure of the zeolite that could lead to fluorescent background. For this purpose, a static air over was used in combination with a specialized heating program in order to prevent any structural changes to the zeolite framework. The sample was heated from room temperature to 80 °C at a rate of 1 °C/min, after which the sample was kept at 80 °C for 1 h. In a second step, the temperature was further increased to 120 °C at 1 °C/min and this temperature was held for 1 h again. In a final heating stage, the temperature was further increased from 120 °C to 450 °C, again with a heating rate of 1 °C/min, and this temperature was maintained for at least 24 h. Afterwards, the sample was cooled down to room temperature and immediately mounted into the iFlEM for investigation.

### 5.2.4.Correlated experiments

All correlative super-resolution fluorescence and scanning electron microscopy experiments were performed at room temperature. After spin coating and subsequent calcination, the sample was mounted on the stage of the iFlEM. Unless stated otherwise, SEM imaging was performed prior to the NASCA experiments throughout the presented research. Therefore, the sample chamber was pumped down to allow SEM imaging (2 kV, SE, high vacuum mode), which was applied to locate a suitable region of interest and to perform detailed structural imaging of the contained samples. Afterwards, the SEM chamber was brought back to atmospheric pressure. This allowed us to perform the cathodoluminescent grid scan that was part of the quantitative overlay procedure (further described in the overlay section) and to perform the NASCA imaging. The latter was performed after attaching a perfusion chamber (PC8R-1.0-CoverWell, Grace Bio labs) onto the sample and after a waiting time of approximately 15 min needed to eliminate mechanical drift that could be present after bringing the sample back to atmospheric pressure. 50 µL of a 10 vol. % furfuryl alcohol (FFA) (Sigma Aldrich, 98%, purified through vacuum distillation prior to use) in milli Q water was added to the perfusion chamber, which acted as a reactor cell. This reagent concentration has been established as being optimal through several experiments that were conducted using various reagent concentrations. By adding the FFA reagent, fluorescent oligomers are formed on the catalytically active sites which are excited with 3.5 kW/cm$^2$ laser power at 532 nm, and detected using 30 ms exposure time and 297 electron multiplying gain. The reaction scheme for the FFA oligomerization reaction that leads to the fluorescent reaction products is described elsewhere.[30]

### 5.2.5.Data analysis

During all experiments performed in this research, 10.000 frame movies are acquired. One exception was made for the experiment performed using linear polarized excitation light perpendicular to the one dimensional porous structure that led to **Figure 5.4B**. This image is the result of a 1.000 frame movie due to the clear absence of catalytic turnovers. These are analyzed using the Localizer software for Igor Pro (Wavemetrics). The localization of individual catalytic turnovers is achieved by fitting a 2D Gaussian function to their point spread function. This approach yields the positions of the fluorescent catalytic reaction products with up to 20 nm resolution.[32] By depicting the locations of the turnovers within 20 x 20 nm$^2$ bins, a quantitative catalytic activity map is obtained. The quantitative catalytic activity maps that are described in the current research have undergone an additional consolidation procedure in order to remove reappearing fluorescent events (100 ms of blinking time is maximally allowed and a distance of maximally 50 nm). The parameters used for the analysis of the sample were determined by a careful assessment of a series of different parameters. On the quantitative activity maps that are displayed in the main article, the color bar indicates the chemical reactivity. This is obtained by considering the number of turnovers within the 20 x 20 nm$^2$ bins in combination with the average thickness of the needle-shaped particles. The latter is assumed to be 160 nm, based on their geometry, which implies that the height of the particles is similar to the width of the particles. These dimensions result in the voxel volume. By additionally using the Avogadro number, the mol of product that is formed within every voxel and per time unit can be determined.

### 5.2.6.Overlay procedure

The quantitative activity maps and SEM micrographs are quantitatively correlated by an in-house developed approach based on cathodoluminescence (CL) (**Appendix 1**). After performing the SEM imaging, the electron beam is used to generate optical reference signals by means of CL. A grid is projected onto the class cover slide by the electron beam in spot mode and the corresponding positions are precisely localized based on these diffraction limited CL spots in the optical image using localization software. The determined optical positions are subsequently correlated to their corresponding position in SEM, which are accurately known as they have been used as input for the grid projection. This approach enables an accurate determination of the translation, rotation and magnification parameters between both imaging modalities. The software needed to perform the grid scan is provided as a Micromanager script and the application that has been developed to perform the actual overlay is provided as a Matlab procedure, both are publicly available at “https://github.com/KrisJanssen/QuickCLEM”.

## 5.3. Results and discussion

The experiments described in this work are performed on an in-house built integrated fluorescence and electron microscope (iFLEM), which is described in detail in the Supporting Information (**Figure 5.2**). Importantly, this set-up was used in a correlative fashion, i.e., initially SEM is performed under high vacuum conditions and afterwards the system is brought to atmospheric pressure prior to the addition of the fluorogenic furfuryl alcohol (FFA) reagent solution used to perform the catalytic activity mapping on the same H-ZSM-

22 crystals. This approach was used to investigate over 20 individual needle-shaped ZSM-22 particles. In **Figure 5.3A-D** the experimental results of four representative crystals are shown. The catalytic activity maps are built up by simply counting individual reaction turnovers in projected areas of 20 × 20 nm$^2$ during a 300 second experiment. The color scale indicates the local reactivity within these areas. A detailed procedure describing the conversion of single turnover numbers into catalytic reactivity is provided in the supporting information. In **Figure 5.3E-H** the corresponding scanning electron micrographs are shown, which are furthermore accurately overlaid with the catalytic activity maps into correlative micrographs, as displayed in **Figure 5.3I-L**. A detailed description of this procedure is also provided in the supporting information.

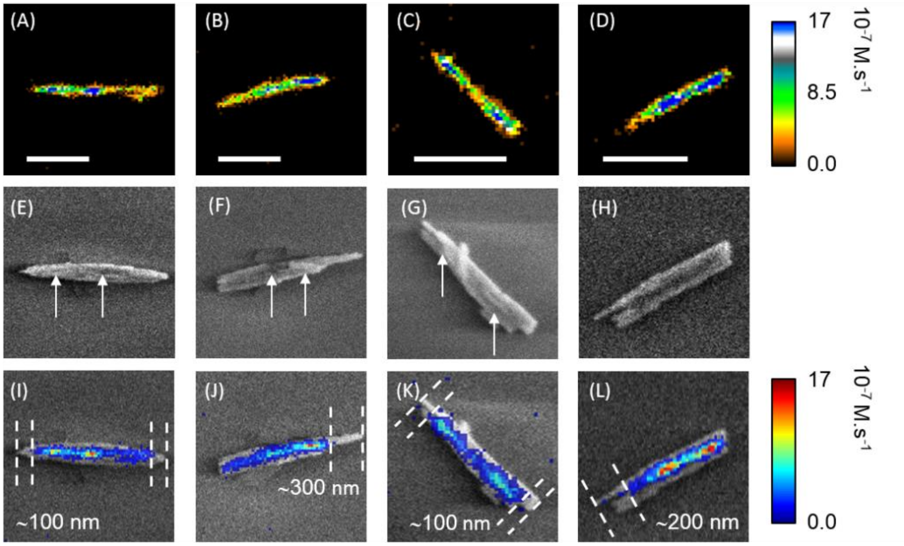

***Figure 5.3**. (A-D) Quantitative catalytic activity maps of four representative ZSM-22 crystals. The color bar indicates the reactivity within the individual bins. (E-H) The respective SEM images of the four ZSM-22 crystallites and (I-L) the correlative micrographs including an alternative color scale that qualitatively represents the activity distribution. Dashed lines indicate the absence of catalytic activity in the tip zones of some crystals. Structural features that correspond to catalytic hotspots are additionally indicated by the white arrows. (Scale bars = 500 nm)*

The correlative micrographs reveal that the catalytic activity is heterogeneously distributed along the long axis of the needle-shaped particles, with at least one zone per particle showing an increased catalytic activity; these zones will be further referred to as catalytic hotspots. These hotspots do not seem to be directly related to any structural feature observed in SEM. However, when taking a closer look at the correlated micrograph in **Figure 5.3J**, a catalytic hotspot can be associated to an intergrown nanorod on top of the needle-shaped ZSM-22 particle. When now looking at the other correlative micrographs, some of the catalytic hotspots can also be related to structural imperfections; see white arrows in the SEM images (**Figure 5.3E-H**).

Also in the lateral direction of the needle-shaped particles, the catalytic activity seems to be irregular. In general, the catalytic activity is low along the edges and reaches a maximum in the middle of the particle. Moreover, when comparing the width of the catalytic activity maps with the actual particle width obtained through SEM, a general discrepancy is observed. For instance, the needle-shaped particle illustrated in **Figure 5.3E** has a physical width of approximately 160 nm, whereas the catalytic activity map is only approximately 110 nm wide. This reveals a catalytically inactive zone of roughly 30 nm on both sides of ZSM-22 particles. Note that also the external surface itself is found to be catalytically inactive. Additionally, a similar zone of inactivity is observed at the tips of the needle-shaped ZSM-22 particles, i.e.*,* less activity is observed on the tips compared to the bulk of the particle. The dashed lines in **Figure 5.3I-L** indicate these catalytically inactive areas. Nevertheless, it is clear from **Figure 5.3J** and **L** that two distinct behaviors are noticeable. On the one hand, no catalytic activity is observed on the sharp tip, while blunt particle tips are catalytically active.

The observations described above support the growth mechanism of needle-shaped H-ZSM-22 catalyst particles as proposed in literature (*vide supra*).[13] More precisely, as lateral nanorod fusion is hypothesized to transforms the catalytically inactive external Al into catalytically active internal Al, a zone of inactivity at the edges of the needle-shaped crystals is to be expected. Moreover, the catalytic activity maps are a 2D projection of a 3D object, which is thicker in the center compared to the edges. Hence, more aluminium is present internally and this results in the increased activity at the center of the particles. The edges of the needle-shaped particles are generally composed of only one nanorod (diameter ~ 30 nm), which is in agreement with the HR-TEM observations (**Figure S5.1A**), and can consequently be considered as being composed of catalytically inactive external Al sites. The same rationale can also explain why sharp tips at the outer ends of the needle-shaped ZSM-22 particles do no show significant catalytic activity, as opposed to blunt tips. Sharp tips are composed of individual nanorods which are only fused together close to one end along their longest dimension. Hence, the amount of catalytically active Al resulting from this fusion is limited and is only located at the end closest to the bulk of the particle. This is not the case for blunt particle ends, in which several nanorods are most likely fused together parallelly, resulting in much more internal Al along their full length.

The origin of the catalytic hotspots is less clear from the performed experiments. Based on the correlation of catalyst activity to the structural details, the hotspots seem to be related to crystal imperfections and these might lead to improved accessibility. Al sites can only optimally fulfill their catalytic role if both reagent and product molecules can easily diffuse through the micropores where the active sites are located. In case of the ZSM-22 framework, only the 10 membered ring channels are of the right size to allow sufficient mass transport for catalysis purposes. This limits diffusion through the micropores, possibly hampering catalytic activity. However, an imperfect fusion between the elementary nanorods could leave a gap in the catalyst structure and decrease the average distance between the micropore entrances and the active sites. Thus, increasing mass transport. A similar explanation holds for the nanorod fused on top of the needle-shaped particle in **Figure 5.3J**. An incomplete fusion with the underlying particle might lead to additional openings into the catalyst structure, making the internal Al more accessible. It must be noted, however, that this is one possible explanation and further research is needed to ensure that structural imperfections are indeed inducing the catalytic hotspots. Additionally, not all catalytic hotspots in the investigated ZSM-22 particles can be related to specific structural features. On the one hand, this could be explained by structural features that remain unresolved using the presented approach, but also a heterogeneous Al distribution that was already present within the elementary nanorods, prior to nanorod fusion, could lead to this observation. Clearly, an improved structural resolution would be prerequisite for further elucidation of the revealed activity distribution and its relation to catalyst structure.

Importantly, previous research has demonstrated that prolonged electron beam exposure can induce chemical and structural changes to zeolites and molecular sieve catalysts.[34-36] Logically, such electron beam induced amorphisation would impact the catalytic activity and seems to be most precarious in small, nanometer sized zeolite particles. In this regard, the sample under investigation and, more specifically, the outer edges and the sharp particle tips, appear particularly prone to electron beam damage as these are the narrowest structural features. This is confirmed by an additional experiment in which several ZSM-22 particles are exposed to at least 5-fold more intense electron beam irradiation (Half FOV scanned in 2 min, 5 keV acceleration voltage, 0.19 nA) and one particle within the same field of view is only irradiated using the mild imaging conditions used throughout this work (Full FOV scanned once in 1.4 min, 2 keV acceleration voltage, 0.10 nA). The result of this experiment is shown in **Figure S5.2** and reveals that the catalyst particles become catalytically inactive after intense electron beam irradiation, as the mildly irradiated catalyst particle still shows activity.

Clearly, the effect of the SEM imaging conditions applied during the presented research on the sample integrity needs to be carefully considered. In order to double check the previously discussed results obtained with the mild electron doses, the correlated experiments were performed in a reversed sequence, i.e. the SEM image is acquired after performing the chemical activity mapping (**Figure S5.3**). Performing the experiments in a reversed order is, however, not the method of choice, as the removal of the liquid after the catalytic activity measurements enhances the risk of unwanted sample movement; small shifts hamper correct image correlation. Further, after removal of the liquid a residual film might remain on the sample that reduces the amount of detail that can be resolved in the SEM images (**Figure S5.3F** and **G**). The results of four validation experiments that were performed reveal a similar reactivity distribution compared to the previous experiments using the initial experimental approach (**Figure 5.3**). Hence, these results demonstrate that the electron beam effect, at least under the mild SEM imaging conditions used in this work (2 keV and 0.15 nA), on the chemical reactivity in the described ZSM-22 investigation is negligible. Using such milder imaging conditions additionally reduces sample charging, which is required as the sample is mounted on insulating glass cover slides.

To further confirm the importance of nanorod fusion in generating catalytically active crystal domains, the molecular confinement of the observed catalytic reaction products to the one-dimensional pore network of ZSM-22 was evaluated. Specifically for ZSM-22, the presence of acid sites at the exterior zeolite surface would have a negative impact in various processes. In n-alkane hydroisomerization, for example, this would deteriorate catalyst shape selectivity.[37,38] The molecular confinement of the individual fluorescent reaction products with respect to the ZSM-22 crystals and the underlying pore structure was investigated using linear polarized excitation light. Note that the fluorescent FFA oligomers will only be efficiently excited when its dipole moment is oriented parallel to the polarization of the excitation light. The dimensions of the FFA oligomers are such that their long axis needs to be aligned along the 10MR pores. The results of such a linear polarized excitation light experiment on a representative ZSM-22 particle are shown in **Figure 5.4**.

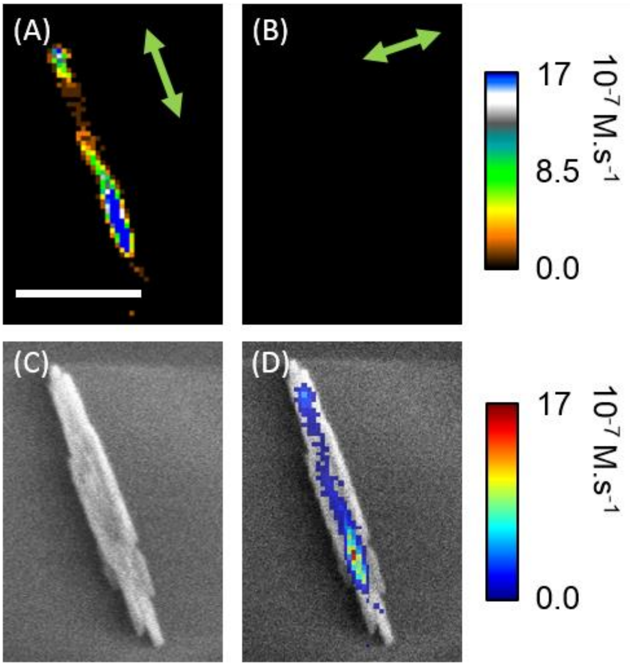

***Figure 5.4**. (A) Catalytic activity map obtained with linear polarized excitation light along and (B) perpendicular to the one dimensional porous structure in a needle-shaped ZSM-22 particle. The green double headed arrows indicate the respective light polarization direction and the color scale represents the reactivity within the individual bins. (C) The corresponding SEM image of the particle under investigation and (D) the correlative micrograph in combination with a color scale that qualitatively indicates reactivity differences in the different areas of the catalyst particle. (Scale bar = 500 nm).*

When mapping the catalytic activity distribution using linear polarized excitation light along the 10MR pores (**Figure 5.4A**), a similar reactivity is observed as when using circular polarized excitation light (**Figure 5.3**). In both cases a heterogeneous activity profile is revealed along the long axis of the particle and the edges and sharp tips of the particle are completely inactive. The activity map obtained after changing the polarization direction with 90 degrees (**Figure 5.4B**) results in a complete disappearance of the fluorescence signal. This shows that all fluorescent product molecules are confined to the microporous structure. Based on the results shown in **Figure 5.3** and **5.4**, the overall activity of ZSM-22 particles can be schematically represented as in **Figure 5.5**. Hence, it is demonstrated beyond doubt that catalytic transformations of furfuryl alcohol exclusively occur on acid sites contained inside the microporous structure, leading to the highly shape-selective properties.

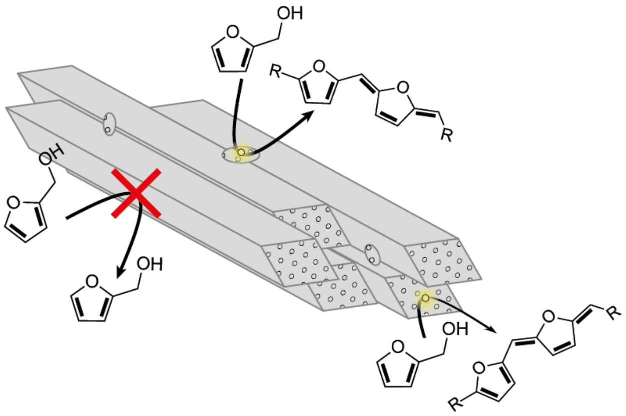

***Figure 5.5.*** *Schematic representation of the catalytic activity distribution of needle-shaped ZSM-22 crystals. Internal aluminium results in catalytically active acid sites that are located within the microporous structure. These active sites are accessible through the pore entrances (dotted pattern) that are present on the tips of the individual nanorods, or at crystallographic defects that originate from imperfect lateral nanorod fusion. Framework aluminium at the external surface are catalytically inactive.*

## 5.4. Conclusion

Correlative super-resolution fluorescence and scanning electron microscopy has been used to investigate the catalytic activity of individual ZSM-22 catalyst particles. This has, for the first time, directly revealed that catalytic activity is confined to the inner parts of needle-shaped ZSM-22 crystals where the catalytically inactive external Al, present at the outer edges of the primary nanorods, is converted into catalytically active internal Al. As a result, the outer shell of the crystals, with a thickness of about 30 nm, is catalytically inactive. This further adds to the shape selectivity imposed by the 10MR pore dimensions, by avoiding undesirable product formation at the external surface of the zeolite particles. Additionally, catalytic hotspots are prominently present in each crystal. Based on the correlated SEM images these could be assigned to crystal defects such as mismatching during lateral nanorod fusion. However, variations in Al distribution at these scales cannot be ruled out due to a lack of sufficiently accurate experimental methods. The confinement of the catalytic process to the 10MR micropores could further be confirmed from the linear polarized excitation experiments. These support that catalytic activity is confined to Al sites present within the internal surface of the microporous structure. Future efforts should focus on investigating the precise interplay between structural imperfections and improved catalytic activity. For example, the development of tools that combine HR-SEM or –TEM[39] with NASCA microscopy would enable such research.

## 5.5. References

(1) Mizuno, N.; Misono, M. *Chem. Rev.* **1998**, *98*, 199-218.

(2) Weitkamp, J. *Solid State Ionics* **2000**, *131*, 175–188.

(3) Corma, A. *J. Catal.* **2003**, *216*, 298-312.

(4) Bhan, A.; Iglesia, E. *Acc. Chem. Res.* **2008**, *41*, 559-567.

(5) Baerlocher, C.; McCusker, L. B.; Olson, D. H. *Atlas of Zeolite Framework Types*; Sixth ed.; Elsevier, 2007.

(6) Danilina, N.; Krumeich, F.; Castelanelli, S. A.; van Bokhoven, J. A. *J. Phys. Chem. C* **2010**, *114*, 6640-6645.

(7) Dědeček, J.; Sobalík, Z.; Wichterlová, B. *Catal. Rev.* **2012**, *54*, 135-223.

(8) Kokotailo, G. T.; Schlenker, J. L.; Dwyer, F. G.; Valyocsik, E. W. *Zeolites* **1985**, *5*, 349-351.

(9) Kumar, R.; Ratnasamy, P. *J. Catal.* **1989**, *116*, 440-448.

(10) Teketel, S.; Skistad, W.; Benard, S.; Olsbye, U.; Lillerud, K. P.; Beato, P.; Svelle, S. *ACS Catal.* **2012**, *2*, 26-37.

(11) Cui, Z.; Liu, Q.; Ma, Z.; Bian, S.; Song, W. *J. Catal.* **2008**, *258*, 83-86.

(12) Verboekend, D.; Thomas, K.; Milina, M.; Mitchell, S.; Pérez-Ramírez, J.; Gilson, J.-P. *Catal. Sci. Technol.* **2011**, *1*, 1331-1335.

(13) Hayasaka, K.; Liang, D.; Huybrechts, W.; De Waele, B. R.; Houthoofd, K. J.; Eloy, P.; Gaigneaux, E. M.; van Tendeloo, G.; Thybaut, J. W.; Marin, G. B.; Denayer, J. F.; Baron, G. V.; Jacobs, P. A.; Kirschhock, C. E.; Martens, J. A. *Chem. -Eur. J.* **2007**, *13*, 10070-10077.

(14) Verboekend, D.; Chabaneix, A. M.; Thomas, K.; Gilson, J.-P.; Pérez-Ramírez, J. *Cryst. Eng. Comm* **2011**, *13*, 3408-3416.

(15) Chester, A. W.; Garwood, W. E.; Vartuli, J. C. Google Patents, 1986.

(16) Chen, N. Y.; Garwood, W. E. Google Patents, 1988.

(17) Martens, J. A.; Verboekend, D.; Thomas, K.; Vanbutsele, G.; Gilson, J. P.; Perez-Ramirez, J. *ChemSusChem* **2013**, *6*, 421-425.

(18) Maesen, T. L. M.; Schenk, M.; Vlugt, T. J. H.; Jonge, J. P. d.; Smit, B. *J. Catal.* **1999**, *188*, 403-412.

(19) Martens, J. A.; Souverijns, W.; Verrelst, W. i. m.; Parton, R.; Froment, G. F.; Jacobs, P. A.

(20) Jamil, A. K.; Muraza, O.; Sanhoob, M.; Tago, T.; Konno, H.; Nakasaka, Y.; Masuda, T. *J. Anal. Appl. Pyrolysis* **2014**, *110*, 338-345.

(21) Jamil, A. K.; Muraza, O.; Yoshioka, M.; Al-Amer, A. M.; Yamani, Z. H.; Yokoi, T. *Ind. Eng. Chem. Res.* **2014**, *53*, 19498-19505.

(22) Teketel, S.; Svelle, S.; Lillerud, K.-P.; Olsbye, U. *ChemCatChem* **2009**, *1*, 78-81.

(23) Hoang, T. Q.; Zhu, X.; Danuthai, T.; Lobban, L. L.; Resasco, D. E.; Mallinson, R. G. *Energy & Fuels* **2010**, *24*, 3804-3809.

(24) Luo, Y.; Wang, Z.; Jin, S.; Zhang, B.; Sun, H.; Yuan, X.; Yang, W. *CrystEngComm* **2016**, *18* (1), 5611–5615.

(25) Di Renzo, F.; Des Courrieres, T.; Massiani, P.; Fajula, F.; Figueras, F. *Zeolites* **1991**, *11*, 539–548.

(26) Cejka, J.; Corma, A.; Zones, S. *Zeolites and catalysis: synthesis, reactions and applications*; Wiley-VCH, Weinheim, 2010.

(27) Weckhuysen, B. M. *Angew. Chem. Int. Ed.* **2009**, *48*, 4910-4943.

(28) Buurmans, I. L.; Weckhuysen, B. M. Heterogeneities of individual catalyst particles in space and time as monitored by spectroscopy. *Nat. Chem.* **2012**, *4*, 873-886.

(29) Janssen, K. P.; De Cremer, G.; Neely, R. K.; Kubarev, A. V.; Van Loon, J.; Martens, J. A.; De Vos, D. E.; Roeffaers, M. B.; Hofkens, J. *Chem. Soc. Rev.* **2014**, *43*, 990-1006.

(30) Roeffaers, M. B.; De Cremer, G.; Uji-i, H.; Muls, B.; Sels, B. F.; Jacobs, P. A.; De Schryver, F. C.; De Vos, D. E.; Hofkens, J. *Proc. Natl. Acad. Sci.* **2007**, *104*, 12603-12609.
(31) Xu, W.; Kong, J. S.; Yeh, Y. T.; Chen, P. *Nat. Mater.* **2008**, *7*, 992-996.
(32) Roeffaers, M. B.; De Cremer, G.; Libeert, J.; Ameloot, R.; Dedecker, P.; Bons, A. J.; Buckins, M.; Martens, J. A.; Sels, B. F.; De Vos, D. E.; Hofkens, J. *Angew. Chem. Int. Ed.* **2009**, *48*, 9285-9289.
(33) Zhou, X.; Andoy, N. M.; Liu, G.; Choudhary, E.; Han, K. S.; Shen, H.; Chen, P. *Nat. Nanotechnol.* **2012**, *7*, 237-241.
(34) Bursill, L. A.; Thomas, J. M.; Rao, K. J. *Nature* **1981**, *289*, 157 - 158.
(35) Hirsch, E. H. *Nature* **1981**, *293*, 759.
(36) Aydin, C.; Lu, J.; Liang, A. J.; Chen, C. Y.; Browning, N. D.; Gates, B. C. *Nano Lett.* **2011**, *11*, 5537-5541.
(37) Chen, N.; Wang, N.; Ren, Y.; Tominaga, H.; Qian, E. W. *J. Catal.* **2017**, *345*, 124-134.
(38) J.A. Martens, G. V.; P.A. Jacobs; J. Denayer; R. Ocakoglu; G. Baron; J.A. Muñoz Arroyo; J. Thybaut; Marin, G. B. *Catal. Today* **2001**, *65*, 111-116.
(39) Karreman, M. A.; Buurmans, I. L.; Agronskaia, A. V.; Geus, J. W.; Gerritsen, H. C.; Weckhuysen, B. M. *Chem. -Eur. J.* **2013**, *19*, 3846-3859.

## 5.6. Supporting information

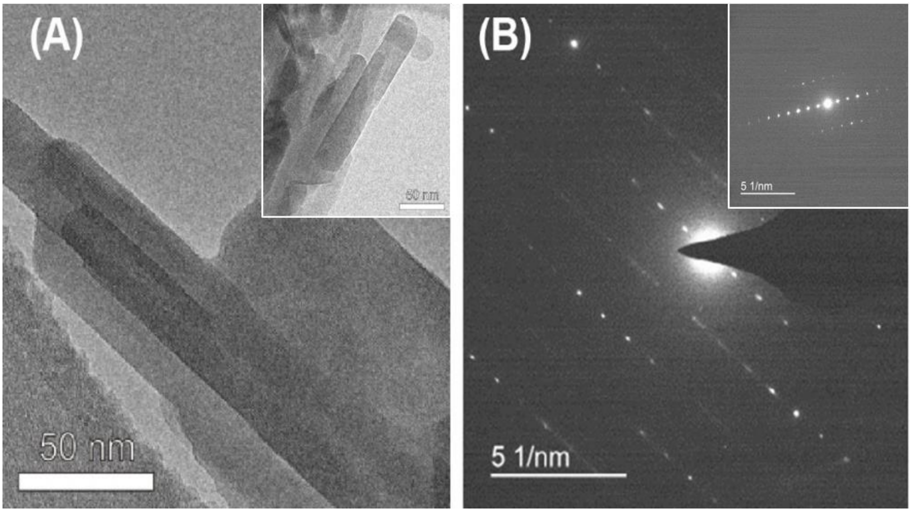

***Figure S5.1.*** *(A) HR-TEM image of needle-shaped ZSM-22 particles and their elementary nanorods. (B) The electron diffraction pattern of the needle-shaped particle in subimage (A), illustrating its high crystallinity. The insert shows the electron diffraction pattern of the individual nanorod represented in the inset in subimage (A) and also reveals high crystallinity.*

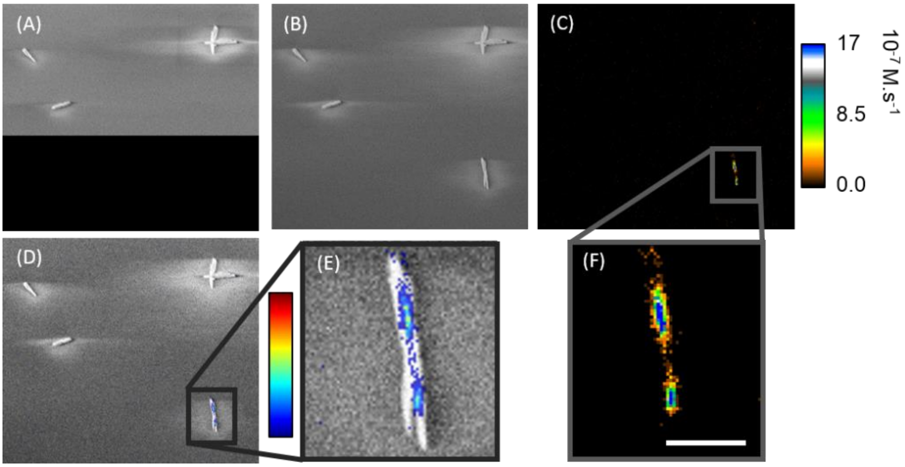

***Figure S5.2.*** *(A) SEM image of the intensely irradiated area containing three ZSM-22 particles (SEM imaging conditions: FOV scanned halfway in 2 min, 5 keV acceleration voltage, 0.19 nA). (B) SEM image of the full field of view (FOV), acquired with the imaging conditions used throughout the experiments (FOV fully scanned in 1.4 min, 2 keV acceleration voltage, 0.10 nA), revealing an additional ZSM-22 particle that was not intensely irradiated. (C) Quantitative activity map and (D) the correlative micrograph obtained for the complete FOV; only the particle at the bottom right in the FOV shows catalytic activity. (E), (F) enlargements of the correlative micrograph and quantitative activity map respectively. (Scale bar = 500 nm).*

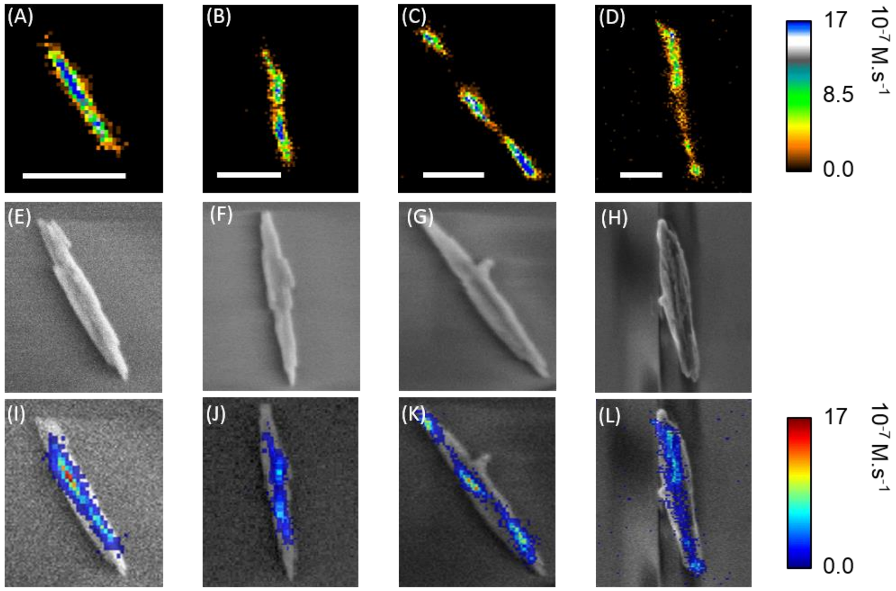

***Figure S5.3.*** *The resulting images of correlative experiments performed in a reversed order compared to the results shown in the main article, i.e. catalytic activity mapping is performed prior to SEM imaging. (A-D) Catalytic activity maps, (E-H) corresponding SEM images and (I-L) resulting correlative micrographs. The SEM images represented in F and G reveal a possible drawback of performing the experiments in the reversed order. A film has deposited on top of the samples due to the removal of the reagent solution after activity mapping. This reduces the obtained resolution, leaving more structural features undetected. (Scale bars = 500 nm).*

# Chapter 6

## Conclusion and Perspectives

.

# Chapter 6 – Conclusion and Perspectives

Recently, there have been increased efforts to investigate the structure-activity relationship in heterogeneous catalyst samples using correlative light and electron microscopy (CLEM). By consecutively performing super-resolution fluorescence microscopy (SRFM) and scanning electron microscopy (SEM), nanoscale catalytic activity maps could be linked to local structural details. As described in **Chapter 1**, this state-of-the-art research has so far uncovered large variations in (photo)catalytic activity and reagent adsorption, which could be related to the intrinsically complex catalyst structure. Such insights remain hidden in traditional ensemble averaged experimentation. However, correlative SRFM and EM studies have thus far exclusively been performed using dedicated microscopes, requiring delicate sample transfer. Furthermore, despite the numerous successful applications of SRFM to investigate zeolite catalyst performance at the nanoscale, correlative SRFM and SEM has not yet been explored in this field. Correlative attempts have been limited to one study of FCC catalyst particles using an integrated light and electron microscope (ILEM) that combines diffraction limited confocal laser scanning microscopy (CLSM) and transmission electron microscopy (TEM). Such an ILEM decreases sampling time and facilitates image overlay, but simultaneous structural imaging and super-resolved catalytic activity mapping is rendered impossible due to the required configuration of the applied TEM based approach.

The goal of my PhD was to investigate the catalyst structure-activity relationship by developing an ILEM and accompanying assays to enable simultaneous SRFM and SEM. For this purpose, a commercial SEM based ILEM was acquired and further developed in-house to allow super-resolved catalytic activity mapping by recording single fluorescent reaction products. Throughout the project, this device has been applied to study increasingly complex systems. This allowed its gradual improvement by resolving the encountered technical issues. Initially, the possibility of investigating silver photodeposition on ZnO crystals was assessed under *in situ* conditions. As a follow-up, the ILEM was applied correlatively to allow a quantitative study of the photocatalytic silver deposition on different ZnO structures. The gained insights led to first of their kind correlative SRFM and SEM investigations on zeolite catalysts. These demonstrated the importance of intercrystalline intergrowth structures on the overall catalyst performance in a SP-MOR batch, and the impact of lateral nanorod fusion on ZSM-22 catalyst shape-selectivity could be directly studied.

The ILEM configuration allows simultaneous UV irradiation and SEM imaging at the same region of interest (ROI). Hence, as is reported in **Chapter 2**, its initial application led to a real-time visualization of silver co-catalyst photodeposition on ZnO crystals. This research demonstrated that silver nanoparticle formation predominantly occurs at crystal edges. However, regardless of this successful nanoscale structure-activity investigation under realistic conditions, the electron beam contribution to the silver deposition was found to be non-negligible. A quantitative *in situ* study therefore required an optimization of the experimental conditions, or, alternatively, the electron beam impact could be avoided by applying the ILEM correlatively. Such a correlative approach was applied in **Chapter 3** and involved nanoscale structural imaging of the photocatalyst before and after UV induced silver photodeposition. This study revealed a heterogeneously distributed photoreduction activity for commonly encountered ZnO photocatalysts. More precisely, on dumbbell-shaped particles about half of the Ag deposits were located at the crystallographic edges of the O-terminated $(000\bar{1})$ polar planes and the other half at the O-terminated facets of structural imperfections. Upon subjecting seemingly defect-free ZnO microrods to such tests, edges of O-terminated polar planes outlined with $\{10\bar{1}\bar{1}\}$ facets were found to be most active towards Ag photodeposition. A discrepancy is noticed when comparing these results with earlier indirect bulk scale experiments. This illustrates the necessity to directly visualize the photocatalyst structure-activity relationship at the sub-particle level to capture the contribution of structural imperfections.

Several technical advances were needed to enable these real-time and consecutive photocatalyst structure-activity investigations. A procedure was established to align the fields of view of the optical and electron microscope. This is at the base of the ILEM approach, as it facilitates ROI retrieval, and in this application allowed UV-irradiation at the area that is observed by SEM. Nevertheless, an *in situ* investigation of Ag photodeposition was only possible by the development of a liquid cell, as deposition occurs from a liquid phase reagent. The liquid cell consisted of an electron transparent $Si_3N_4$ window at the top and an optically transparent cover slide at the bottom. The 50 nm thickness of the electron transparent window makes it susceptible to rupturing. Hence, procedures were developed for liquid cell assembly that prevented an uneven force distribution, sudden pressure increases and too dense sample mounting. Also, a responsive sample and objective movement was required, which was initially hampered by the use of a viscous vacuum compatible immersion oil. This was resolved by exploring the possibility of using an ionic liquid based vacuum compatible immersion medium. However, the intrinsic electron beam induced Ag deposition remained an issue when using the liquid cell. A correlative approach was therefore developed that allowed bringing the SEM chamber to atmospheric pressure in between structural imaging, to perform Ag photodeposition.

The first nanoscale zeolite catalyst structure-activity investigation was ultimately achieved after an upgrade of the ILEM stage to ensure sufficient stage stability for accurate single turnover based activity mapping. A correlative approach, in combination with the attained technical developments, allowed structural imaging prior to venting the SEM and adding the fluorogenic reagent for catalytic activity mapping. In **Chapter 4** it is described how such research directly revealed the role of commonly encountered intercrystalline intergrowths in small-port MOR aggregates on the overall catalytic performance. The introduction of reaction-pore confinement plots revealed that reaction products at the defect-rich intergrowth boundary mainly result from active sites located within the microporous structure, identifying the intergrowth structure as a void space that allows unrestricted mass transport towards the intrinsic microporous structure. Dealumination by acid leaching did not change this situation and merely increased activity on previously active intergrowths and crystallite edges. Even the removal of 30% of framework aluminium, which was demonstrated by means of static pyridine adsorption experiments to lead to a transition of small-port to large-port H-MOR, did not alter the spaciousness of the reactivity pattern and the local reaction-pore confinement. These results demonstrate the relevance of dynamic catalyst testing at the single particle level and indicate the importance of intercrystalline intergrowths for the overall catalyst performance.

**Chapter 5** reports on the correlative nanoscale structure-activity investigation of individual ZSM-22 catalyst particles. These typically needle shaped catalyst crystals result from a lateral fusion of elementary nanorods. Direct evidence has been provided that during this lateral fusion, external, catalytically inactive, aluminium is converted into catalytically active internal aluminium. Hence, reactions are mainly catalyzed by active sites contained within the shape selective microporous structure, avoiding undesirable product formation at the external catalyst surface. The prominent presence of catalytic hotspots could furthermore be assigned to crystallographic mismatching during lateral nanorod fusion, which leads to higher accessibility into the microporous structure while maintaining shape selectivity.

Over the course of my PhD, a performant ILEM was developed with accompanying assays to explore the structure-activity relationship of heterogeneous catalysts at the nanoscale. This enabled both consecutive and real-time investigations of ZnO photocatalysts and the first correlative structure-activity studies on zeolite catalysts. The strength of this device is its ability to look beyond the ensemble level with sub-particle precision. This exposes inter- and intraparticle activity variations and enables the investigation of industrially relevant catalyst samples. The latter are characterized by their nanometer scale dimensions and complex structural features and compositions. Still, the research reported in my PhD highlighted several challenges and opportunities. Future technical and scientific advances that act on these are therefore anticipated to contribute to a more rationalized improvement of catalyst materials.

On the short term, the development of a liquid flow cell is envisioned based on the experiences accumulated during this work. *In situ* SEM imaging of silver photodeposition from a liquid phase solution was already possible under atmospheric conditions by means of a static liquid cell. However, such an approach is not applicable for the fluorogenic reaction based catalytic activity mapping of zeolite catalysts, as is done in **Chapter 4 and Chapter 5**. The fluorogenic reaction is initiated from the moment the reagent is added to the sample, i.e., without an external trigger such as UV-irradiation in the photocatalytic experiments. Hence, the time needed to assemble and mount the liquid cell would already lead to a fluorescence build-up that precludes nanoscale catalytic activity mapping. In **Appendix 2**, the feasibility of a liquid cell design with flow capabilities is assessed, this would allow the introduction of a reagent to the sample at a certain point after assembly. The successful development of such a device would reduce sampling time and facilitate the correlation of activity maps with structural images. Furthermore, also fluorogenic reaction based structure-activity investigations of photocatalysts would be possible while electron beam interference is avoided.

Structure is not the only determining factor for catalyst performance. Local catalyst composition also plays a crucial role. Especially in zeolite catalysis, where the silicon aluminium ratio dictates the number and strength of acid sites, and a variety of ions are typically exchanged into the structure to improve catalyst performance. Here, the correlation of nanoscale structure-activity information with the local chemical composition obtained from elemental analysis by, e.g., energy dispersive spectroscopy (EDS), would further lead to more profound insights. Such elemental investigations are typically performed using electron doses that lead to extensive sample charging, possibly even compromising sample integrity. This is particularly the case as the sample is typically mounted on an insulating glass cover slide. The application of a liquid flow cell would be helpful, as the presence of liquid surrounding the sample could help to dissipate possible charges.

It is well known that catalyst working mechanisms are strongly influenced by the reaction conditions.[1] For example, zeolite catalysis is typically performed at increased pressures and temperature. This drives the increased efforts towards catalyst research under operando conditions.[2] The possibility of performing nanoscale catalytic activity mapping in the liquid phase already is an addition to this field. Nevertheless, the development of assays that enable catalyst structure-activity investigation at increased temperatures would be a step forward. Performing sample heating in a liquid flow cell should be implementable, as commercial TEM sample holders are already available that allow experiments at elevated temperatures. However, it will be challenging to use an elevated temperature in combination with a high-NA objective lens and the fluorescent properties of the probe reaction will be modified. It is therefore anticipated that such experiments will initially take place on a dedicated SRFM.

Even though SRFM enables nanoscale precise single turnover mapping, the axial resolution remains diffraction limited. Hence, catalytic turnovers occurring within the approximately 500 nm thick optical slice are all projected on the 2D activity map. Particles that are slimmer than this optical slice are therefore instantaneously probed throughout their full volume. As a result, the depth information is lost and obscures nanoscale details by superimposing information of different structural origins. The recent advent of 3D SRFM techniques would thus further increase the resolving power of nanoscale catalytic activity maps.[3,4]

In the introduction of my PhD it is mentioned that correlative SRFM and SEM allows high-throughput experimenting of catalyst activity on the single particle level.[5] Combined with the availability of high-throughput catalyst preparation, this promises to accelerate the search for improved heterogeneous catalysts. A limitation of SRFM for catalysis research is, however, that only catalytic reactions resulting in fluorescent product molecules can directly be visualized. Reactions that do not involve the production of fluorescent product molecules can in some cases be investigated indirectly[6] or, alternatively, correlations can be established that allow extrapolation of SRFM results to more general catalytic reactions.[5] Nevertheless, the development of alternative fluorogenic reactions is indispensable to a wider spread implementation of nanoscale structure-activity investigations. When developing such assays for catalysis research, approaches to investigate the effect of interparticle intergrowths on zeolite catalyst coking and mesopore creation through hydrothermal treatment could also be of interest. The application of diffraction limited confocal fluorescence or Raman microscopy could provide profound insights into different aspects of heterogeneous catalysts which possibly complement those obtained by correlative SRFM and EM. Therefore, there have been increased efforts towards their correlation with EM lately.[7,8]

## 6.1. References

(1) Olaf, D.; Helmut, K.; Karl, K.; Thomas, T. In *Ullmann’s Encyclopedia of Industrial Chemistry*; Bohnet, M., Ed.; John Wiley and Sons, 2014; pp 457–481.

(2) Weckhuysen, B. M. *Chem. Soc. Rev.* **2010**, *39*, 4557–4559.

(3) Huang, B.; Wang, W.; Bates, M.; Zhuang, X. *Science (80-. ).* **2008**, *319* (810), 810–813.

(4) Huang, B.; Sara, J.; Brandenburg, B.; Zhuang, X. *Nat. Methods* **2008**, *5* (12), 1047–1052.

(5) Zhou, X.; Choudhary, E.; Andoy, N. M.; Zou, N.; Chen, P. *ACS Catal.* **2013**, *3*, 1448–1453.

(6) Sambur, J. B.; Chen, P. *J. Phys. Chem. C* **2016**, *120* (37), 20668–20675.

(7) Tian, Y.; Chassaing, D.; Nasibulin, A. G.; Ayala, P.; Jiang, H.; Anisimov, A. S.; Kauppinen, E. I. **2008**, 7188–7189.

(8) de Boer, P.; Hoogenboom, J. P.; Giepmans, B. N. G. *Nat. Methods* **2015**, *12* (6), 503–513.

# Appendices

# Appendix 1

## Automated Image Registration

.

# Appendix 1 – Automated Image Registration

## 7.1. Introduction

Fluorescence imaging approaches, such as photoactivated localization microscopy (PALM)[1] and stochastic optical reconstruction microscopy (STORM)[2], allowed imaging beyond the diffraction limit by leveraging, each in their own way, photo switching behavior of fluorophores to ensure localization of individual fluorescent molecules with extremely high precision. In nanometer accuracy by stochastical chemical reactions (NASCA) imaging, this photoswitching is replaced by the conversion of non-fluorescent reagents into fluorescent products on the catalytically active sites. If the fluorescent product has the correct properties for single molecule detection, this scheme allows a localization of individual catalytic turnovers with nanometer-scale precision.[3] When NASCA is used to study the catalyst structure-activity relationship, structural information is ideally obtained at a resolution that matches the localization accuracy of individual turnover events. This can be achieved by correlating super-resolution fluorescence microscopy (SRFM), for catalytic activity mapping, and scanning electron microscopy (SEM), for structural imaging. As described in **Chapter 1**, such a correlation is commonly achieved by means of two dedicated microscopes.[4,5] This requires specific protocols to retrieve the exact same region of interest (ROI) using both modalities and overlaying them with the highest possible accuracy. In many cases this involves the introduction of luminescent nanoparticles as fiducial markers that can be identified using both SEM and FM. However, this is not always possible, nor desirable, as this potentially compromises sample integrity. Furthermore, even if successful, it remains time consuming to perform proper image registration and the uncontrolled dispersion of these markers does not provide full coverage of the ROI.[6] Hence, it is not universally applicable.

In this PhD project, an integrated light and electron microscope (ILEM) is applied that combines a SRFM and SEM. An initial alignment of the objective lens to the electron gun, preceding the experiments, ensures that the same ROI is probed by both modalities. This already significantly facilitates image registration and by identifying recurring features in the SEM image and catalytic activity map, a coarse image correlation can easily be obtained. This approach has resulted in the overlay images represented in **Chapter 4**. Clearly, this approach allows larger structural features to be correlated with their corresponding catalytic performance, but when investigating nanometer sized structures this method is no longer sufficient. Therefore, we have developed a cathodoluminescence (CL) based procedure that allows a more accurate image registration. This procedure has resulted in the correlated micrographs included in **Chapter 5**. In this appendix, a description of the procedure is provided and different parameters are evaluated to concisely optimize the image registration performance.

## 7.2. Description of the procedure

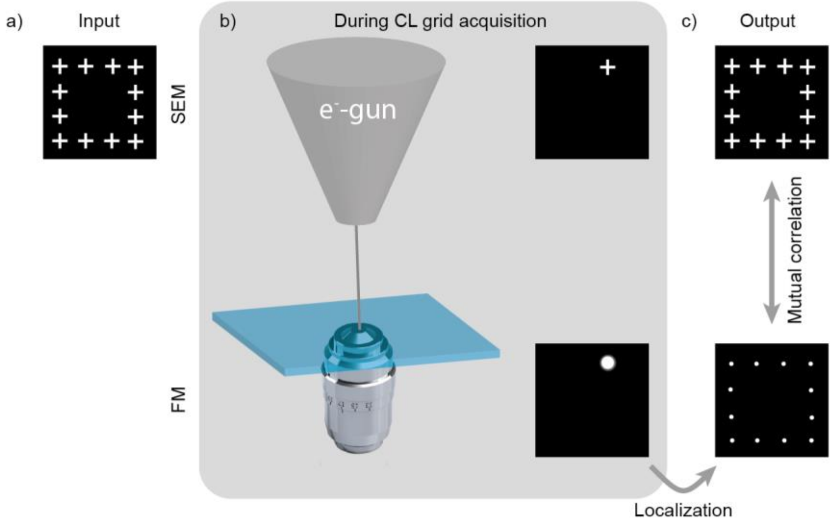

***Figure 7.1.*** *Schematic representation of the CL based procedure used to perform image registration by means of temporal fiducial markers. a) The CL grid positions are provided as SEM input. b) The electron beam is sequentially projected in these grid positions and the resulting diffraction-limited CL signal is detected using the built in optical microscope; care has to be taken to synchronize the camera frame rate to the electron beam movement. c) After projecting the electron beam in all the input positions, the corresponding CL signals that have been detected are localized using the same localization algorithm applied to perform catalytic activity mapping. The obtained localized positions are then correlated with the corresponding input parameters to accurately determine the parameters for correct image registration.*

The image registration procedure outlined here makes use of CL: upon irradiation of a solid material, e.g., a glass cover slide, by a stream of highly energetic electrons, secondary electrons are generated due to inelastic electron scattering.[7] These secondary electrons can, on their turn, also become inelastically scattered, leading to a cascade of scattering events which eventually results in the release of secondary electrons that are in compliance with the energy needed to transfer valence electrons to the conduction band of the solid material. When these electrons subsequently make the opposite movement, a luminescent signal is generated in the UV, visible or NIR range.[8] This luminescence or CL signal is generated at the location where the focused electron beam interacts with the sample and it is detectable using the optical microscope of the ILEM. As the signal only exists during electron irradiation, it can be regarded as a temporal fiducial marker. In practice, the electron beam in spot mode is positioned at 12 locations arranged in a grid like pattern and the corresponding CL signals are detected using the optical microscope. As the luminescence originates from a small point in the sample, typically in the nanometer range, the recorded PSF can be treated and localized like a single luminescent molecule.[8] In this way, the SEM specific coordinates, used as input to project the grid points, can be matched with their coordinates on the EMCCD camera of the ILEM. This enables an accurate determination of the translation, rotation and magnification parameters that are needed for a precise image registration. A schematic representation of this procedure is given in **Figure 7.1**.

For a straightforward implementation of this CL based image registration, a tool has been developed using Matlab and is available at: “https://github.com/KrisJanssen/QuickCLEM”. The input data that is needed to run the application is; 1) a tiff stack with images containing the CL signals of the grid positions, 2) a txt file comprising their respective input coordinates used to direct the electron beam of the SEM, 3) an overview SEM image of the ROI obtained with the same horizontal field width (HFW) as the grid scan, 4) a zoomed image of the ROI and 5) a txt file containing the localized positions of the catalytic turnovers or a tiff file with the diffraction limited fluorescence image. The functionality of the developed Matlab tool is mostly based on already existing and freely available scripts. At the heart of it is the “imwarp” function of Matlab, which transforms the wide field image, or catalytic activity map, based on the parameters obtained by correlating the localized and input data of the CL grid. Additionally, the possibility is offered to manually adjust for large portions of drift in the XY-plane.

## 7.3. Performance of the procedure

There are multiple possible grid configurations that can be used to perform the CL based image registration. However, these different options are expected to influence the performance of the procedure. First off, the number of grid positions should not be too large, as this would render the procedure time consuming and sample charging would make a proper image registration challenging, since it could shift the CL location of nearby grid positions by repelling the incoming electron beam. Extensive charging could even compromise sample integrity. Therefore, the configuration of choice consisted of a square grid at the rim of the FOV, surrounding the sample, instead of a full raster covering the full FOV. This further reduces charging, and the related shift in CL spot localization and sample damaging. The optimal grid configuration was considered to entail 12 CL projections at the rim of the FOV. A concise practical investigation of this configuration is performed to validate this theoretical assessment.

The image registration performance achieved by means of the described grid configuration was assessed using a regularly spaced gold nanoparticle (NP) sample on a glass cover slide (20 x 20 NP’s of 120 nm with 1 µm spacing) obtained from the group of Kosei Ueno in Japan. The Au NP’s can be readily visualized in SEM and via their plasmon emission, also a strong optical signal is detected, e.g., using the 532 nm illumination and 545-620 nm detection.

This signal can be used to localize their position in the optical microscope. An accurate determination of the Au NP positions in the SEM image is achieved by applying a SOBEL-Feldman operator to identify the edges of the NP’s, after which their center of mass is calculated. The image registration performance was subsequently analyzed by determining the mutual distance between the center of the Au NP in the SEM image and the corresponding localized position of the plasmon emission. The latter is assumed to align to the center of the sub diffraction sized NP’s.[9] The result of such an analysis is shown in **Figure 7.2**. The red asterix corresponds to the localized plasmon location and the blue circle to the center of mass of the Au NP. Both are superimposed on the SEM image after applying the overlay procedure. The calculated mutual distances for corresponding positions are provided in the distribution plot. By fitting a Gaussian function to this plot and determining the mean and standard deviation, the performance of different grid configurations can be compared. This comparison is considered to be qualitative, as no proper statistical approach has been used.

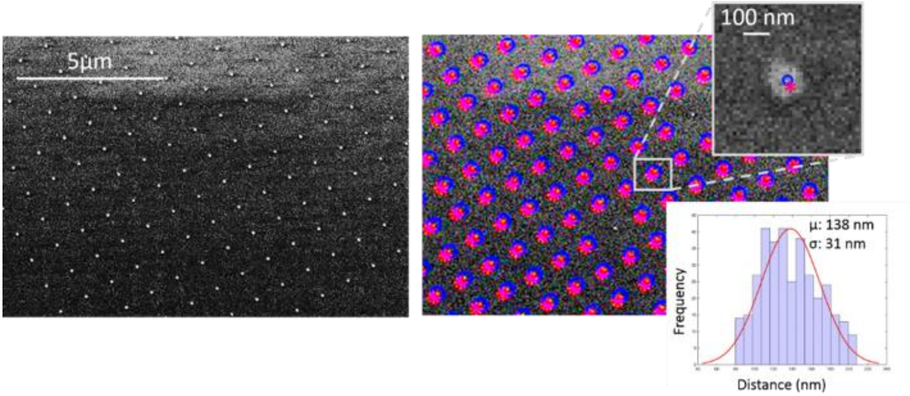

***Figure 7.2.*** *Left: Gold nanoparticle grid; Right: the centroid positions (blue circles, SEM) and localized positions (red asterix, SRFM) superimposed onto the SEM image by means of the autocorrelation procedure. The top inset is an enlarged FOV of one such gold nanoparticle, showing, in detail, the discrepancy between the localized position based on the photoluminescence data and centroid position determined from the SEM image. The bottom inset shows the distribution function of the mutual distance between every localized and centroid position in the sample, by fitting this to a Gaussian function and determining the standard deviation and average, a measure for the performance of a certain procedure can be obtained.*

Besides different grid configurations, also the use of different acquisition parameters and the order in which the input data is obtained will influence the performance of image registration. For instance, the localization precision depends on the EMCCD settings used during the CL acquisition, as the signal-to-noise ratio will change. The same holds for the electron beam properties. By increasing the acceleration voltage and beam current (Spot Size), the signal-to-noise ratio of the detected CL positions will be increased and, hence, image registration will be more accurate. However, the latter will also lead to increased sample charging. As was previously described, this is disadvantageous. Additionally, regardless of the SEM imaging conditions that are used, charging will always be introduced to some extent. The order in which the SEM image and CL grid are acquired is therefore also expected to affect the performance of image registration. The results of this evaluation are represented in **Figure 7.3**. **Figure 7.3a** shows the influence of different EMCCD settings and SEM conditions for CL grid localization by means of the localization error. The effect of the different acquisition orders and number of grid positions is displayed in **Figure 7.3b** as a means of the standard deviation determined for the mutual distances between localized and centroid positions.

Clearly, when using an increased acceleration voltage and beam current to induce the CL, the localization error decreases as the CL intensity gets higher. The same holds for increased electron gain and exposure time for the CL detection on the EMCCD. However, as increased electron currents induce charging, it is not optimal to use the settings that have been determined to be most performant, i.e., combination 1.3 in **Figure 7.3a**. Combination 1.1 thus represents the optimal CL grid detection and deposition parameters for application in this PhD.

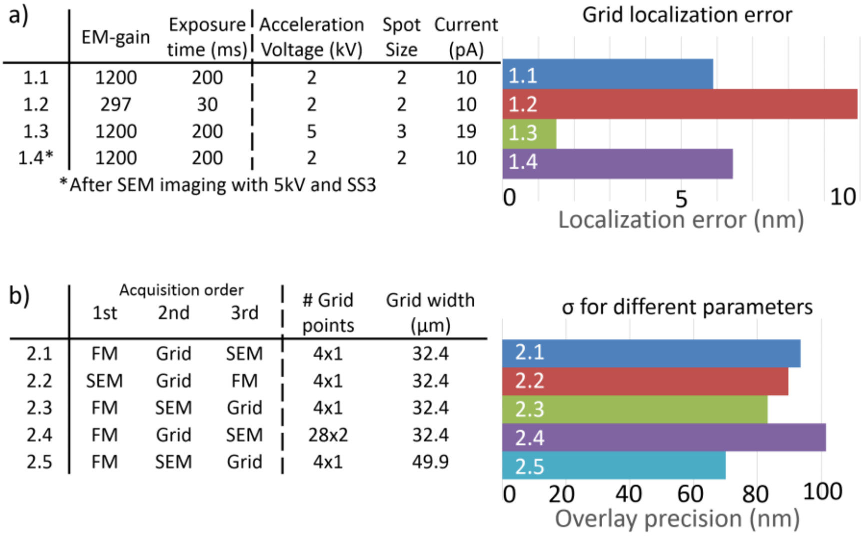

a)

|  | EM-gain | Exposure time (ms) | Acceleration Voltage (kV) | Spot Size | Current (pA) |
|---|---|---|---|---|---|
| 1.1 | 1200 | 200 | 2 | 2 | 10 |
| 1.2 | 297 | 30 | 2 | 2 | 10 |
| 1.3 | 1200 | 200 | 5 | 3 | 19 |
| 1.4* | 1200 | 200 | 2 | 2 | 10 |

*After SEM imaging with 5kV and SS3

b)

|  | Acquisition order |  |  | # Grid points | Grid width (µm) |
|---|---|---|---|---|---|
|  | 1st | 2nd | 3rd |  |  |
| 2.1 | FM | Grid | SEM | 4x1 | 32.4 |
| 2.2 | SEM | Grid | FM | 4x1 | 32.4 |
| 2.3 | FM | SEM | Grid | 4x1 | 32.4 |
| 2.4 | FM | Grid | SEM | 28x2 | 32.4 |
| 2.5 | FM | SEM | Grid | 4x1 | 49.9 |

***Figure 7.3.*** *Comparison of different protocols to obtain the input data required to perform the CL based image registration. a) Different CL grid deposition and detection parameters are assessed and b) different acquisition orders and grid parameters have been compared to determine the most optimal procedure. Note: # of grid points corresponds to the number of grid positions in the X and Y direction, times the thickness of the grid. 4x1 (represented in **Figure 7.1**) thus corresponds to 12 grid positions. 28x2 corresponds to 208 grid positions.*

Secondly, the influence of the acquisition order of the different input data is considered in **Figure 7.3b**. Based on the standard deviation of the mutual distance distribution, the most optimal acquisition order is the one in which the grid scan is performed after SEM imaging, with a grid width exceeding the FOV of the EMCCD camera (Combination 2.5). The latter will effectively lead to CL projections close to the edge of the EMCCD FOV.

It is important to note that the protocols that have been considered above, all apply to CL based image registration performed during *in situ* experiments. Hence, SEM and (SR)FM are performed within the vacuum of the SEM chamber. However, the ILEM is applied correlatively in **Chapter 5**. This requires the SEM chamber to be vented to atmospheric pressure after structural imaging and prior to SRFM. Even though the applicability of the developed image registration procedure is not altered, since the required data can still be obtained prior to venting, this will have consequences on the image registration performance. Moreover, the most performant acquisition order and settings, as determined in the current assessment, are still valid, but, venting will induce sample drift which needs to be corrected for. This correction can be done manually in the provided Matlab script, but makes the image registration less accurate. A solution to this drawback would be to calibrate the induced drift using a standard sample, such as the gold NP's on a glass cover slide, or by performing truly integrated experiments using a liquid flow cell.

## 7.4. Conclusion

A CL based image registration procedure was developed that enables an automated correlation of (SR)FM and SEM images by introducing temporal fiducial markers, and has been made freely available as a Matlab tool. The performance of this procedure has been assessed for different input parameters and protocols. A regularly spaced gold NP grid deposited on a glass cover slide served as the reference sample. By determining the mutual distance between the corresponding centroid and localized positions of gold NP's on the SEM and SRFM images, after performing image registration, the prime acquisition order and settings were established. This assessment clearly revealed the effect of charging. Importantly, the optimal application of this tool would be for *in situ* experiments.

## 7.5. References

(1) Betzig, E.; Patterson, G. H.; Sougrat, R.; Lindwasser, O. W. W.; Olenych, S.; Bonifacino, J. S.; Davidson, M. W.; Lippincott-Schwartz, J.; Hess, H. F. *Science (80-. ).* **2006**, *313* (5793), 1642–1645.
(2) Rust, M. J.; Bates, M.; Zhuang, X. *Nat. Methods* **2006**, *3* (10), 793–796.
(3) Roeffaers, M. B. J.; De Cremer, G.; Libeert, J.; Ameloot, R.; Dedecker, P.; Bons, A. J.; Bückins, M.; Martens, J. A.; Sels, B. F.; De Vos, D. E.; Hofkens, J. *Angew. Chemie - Int. Ed.* **2009**, *48* (49), 9285–9289.
(4) Robinson, J. M.; Vandre, D. D. *J. Histochem. Cytochem.* **1997**, *45* (5), 631–

642.
(5) Zhou, X.; Andoy, N. M.; Liu, G.; Choudhary, E.; Han, K.-S.; Shen, H.; Chen, P. *Nat. Nanotechnol.* **2012**, *7* (4), 237–241.
(6) de Boer, P.; Hoogenboom, J. P.; Giepmans, B. N. G. *Nat. Methods* **2015**, *12* (6), 503–513.
(7) Mitsui, T.; Sekiguchi, T.; Fujita, D.; Koguchi, N. *Jpn. J. Appl. Phys.* **2005**, *44*, 1820–1824.
(8) Boggs, S.; Krinsley, D. *Application of Cathodoluminescence Imaging to the Study of Sedimentary Rocks*; Cambridge University Press, 2006.
(9) Bon, P.; Bourg, N.; Lécart, S.; Monneret, S.; Fort, E.; Wenger, J.; Léveque-Fort, S. *Nat. Commun.* **2015**, *6*.

# Appendix 2

## *In situ* Correlative Imaging

.

# Appendix 2 – *In situ* correlative imaging

## 8.1. Introduction

In this PhD thesis, an integrated light and electron microscope (ILEM) was applied to investigate the structure-activity relationship in heterogeneous catalysts. This required the use of a liquid phase reagent, which is incompatible with the vacuum conditions required inside the SEM chamber during operation. Therefore, it was already attempted from the start of this PhD to make use of a liquid cell that contains a limited volume of reagent solution squeezed between an electron transparent $Si_3N_4$ window, and an optically transparent cover slide. As such, both scanning electron microscopy (SEM) and super-resolution fluorescence microscopy (SRFM) could be performed simultaneously. This has enabled *in situ* UV induced silver photodeposition on ZnO photocatalysts while performing SEM imaging (**Chapter 2**; see **Figure 2.4**).

Regardless of this successful application, several shortcomings of the liquid cell design were exposed. For instance, the distance between the sample on the $Si_3N_4$ window and the cover slide, which was specified to 50 µm, was not reproducible and often much larger due to improper and inaccurate sample mounting. This rendered it difficult to focus the high NA objective lens (Nikon 1.4 NACFI Plan Apo VC 100X Oil), which has a working distance of 130 µm, onto the sample. This was an intrinsic flaw of the liquid cell, as it was not precisely manufactured and liquid cell assembly could not repetitively be achieved. **Figure 8.1** schematically represents this initial liquid cell design. Further, since the assembly of the liquid cell could not be delicately achieved, the electron transparent window regularly ruptured during this critical step. Additionally, the reagent solution must already be loaded into the cell prior to its assembly. Particularly when using a fluorogenic reaction to investigate solid acid catalysts, the time that is needed to reach the required vacuum conditions for SEM imaging leads to a fluorescence buildup that renders single turnover mapping impossible. The ILEM has therefore further been applied in a correlative fashion in **Chapters 3-5**, i.e., after SEM imaging the system is vented and the reagent solution is added while doing the SRFM experiments. Nonetheless, the development of a robust liquid cell with flow capabilities would be highly beneficial, as this would reduce sampling time and increase the performance of image registration (**Appendix 1**). For the design and manufacturing of such a device, Comate, an engineering bureau from Leuven, was contacted for advice and support. In this appendix, a state of the art of similar devices is provided, our requirements are stated and a design is proposed.

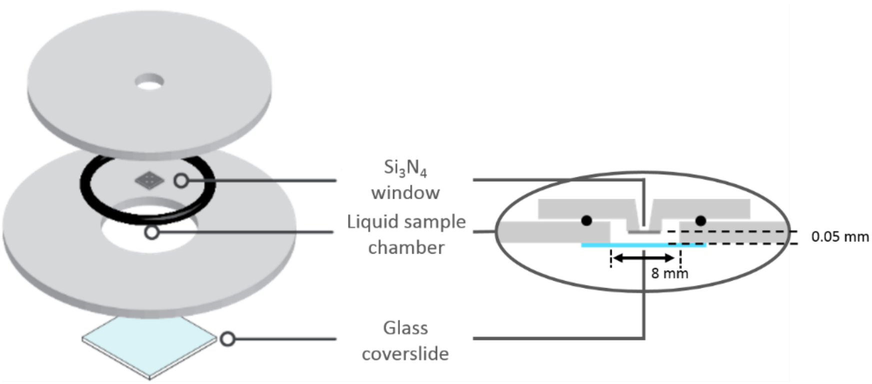

***Figure 8.1.** Schematic representation of the liquid cell used for the in situ investigation of photocatalytic silver deposition in **Chapter 2**.*

## 8.2. State of the art

The start of this technical design consisted of a close comparison of the few liquid and flow cell designs that have been developed for application in environmental and *in situ* TEM and SEM. Some of these designs, such as the “SPI Wet cell 2” or “DENS solutions Ocean cell”, are even commercially available. However, even though these commercially available devices are very robust and often have similar features as would be required from a liquid cell for application in an ILEM, none of them allows simultaneous SEM and SRFM studies. The most relevant features of these systems were extracted in the following report on the state of the art. This will be the starting point for the proposed liquid cell design with flow capabilities that suits our needs.

### SPI Wet cell 2[1]

SPI offers an integrated system that enables analysis of samples submerged in liquids through a $Si_3N_4$ window for application in vacuum-based chemical analysis instruments (**Figure 8.1**). The design consists of a PDMS block at the bottom of the sample holder, which is fitted with channels that allow liquid transport to and from the actual reactor cell, located under a thin $Si_3N_4$ membrane. By etching the latter membrane, an aperture is created through which the fluid submerged sample can be observed. By carefully determining the size of this aperture, it is made sure that there is no significant evaporation. The device additionally comprises a liquid reservoir containing the fluid used in the experiment, a liquid flow path, a pressure relief capillary and an electro-osmotic pump that ensures circular flow of the fluid through the flow path once it is connected to a battery (**Figure 8.2b**, component c). This configuration enables proper operation without the need for electrical or fluid connections to pass through the walls of the SEM chamber. This leads to the universal applicability of the device in any SEM. Importantly, all these components are contained under a metal cover and only the PDMS block is in direct contact with the vacuum. It is therefore extremely leakage proof. A similar device would be ideal for application in our ILEM, if the PDMS block could be replaced by a reactor cell that holds an optically transparent cover slide at the bottom.

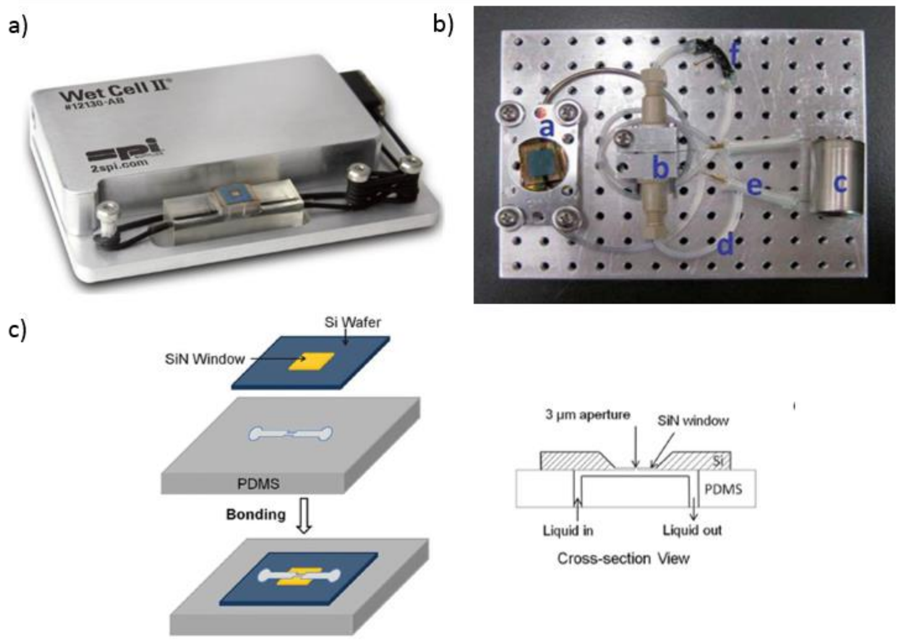

***Figure.8.2.*** *a) Integrated liquid flow cell design available from spi.*[2] *b) the components embedded under the protective cover; a. liquid cell carved from a PDMS block, equipped with a* $Si_3N_4$ *window b. electro-osmotic pump c. battery d. microfluidic tubing e. electric wiring between the battery and pump f. pressure relief capillary. Reproduced from Ref.* [3] *with permission from The Royal Society of Chemistry. c) Schematic representation of the PDMS block, holding the* $Si_3N_4$ *window and fitted with the channels that allow liquid flow in and out of the liquid cell. Reproduced with permission from Ref.* [4]

### Hummingbird scientific liquid TEM sample holder[4]

Different liquid cell devices for transmission electron microscopy (TEM) are available from Hummingbird scientific and all are based on the same design (**Figure 8.3a**). Two $Si_3N_4$ membranes with electron transparent windows are placed 500 nm apart, by using a spacer which is integrated onto one of both. This spacer, made from SU8 photoresist, which has excellent solvent compatibility, is used to ensure that both membranes are at a reproducible distance and its thickness can easily be decreased, possibly bringing both windows within 50 nm distance. Precision milled slots, in combination with proper O-rings and screws allow a precise assembly of the liquid cell, which is then mounted into a pen type cell holder (**Figure 8.3b**). These should, hence, also be modified with respect to the applied spacer thickness. A pen type assembly, as described here, can conveniently and reproducibly be mounted into a dedicated port in the TEM chamber wall. As such, this pen acts as the barrier between the in- and outside of the TEM vacuum chamber and the required fluid and electric connections can easily be provided to the liquid cell. Liquid flow is established by means of an external syringe pump. The combination of the pen cell holder with a variety of membranes allows different applications, such as electrochemical reactions or EDS analysis. Also sample heating is possible using the liquid flow cell, and temperatures of up to 1000 °C can be achieved under accurate temperature control by means of a thermocouple. Additionally, a specialized holder can be used to enable "cross-correlative" experiments. This means that the liquid cell tip that is typically mounted into the pen assembly, can also be mounted into a dedicated holder attached to the stage of an optical microscope (**Figure 8.3c**). This configuration allows both TEM and fluorescence microscopy, using two dedicated setups. As the thin $Si_3N_4$ window is fragile, air objectives rather than oil immersion objectives with high NA are used in a consecutive fashion. A similar solution is available for dedicated *in situ* SEM measurements and comprises a liquid cell and a dedicated mount (**Figure 8.3d**). Again, the limiting factor is the absence of an optically transparent cover slide as SRFM ideally requires a high NA oil immersion objective lens for proper correlative SRFM and SEM.

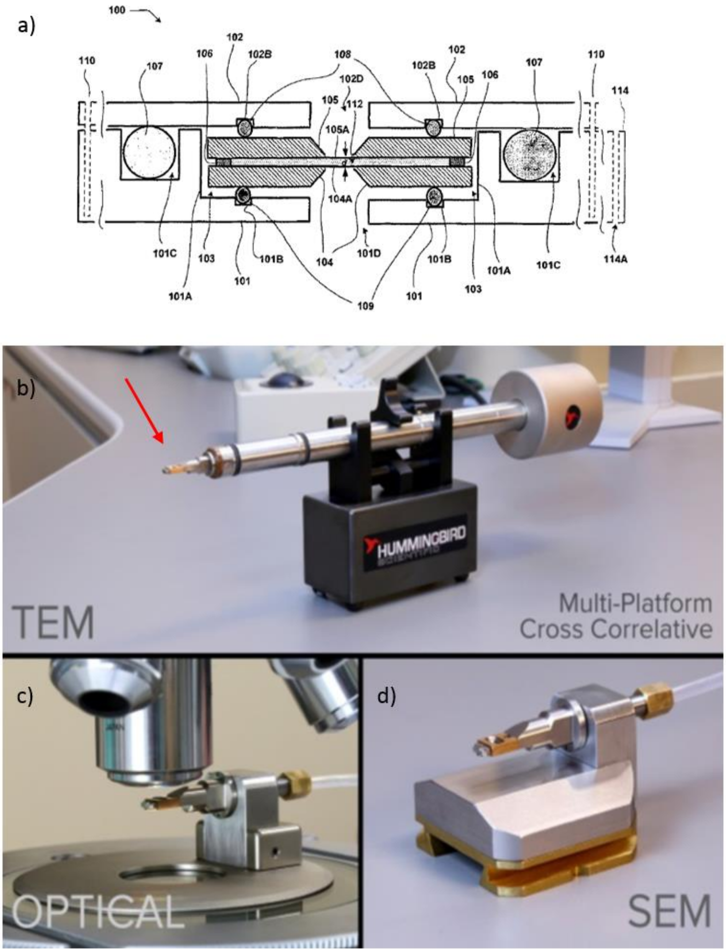

***Figure 8.3.*** *a) Liquid cell design for in situ TEM imaging.*[5] *The most relevant components are: 100: The sample holder, 104: Silicon wafer, 104A:* $Si_3N_4$ *window, 105: Silicon wafer, 105A:* $Si_3N_4$ *window, 106: A spacer for maintaining a pre specified gap "d", 107: First O-ring, 108: Second O-ring, 109: Third O-ring, and 112: The sample. b) Pen type assembly that holds the liquid cell in its tip (indicated by the red arrow) and can be reproducibly introduced into the SEM chamber. c) Liquid cell holder enabling "cross-correlative" optical microscopy. d) Liquid cell holder that enables SEM investigations.*[6]

## Other *in situ* sample holders

Both DENS solutions and Protochips fabricate *in situ* TEM and SEM sample holders with liquid flow capabilities similar to those available from Hummingbird scientific. A pen assembly in which different liquid cells, composed of specific $Si_3N_4$ chips, can be mounted, is introduced into the vacuum chamber of a TEM through a specific port. By equipping one of the opposing $Si_3N_4$ windows with spacers, a proper liquid cell thickness can be ensured of up to 50 nm and channels can be provided. As such, a syringe pump driven flow is enabled through the reactor cell. The uniqueness of the liquid flow cell available from Protochips is in the use of dedicated gaskets that improve flow from the pen assembly through the liquid cell and over the electron transparent windows.[7] Several possible chips and sample holders are available that allow electrochemical investigations, the introduction of gasses into the reactor cell, heating of the sample, etc. The latter is attained by the "DENS solutions WildFire" and "Protochips Poseidon Select" *in situ* cells. Particularly, the WildFire cell from DENS solutions can reach temperatures of up to 1300°C with a stability of 0.001°C.

## 8.3. Requirements for an ILEM liquid flow cell

In the following section, a summary of the requirements that the liquid flow cell should meet is presented.

### Windows and sealing

In order to allow *in situ* SEM and SRFM experiments, a liquid cell needs to be designed that consists of both an electron and optically transparent window. The electron transparent window should be part of the top element of the liquid cell and the sample will be attached to the bottom of this window. The optically transparent glass cover slide should be part of the bottom of the liquid cell and should have the standard dimensions (e.g. 22 x 22 $mm^2$) and #1 thickness. Physical contact with the high NA objective lens through an immersion liquid should also be possible. It is important that the liquid cell is properly sealed because of the 1 bar pressure difference between the inside of the sample holder and the $1x10^{-9}$ atm vacuum conditions inside the SEM chamber. Importantly, if the volume of liquid in the cell is too high upon assembly, the thin electron transparent window (about 30 nm thick) will bulge out upon closing. This could lead to rupturing of the window due to pressure build-up during assembly or by introducing it to the vacuum of the SEM chamber. Such significant pressure differences over the window should be prevented by high precision manufacturing.

### Liquid reservoirs and flow

A liquid reservoir is needed that contains the desired solution prior to introduction into the liquid cell. As accidental cell leakage should be considered, the amount of liquid should be minimized. Additionally, a reservoir or buffer area should be foreseen to prevent unnecessary pressure build up while flowing the solution into the liquid cell. Overpressure could easily lead to rupturing of the thin $Si_3N_4$ window. To fill the reactor cell, the solution needs to be transferred from the reservoir. This can either be achieved by active pumping of the liquid, or by a height induced pressure difference between the liquid reservoir and the recipient. In the latter case, fluid flow is controlled by opening a valve. This should only be done after the sample holder is assembled and held in the vacuum of the SEM chamber and thus an external trigger is needed. An electronic connection to the liquid cell can be established through the side flange of the SEM by means of COAX connectors. This prevents leakage of the vacuum chamber. Additionally, all tubing and liquid containing components are fully contained within the vacuum chamber. As such, no fluids connections are needed between the in- and outside of the SEM. Also a practical procedure or interface should be designed that allows a straightforward introduction of the liquid into the holding reservoir prior to assembly of the device.

### Sample submersion and liquid cell thickness

Care has to be taken that after opening the valve or initiating the pump, the sample is properly submerged in the liquid. Due to the configuration of the ILEM, the sample will be attached to the bottom of the electron transparent window, which is at the top side of the liquid cell. This potentially hampers full wetting of the sample. Therefore, an important parameter that needs to be considered is the wettability of the electron transparent window, as a different polarity between the solution and window could lead to an incomplete submersion of the sample. A brief oxygen plasma treatment of the $Si_3N_4$ window could be used to render it hydrophilic. This ensures proper wettability when using polar solvents. In case apolar solvents are used, no treatment is required. Additionally, a determinant factor when considering liquid cell filling, is the height of the liquid volume (distance between top of cover slide and bottom of $Si_3N_4$ window). As the working distance of the objective lens is 130 µm, this puts a hard limit to the potential height. Actually, to improve imaging conditions, smaller distances are preferred. From experience, distances of below 50 µm are considered optimal. However, there is also a lower limit; as the samples will be introduced onto the $Si_3N_4$ window, the distance to the glass should exceed the crystal size. For this work, 20 µm was set as the lower limit. This height can be attained by using correct spacers (O-rings) in the hardware design and using $Si_3N_4$ membranes equipped with etched spacers (SU8).

### Leakage security

As all fluid containing components should be fully integrated into the vacuum chamber, a cover that fully conceals the device, except the liquid cell itself, further minimizes the risk of chamber contamination in case of leakages of the tubing and connections. Electric wiring can easily be introduced without compromising the leak security as previously discussed.

## 8.4. Proposed design

Based on these insights and considerations, a possible design was proposed as a starting point. This design is composed of elements from the covered-up flow system from SPI and the liquid cell design used in the TEM applications.

More precisely, the liquid cell should be composed of one electron transparent $Si_3N_4$ window with spacers, mounted on the top, and a glass cover slide at the bottom. Proper spacing and sealing is further ensured by providing the necessary spacers in the form of O-rings. By equipping in- and outlets that are connected with microfluidics, fluid will be able to flow through the reactor cell. The fluid containing the reagent solution is initially stored in a reservoir or excess tubing and introduced into the liquid cell by a miniature electro-osmotic pump, or valve. An additional reservoir, or excess tubing, should be present to serve as pressure relief and accept spent fluid. Also a metal cover with proper sealing is part of the proposed design as an additional leakage security. A schematic drawing is provided in **Figure 8.4**. Electronic connections that enable operating the pump or valve, are not part of **Figure 8.4.**, but can be established by means of COAX connectors through the SEM chamber wall.

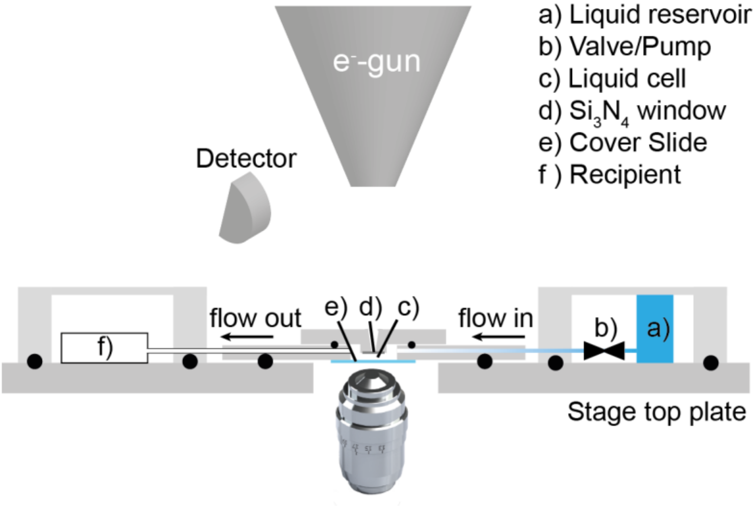

***Figure 8.4.*** *Proposed liquid flow cell design that is integrated with the stage top plate and contains a cover for the different components, except the liquid cell itself, to prevent liquid leakage. The black discs are indicative for O-rings in the front view. Al other components are assigned in the schematic image.*

## 8.5. Conclusion

The research described in this PhD illustrates that a device that enables *in situ* experiments on the ILEM would be highly beneficial, but its development is not straightforward. Several liquid flow cell devices are commercially available to perform *in situ* SEM or TEM imaging, but none of them complies with the demands for correlative *in situ* SEM and SRFM. Therefore, a report is made on the state of the art devices, exploring relevant features that would enable the development of an *in situ* cell for the ILEM. A device integrated into the top plate of the SEM sample stage, where all components are covered from the vacuum and only electrical connections are needed between the in- and outside of the vacuum chamber is regarded as being the optimal configuration. The liquid sample holder itself should consist of a glass cover slide at the bottom and a $Si_3N_4$ window at the top, accurately separated by a photo resistive spacer deposited onto the latter. These findings have been transferred to a design company that will further develop the details and ultimately provide us with a well-functioning liquid flow cell.

## 8.6. References

(1) Yang, L.; Yu, X.-Y.; Zhu, Z.; Iedema, M. J.; Cowin, J. P. Systems and Methods for Analyzing Liquids Under Vacuum. 8555710 B2, 2011.

(2) Structure Probe Inc. Wet Cell II Liquid Probe System for SEM/EDS,EPMA and TOF-SIMS https://www.2spi.com/item/12130-ab/ (accessed Jun 26, 2017).

(3) Yang, L.; Yu, X.-Y.; Zhu, Z.; Iedema, M. J.; Cowin, J. P. *Lab Chip* **2011**, *11* (15), 2481–2484.

(4) Yang, L.; Yu, X.-Y.; Zhu, Z.; Thevuthasan, T.; Cowin, J. P. Making ahybrid microfluidic platform compatible for in situ imaging by vacuum-based techniques. *J. Vac. Sci. Technol. A* **2011**, *29*, 061101-10

(5) Charles P., M.; Olson, E.; Todor I., D.; Ivan, P.; Jianguo, W.; Ryan, F.; Dongxiang, L. Reusable Sample Holding Device Permitting Ready Loading of Very Small Wet Samples. 8059271 B2, 2011.

(6) Scientific, H. Cross-Correlative http://hummingbirdscientific.com/products/liquid/ (accessed Jun 26, 2017).

(7) Daniel Stephen, G.; Franklin Stampley, W.; John, D. Method for Optimizing Fluid Flow Across a Sample Within an Electron Microscope Sample Holder. 9466459 B2, 2016.

# Curriculum Vitae

## Personalia

| | |
|---|---|
| Name: | Jordi Van Loon |
| E-Mail: | jordivanloon20@gmail.com |
| Linkedin: | www.linkedin.com/jordivl |
| Place of birth: | Antwerp (Ekeren), Belgium |
| Date of birth: | 23/11/1989 |

## Education

| | |
|---|---|
| 2013 – 2017 | KU Leuven, PhD, Bioscience Engineering |
| 2011 – 2013 | KU Leuven, MSc, Chemistry |
| 2007 – 2011 | KU Leuven, BSc, Chemistry |

## Contributions to education

[1] 2015 and 2016 – Teaching of an exercise session for the course “Chemie vaste stof water interfase”; topic: ion exchange capacity and determination of solubility.

[2] 2nd term 2016 – Supervision of ProjectWerk Interfasechemie; students: Felix Janssens, Stephanie Kennis and Hatice Kurban.

[3] 2nd term 2015 – Supervision of ProjectWerk Interfasechemie; students: Thomas Cuypers, Raymond Thür and Jonathan Vandendriessche.

[4] 2013-2014 – Supervision of a master thesis project; student Xian Gu

## List of publications

[1] Kubarev A., Breynaert E., Van Loon J., Layek A., Fleury G., Radhakrishnan S., Martens J., Roeffaers M. **2017**. Solvent polarity-induced pore selectivity in H-ZSM-5 catalysis. *ACS Catalysis*, 7, 4248-4252.

[2] Van Loon J., Janssen K., Franklin T., Kubarev A., Steele J., Debroye E., Breynaert E., Martens J., Roeffaers M. **2017**. Rationalizing acid zeolite performance at the nanoscale by correlative fluorescence and electron microscopy. *ACS Catalysis*, 7, 5234-5242.

[3] Kennes K., Demaret C., Van Loon J., Kubarev A., Fleury G., Sliwa M., Delpoux O., Maury S., Harbuzaru B., Roeffaers M. **2017**. Assessing inter and intra-particle heterogeneity in alumina-poor H-ZSM-5 zeolites. *ChemCatChem*.

[4] Yuan H., Debroye E., Caliandro G., Janssen K., Van Loon J., Kirschhock C., Martens J., Hofkens J., Roeffaers M. **2016**. Photoluminescence Blinking of Single-Crystal Methylammonium Lead Iodide Perovskite Nanorods Induced by Surface Traps. *ACS Omega*, 1, 148-159.

[5] Debroye E.*, Van Loon J.*, Yuan H., Janssen K., Lou Z., Kim S., Majima T., Roeffaers M. **2016**. Facet-Dependent Photoreduction on Single ZnO Crystals. *Journal of Physical Chemistry Letters*, 8, 340-346.

[6] Debroye E.*, Van Loon J.*, Gu X., Franklin T., Hofkens J., Janssen K., Roeffaers M. **2016**. Assessing Photocatalytic Activity at the Nanoscale Using Integrated Optical and Electron Microscopy. *Particle & Particle Systems Characterization*, 33, 412-418.

[7] Janssen K., De Cremer G., Neely R., Kubarev A., Van Loon J., Martens J., De Vos D., Roeffaers M., Hofkens J. **2014**. Single molecule methods for the study of catalysis: from enzymes to heterogeneous catalysts. *Chemical Society Reviews*, 43, 990-1006.

[8] Liu K.*, Kubarev A.*, Van Loon J., Uji-I H., De Vos D., Hofkens J., Roeffaers M. **2014**. Rationalizing Inter- and Intracrystal Heterogeneities in Dealuminated Acid Mordenite Zeolites by Stimulated Raman Scattering Microscopy Correlated with Super-resolution Fluorescence Microscopy. *ACS Nano*, 8, 12650-12659.

* Equal contribution

## Conference participation

[1] Poster presentation: “Combined super-resolution fluorescence and electron microscopy for catalysis research” presented during the Methods and Applications in Fluorescence conference, held in *Bruges, Belgium*. **12/09/2017**

[2] Oral presentation: “Revealing the zeolite structure-activity relationship using super-resolution fluorescence and scanning electron microscopy” presented during the chemical research in Flanders symposium, held in *Blankenberge, Belgium*. **26/10/2016**

[3] Poster presentation: “Relating structural heterogeneities to catalyst activity and post-synthetic modification by integrating fluorescence and electron microscopy” presented during the 18th international zeolite conference, held in *Rio de Janeiro, Brasil*. **21/06/2016**

[4] Poster presentation: “Correlating scanning electron microscopy with super-resolution fluorescence microscopy” presented during the focus on microscopy conference, held in *Taipei, Taiwan*. **22/03/2016**

[5] Poster presentation: “Super-resolution fluorescence and scanning electron microscopy for correlative catalysis research” presented during the 17th international symposium on relations between homogeneous and heterogeneous catalysis, held in *Utrecht, The Netherlands*. **13/07/2015**

[6] Poster presentation: “Combined super-resolution fluorescence and electron microscopy for catalysis research” presented during the Operando V conference, held in *Deauville, France*. **21/05/2015**

[7] Poster presentation: “Combined super-resolution fluorescence and electron microscopy for catalysis research” presented during the Dutch Zeolite Association 2014 meeting, held in *Gent, Belgium*. **07/10/2014**

[8] Poster presentation: “Combined super-resolution fluorescence and electron microscopy for catalysis research” presented during the progress and trends in chemistry, catalysis and chemical engineering symposium, organized on the occasion of the honorary PhD rewarding ceremony for Prof. Gerald G. Fuller, held in *Leuven, Belgium*. **03/06/2014**

## Oral presentations

[1] Seminar entitled “Revealing the zeolite structure-activity relationship using super-resolution fluorescence and scanning electron microscopy” presented at the Chemical Research in Flanders Symposium. **26/10/2016**

[2] Seminar entitled “Revealing the structure activity relationship at the nanoscale in mordenite crystals through correlated super-resolution fluorescence and scanning electron microscopy” presented during a Unit 1 group meeting at the COK. **11/03/2016**

[3] Seminar entitled “Super-resolution fluorescence and scanning electron microscopy for correlative catalysis research” presented during a group meeting of the Molecular Imaging and Photonics group. **09/11/2015**